Mechanical Behaviour of Silver Nanowires

A thesis submitted to the University of Manchester for the degree of

Doctor of Philosophy

in the Faculty of Science and Engineering

2021

Hu Zhao

School of Natural Sciences Department of Materia

Contents

Word Count: 52,597

Abstract

Hu Zhao 2021

Doctor of Philosophy ---The University of Manchester

Mechanical Behaviour of Silver Nanowires

The properties of Ag nanowires (NWs) are ideally suited for applications as flexible transparent electrodes. To predict and improve the reliability of flexible electronic devices made using Ag NWs, it is necessary to study their mechanical behaviour. Ag NWs fabricated by the commercial polyol process show a pentatwinned structure. This thesis uses transmission electron microscopy (TEM) to characterize individual Ag NWs after the deformation in tension, bending and cyclic fatigue loading. Where appropriate, the behaviour of the pentatwinned Ag NWs is compared with equivalent single crystal Ag NWs.

The tensile mechanical properties of pentatwinned Ag NWs are directly compared with single crystal NWs prepared by template electrodeposition over a range of diameters, d, 80 – 300 nm. The plastic flow strengths of both sets of NWs show a significant size effect, which is shown to follow the same empirical scaling law seen with other fcc structured metals. TEM investigation of the deformation structures in each case shows little significant difference between the two classes of NW studied, with relatively low dislocation densities present after deformation. The deformed pentatwinned NWs showed no evidence for any characteristic deformation structures associated with the twin boundaries running parallel to the NW axis.

The deformation structures in both pentatwinned and single crystal NWs are investigated after plastic bending deformation using TEM and electron diffraction. Structural analysis is carried out using high spatial resolution scanning precession electron diffractions (PED). Machine learning methods were used to analyse the overlapping diffraction patterns obtained from the pentatwinned NWs and determine the orientations of the silver subcrystals around localized bends in the wires. While the single crystal NWs showed bending deformation accommodated by a high angle boundary plane, the pentatwinned wires were found to display simple in-plane bends with narrow deformation zones in all 5 sub-crystals of the wire, with a common boundary plane. A coincident site lattice model has been developed to explain the bending angles seen in individual NWs and the observed distribution of angles in a population of pentatwinned NWs. The geometrical constraints of the model explain the difference in this distribution when compared to that from a population of single crystal NWs.

The final part of the project investigated the mechanical behaviour of Ag NW in networks under cyclic (fatigue) loading. The extent of fibre fracture was determined through quantitative determination of the NW end point density changes enabling an analysis of current models predicting the resistance of NW networks. The microstructure of pentatwinned Ag NWs changes after fatigue tests. Bamboo-like faults were observed and characterized using PED in a similar way to the bending analysis described above. It was found that crystal rotations associated with a semi-coherent twist boundary occurred in the bamboo faults. The torsion forces leading to crystal rotation suggests that the far-field tensile stresses in the film can manifest as a variety of local stresses locally in the network particularly when the NWs are constrained by junctions. The reversible behaviour of bamboo faults from the network was observed at high cycle numbers and is supported by a high-energy state argument.

Declaration

No portion of the work referred to in the thesis has been submitted in support of an application for another degree or qualification of this or any university or other institute of learning.

Copyright statement

i. The author of this thesis (including any appendices and/or schedules to this thesis) owns certain copyright or related rights in it (the "Copyright") and s/he has given The University of Manchester certain rights to use such Copyright, including for administrative purposes.

ii. Copies of this thesis, either in full or in extracts and whether in hard or electronic copy, may be made only in accordance with the Copyright, Designs and Patents Act 1988 (as amended) and regulations issued under it or, where appropriate, in accordance with licensing agreements which the University has from time to time. This page must form part of any such copies made.

iii. The ownership of certain Copyright, patents, designs, trademark and other intellectual property (the "Intellectual Property") and any reproductions of copyright works in the thesis, for example graphs and tables ("Reproductions"), which may be described in this thesis, may not be owned by the author and may be owned by third parties. Such Intellectual Property and Reproductions cannot and must not be made available for use without the prior written permission of the owner(s) of the relevant Intellectual Property and/or Reproductions.

iv. Further information on the conditions under which disclosure, publication and commercialisation of this thesis, the Copyright and any Intellectual Property and/or Reproductions described in it may take place is available in the University IP Policy (see http://documents.manchester.ac.uk/DocuInfo.aspx?DocID=24420), in any relevant Thesis restriction declarations deposited in the University Library, The University Library's regulations (see http://www.library.manchester.ac.uk/about/regulations/) and in The University's policy on Presentation of Theses.

Acknowledgements

I would like to express my gratitude to my supervisor, Professor Brian Derby, who provided kind guidance and assistance throughout the whole duration of this journey. I also need to give my acknowledgements to my co-supervisor Dr Alexander Eggeman, who taught me a great amount of knowledge on TEM and crystallography. Both of my supervisors provided visionary advice and unconditional support in my study. They lead me to an interesting research area and taught me how to solve tough problems step by step. Without their incredible help this thesis would not have been possible.

I wish to acknowledge the technical supports provided by dir. Craig Williams. He helped me conduct the nanomechanical tests and gave me some valuable advice on experiments designs and data analysis. My thanks also go to Mr Andy Forrest, Mr Matthew Smith and Xiangli Zhong, who gave me some technical supports on nano-indentation, TEM and FIB. Special thanks to Andy Wallwork and Rachel Saunders for their kind help in my experiments and valuable suggestion on my projects.

Also, I would like to give my special thanks to my colleague Chongguang Liu for the fatigue tests support and Joe Neilson for discussing with me on thin film transistors. I gratefully acknowledge my other dear colleagues in my research group, including Halil Yilmaz, Hui ding, Jinxin Yang, Zixin Wang for their accompany and encouragements. My thanks also go to Dr Lijing Lin, Zelong Jin, Benjamin P. A. Gabriele, Chi Luo and all other friends in Manchester. I am proud to say that friendship is the most precious gains I obtain here. Besides, I am grateful to China Scholarship Council and EPSRC for their kind financial support of the research.

The most gracious thanks go to my parents and my girlfriend Ruidie, for the unconditional love that they gave to me and endless encouragements throughout my study. This thesis is dedicated to you.

This thesis would not have been completed without the help and encouragements of all involved. I really appreciate it and believe that “Gratitude makes sense of our past, brings peace for today, and creates a vision for tomorrow”.

List of figures

List of tables

List of List of Abbreviations

Nanopillars	Nanopillars are shaped structures with diameter in the approximate range 10 nm - 10 µm and with aspect ratio (diameter to the height) ranging from about 1:2 to 1:5.
NWs	Nanowires, structures with diameters in the range of nanopillars but with an aspect ratio greater than 50.
Nanowhisker	Nanowires with a very low density of dislocations.
ITO	Indium tin oxide
TB	Twin boundary
EBSD	Electron backscatter diffraction patterns
PED	Precession electro diffraction pattern
FCC	Face-centred cubic
BCC	Body-centred cubic
HCP	Hexagonal close-packed
LAGB	Low angle grain boundaries
HAGB	High angle grain boundaries
CSL	Coincidence site lattice
TEM	Transmission electron microscopes
FIB	Focussed ion beam
SEM	Scanning electron microscope
AFM	Atomic force microscopy
PTP device	push to pull device
MEMS	Micro-Electro-Mechanical Systems
DIC	digital image correlation

MD	Molecular Dynamics
DD	Dislocation Dynamics
PVP	Polyvinyl Pyrrolidone
CRSS	Critical resolved shear stress
SFD	Stacking fault decahedrons
AAO	Anodized aluminium oxide
SAED	Selected area electron diffraction
CCD	Charge couple cameral
GND	Geometrically necessary dislocation
CBED	Convergent beam electron diffraction
VBF/VDF	Virtual bright/dark field images
NMF	Non-negative matrix factorization
PCA	Principle component analysis
UTS	Ultimate tensile strength

1 Introduction

1.1 Background

Flexibility in electronic devices is very attractive for medical and bioengineering due to the intrinsic softness of living organisms. To make traditional rigid electronics flexible, it is necessary to replace traditional transparent electrodes made by Indium tin oxide (ITO), which is brittle. Metal NWs networks (like Cu and Ag) have attracted a lot of attention to replace ITO due to their mechanical flexibility, high conductivity, excellent optical performances and relatively low cost.[1–6] For example, Ag NWs electrodes prepared by continuous roll-to-roll coating on polymer PET substrate show controllable sheet resistances (30-70 Ohm/square) and optical transmittance values (89-90%) with high mechanical flexibility, making them suitable for making flexible touch screen panels.[4] Therefore, these metallic NWs networks have also been applied to various flexible electronics, such as flexible transparent film heaters,[6] semi-transparent solar cells,[5] polymer light emitting diode electrodes,[7] and wearable capacitive strain sensors[2,3] etc, and show excellent performances.

Among all the metal NWs, pentatwinned Ag NWs, which contains five segments joined along a common NW growth direction and each segment separated by twin boundaries, fabricated by polyol process are a promising choice because of their excellent electrical and optical performances, as well as outstanding chemical stability.[8–10] As the flexible electronics will be deformed many times in reality, research into the mechanical performance of these Ag NWs will be important to predict and improve the reliability of the fabricated device. On the other hand, as a basic science problem, metal NWs with twinning boundaries (TB) also have received much attention recently.[11–14] The influence of twinning on deformation behaviours of metals NWs are still unclear. Several interesting questions that are still under debate: (1) How do dislocations interact with TBs? Do TBs act as barriers or sinks for

dislocations in NWs? (2) Is the size effect of micro/nanoscale pillars/NWs, where the strength of the materials increases with decreasing diameter, changed or not due to the existence of TBs in NWs? (3) how do TBs influence the mechanical behaviours of NWs in different deformations modes.

To explore the deformation behaviours of pentatwinned Ag NWs, their microstructure should be characterized in detail. The key techniques developed for microstructure analysis are electron backscatter diffraction patterns (EBSD) and transmission electron diffraction in TEM.[15–19] The nano-scaled sample dimensions and high special resolution requirements in this study determine that transmission electron diffraction in TEM is a more suitable technique to observe the silver nanowires. Scanning (nanobeam) precession electron diffraction (PED) in TEM is reported to observed the microstructure of materials in nanoscale.[15,20] However, the special structure of pentatwinned Ag NWs decides that there are always two/three subcrystals overlapping for virtually all incident electron beam trajectories, making the obtained diffraction patterns a mixed set of data thus difficult to interpret. Machine learning techniques based on linear matrix decomposition algorithms are reported to be effective methods to achieve signal unmixing,[2116] but these methods have never been applied on pentatwinned Ag NWs to analyse the microstructures after deformation.

When applied in flexible electronics, Ag NWs are normally in form of networks.[22,23] The fatigue performance of Ag NWs in networks are directly related to the reliability of fabricated devices. However, there is limited research studying this problem systematically.[24] On the other hand, the loading conditions for Ag NWs in networks are believed to be complex, which may further result in different mechanical responses of individual NWs, although this hasn’t been reported in current research.

This project therefore has been motivated to study the mechanical performance of Ag NWs systematically to help understand the failure mechanism of fabricated flexible electrodes. The mechanical behaviours of individual Ag NWs are explored first. The influence of TBs in NWs is explored through a comparison the mechanical responses of pentatwinned Ag NWs and single crystal NWs subjected to different stress. Then Ag NWs in networks are tested under fatigue further explore the mechanical responses of individual Ag NWs under serving conditions. In particular, the focus is placed on understanding the deformation behaviours of pentatwinned Ag NWs at the microscopic level.

1.2 Aims and objectives

The principal aim of the thesis is to explore the mechanical responses of pentatwinned Ag NWs and underline mechanisms, thus extending our understanding of the impacts of sample size and the inner twin structure on the mechanical behaviours of metal nanowires. In applications, this work provides valuable insight on the failure mechanisms of flexible transparent electrodes fabricated by Ag NWs, which is necessary to predict and improve the reliability of flexible electronics made by Ag NWs.

1.3 Thesis outline

In order to achieve the above aims, the mechanical responses of Ag NWs under tension, bending and cyclic fatigue loading are tested separately. The impacts of TBs on the mechanical responses of Ag NWs are researched through comparing the mechanical responses of pentatwinned Ag NWs with single crystal Ag NWs. A summary of each thesis chapter is shown as follows:

Chapter 1 introduces the background and aims of this research. The thesis outline is also summarized.

Chapter 2 reviews the fundamentals of crystalline material deformation with an emphasis on the impacts of TBs on the mechanical responses of materials first. Then past work on research into the size effect of nanopillars/nanowires is summarized. The mechanical behaviours of metal NWs containing TBs are discussed in chapter 2.3. The work on fatigue behaviours of these metals NWs is discussed at the end of chapter 2.3.

Chapter 3 describes the materials fabrication process and the main characterization methods. Single crystal Ag NWs are fabricated by templates assisted electrodeposition methods. Scanning precession electron diffraction patterns and following data unmixing are introduced here, which is the main approach to characterize the deformed Ag NWs in this work.

In Chapter 4, the tensile behaviours of individual Ag NWs are studied. The displacement-stress curves of Ag NWs are obtained in in-situ SEM test. To explore the influence of TBs and sample dimension on the mechanical behaviour of Ag NWs, both single crystal Ag NWs and pentatwinned Ag NWs are tested in the same experiment conditions. The microstructures of deformed NWs are characterized under TEM to explore the underline mechanism.

Chapter 5 explores the bending behaviours of individual Ag NWs systematically. Pentatwinned and single crystal silver nanowires were bent in TEM for in-situ observations. The deformed structures are analysed using high spatial resolution scanning precession electron diffraction methods. Machine learning methods were used to determine the structure of the localised bends in the wires. Different deformation behaviours of single crystal nanowires and pentatwinned Ag NWs are showed under bending. A coincident site lattice model has been developed to explain the bending angles seen in individual nanowires and the observed distribution of angles in a population of pentatwinned nanowires. The geometrical constraints of the model explain the difference in this distribution when compared to that from a population of single crystal nanowires.

Chapter 6 focused on the fatigue performances of Ag NWs in networks. Through developing new sample preparation methods, the failure modes of NW networks are explored and studied quantitively using ex-situ TEM observations. The microstructure changes of individual NWs in networks in fatigue tests are analysed using PED followed by discussions on the underline mechanisms.

Chapter 7 summarizes the main conclusions obtained from the above research work. The future work is listed in the end to provide an outlook of this project.

2 Literature Review

2.1 Crystal deformation and the influence of twinning boundaries

2.1.1 Crystal defects and the pentatwinned structure

Understanding the deformation mechanism of metals is important for the safe design of all kinds of structures and devices, whether machines, buildings or electronic devices. For materials under load, if the constituent atoms return to their original positions after removal of the forces, the deformation is defined as elastic. If the applied forces are large enough for the atoms to overcome their local attractive forces, permanent displacement of the atoms occurs on unloading and this is known as plastic deformation. In crystalline materials this plastic flow is achieved through the sliding of crystal planes, hence the crystal structure of materials plays an important role in the deformation process.

Crystalline materials have a structure described by the repeating arrangement of atoms in three-dimensional space. The repeating unit that defines the crystal structure is termed the unit cell. Most metals display one of three densely packed crystal structures, which are: face-

centred cubic (FCC), body-centred cubic (BCC) and hexagonal close-packed (HCP) structures. In this work, the focus is on the mechanical response of an FCC metal, silver (Ag). During plastic deformation, deformation occurs through the sliding of the most closely packed planes along the direction with the highest possible packing density to reduce deformation energy. For FCC metals, like Ag, slip occurs on {1 1 1} planes along <1 1 0> directions, so there are 12 independent slip systems based on the symmetry of the crystal structure. When the loading is applied along the <1 1 0> direction for single crystal FCC metals, four slip systems are activated as the Schmid factor of the other slip systems is zero.

In practice, perfect crystals composed of a continuously repeated uniform unit cell do not exist, and there are always some deviations from the regular lattice. These are collectively known as crystal defects. Conventionally, defects are grouped into four categories: point defects, line defects, planar defects and column defects. [25] To facilitate the understanding of our research, line defects and planar defects will be mainly discussed in this review. Line defects, also termed dislocations, are of particular interest because under applied stress, the motion of dislocations allows slip of crystal planes and plastic deformation to occur.

Dislocations exist as closed loops inside crystals or emergent steps at the surface. The magnitude and direction of the lattice distortion associated with a dislocation is described by the Burgers vector, *b*, which is the same for any given dislocations along their length (Figure 1a). In crystals the orientations between the dislocation line and the Burgers vector can be various. When the Burgers vector is perpendicular to the dislocation line direction, the dislocation is called an edge dislocation. In this case the crystal defect can be considered as a half plane of atoms inside a perfect crystal (Figure 1a).

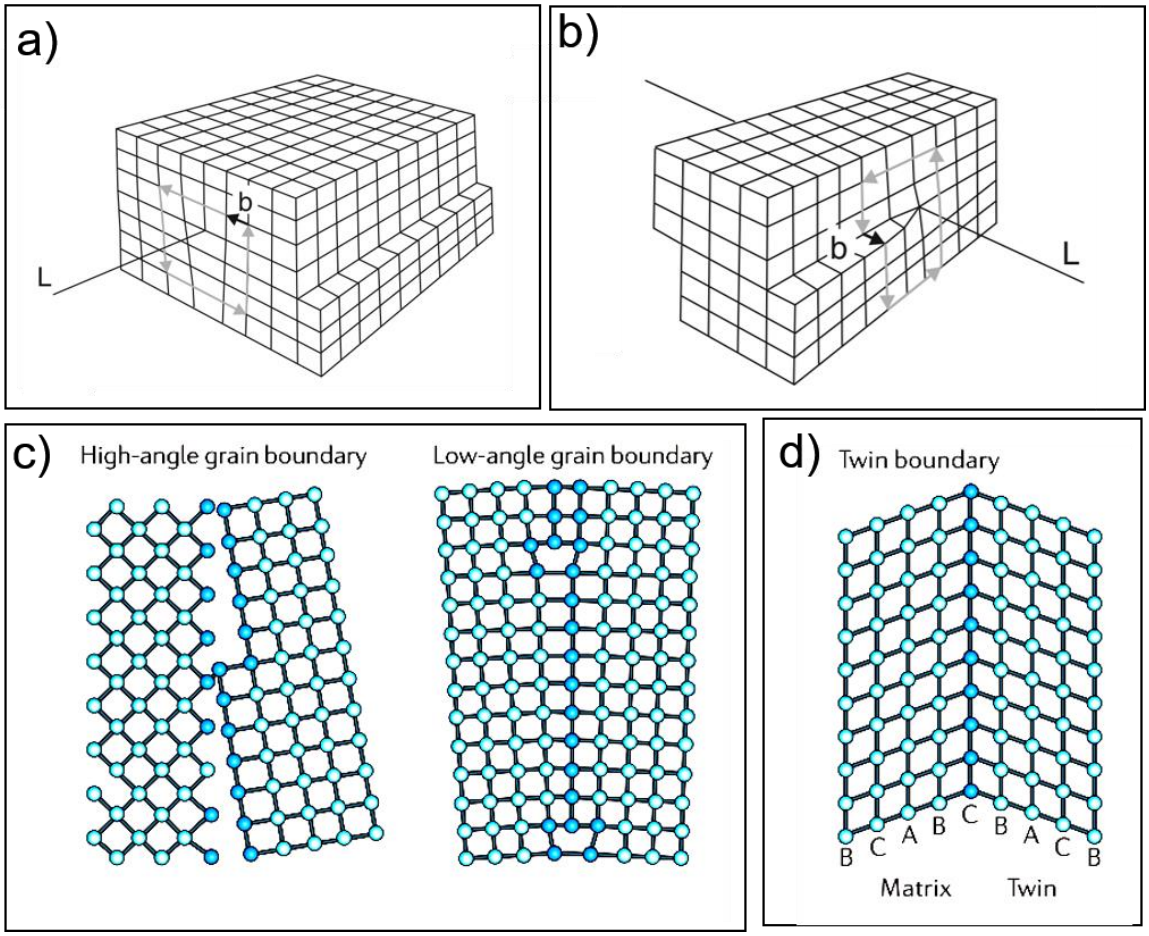

Figure 2-1 . Schematic of line dislocations (a-b)[26] and some planar defects (c-d)[27]. (a) Edge dislocation with Burgers vector perpendicular to the dislocation line (b) The screw dislocation with Burgers vector with Burgers vector parallel to the dislocation line. (c) Grain boundaries, which are classified to high-angle grain boundaries and low angle grain boundaries. (d) The twinning boundary.

When the Burgers vector is parallel to the dislocation line direction it is called a screw dislocation, which can be visualized by cutting crystal planes along a plane and slipping one half of a lattice vector along the other planes under shear stress. This comprises a structure where a helical path is traced around the dislocation line by the atomic plane (Figure 2-1b)). The motion of a dislocation along a plane (the slip plane) requires the plane to contain both the Burgers vector and the dislocation line, hence screw dislocations, with parallel Burgers

vector and dislocation line, can readily move between possible slip planes under applied stress.

Planar defects consist of grain boundaries, twin boundaries, free surfaces and phase boundaries. In bulk metals the grain boundary is the interface between two crystals of different spatial orientations. The grain boundary plane is normally considered to be a region of one or two atoms across in which the atoms are in a relatively disordered and strained condition compared to atoms within a perfect lattice, hence the free energy of the grain boundary is higher than the regular lattice. Grain boundaries are often classified by the relative angular misorientation between the two crystals into low angle grain boundaries (LAGB) and high angle grain boundaries (HAGB), as shown in Figure 2-1c). Generally, boundary misorientations with angle θ smaller than about 15 ^{o} are classed as low angle grain boundaries. The structure of LAGBS can be described adequately by an array of dislocations, which coexist in both crystal lattices at the boundary. As the misorientation angle θ increasing, the energy of a LAGB increases due to the greater total dislocation energy. In contrast the properties of HAGBs are normally independent of the misorientations, as the ordered nature of boundaries modelled by arrays of dislocations breaks down with increasing misorientation angle, θ, until above 15 ^{o} (for FCC metals) where the original grains must be considered to be separated into two distinct crystals.[28]

Grain boundaries can be simply analysed using coincidence site lattice (CSL) theory. For two grains misoriented by a fixed angle around an axis, there may be positions in one crystal lattice where an atom coincides with another site which is in the second grain (called a coincidence site). Owing to the periodicity of the two crystal lattices, there exists an array of these coincident sites called the CSL. The density of coincidence sites on a plane separating the two grains is described by Σ, and the value of Σ is defined as follows:

$$\Sigma = \frac{total\ number\ of\ all\ lattice\ sites\ in\ an\ elementary\ cell}{number\ of\ coincidence\ sites\ in\ an\ elementary\ cell} \quad (1)$$

For example, when one third of atoms in the grain boundary (Fig. 1d) is shared by both crystal grains, this boundary is a Σ3 boundary. Σ3 boundaries are often referred as twin boundaries, as they are related by simple crystallographic orientations related to the symmetry of the parent lattices. Twin Boundaries with very low values of Σ can sometimes be described as faults in the local stacking of crystal planes. This model assumes that the grain boundary energy is low when the number of coincidence sites is high, as the number of broken bonds across the boundary will be small.[29] Therefore, the twin boundary is thought to be a very stable crystal boundary as a result of a high density of coincidence sites.

The formation of twin boundaries can occur during crystal growth, annealing or mechanical deformation. Growth twins can appear during the growth of crystals with relatively low stacking fault energy, e.g. in Cu,[30] Au[31] and Ag,[25,32] or during recrystallization after deformation[33]. Deformation through twinning occurs under certain conditions: (1) low stacking fault energy; (ii) high strain rate; (iii) low deformation temperature and (iv) nanocrystalline grain size.[34] Pentatwinned Ag NWs, fabricated in polyol solutions,[32,35] are studied in this work. They have the potential to make flexible, transparent, conductive electrodes as a possible replacement for traditional ITO, because of their high conductivity, good chemical stability, superior fracture resistance and relatively low cost.[36–38] To better understand and predict the reliability of the flexible electrode made by NWs, this project focuses on the mechanical performances of pentatwinned Ag NWs.

Ag nanowires produced by the polyol process display a pentatwinned structure in which each NW has five twin segments joined along a common quintuple line in the axial direction <011>.[10] A schematic illustration of the structure is shown in Figure 2-2. According to FCC

lattice crystallography, the adjacent {111} twin boundaries in five-fold NWs have an internal angle of 70.53°, leaving a 7.35° deficiency when formed as a pentagonal prism.[39] This deficiency means that substantial internal strain can exist in pentatwinned NWs, also a surface groove may form along them in order to reconcile the strain.[40], The mechanical properties of pentatwinned NWs are expected to be significantly different to single crystal NWs, due to the existence of the twin-boundaries.[11] The existence of twin defects will influence the mechanical behaviours of materials through their interaction with mobile dislocations. To have a good understanding of the mechanical behaviours of pentatwinned Ag NWS, the interaction between TBs and mobile dislocations will be reviewed.

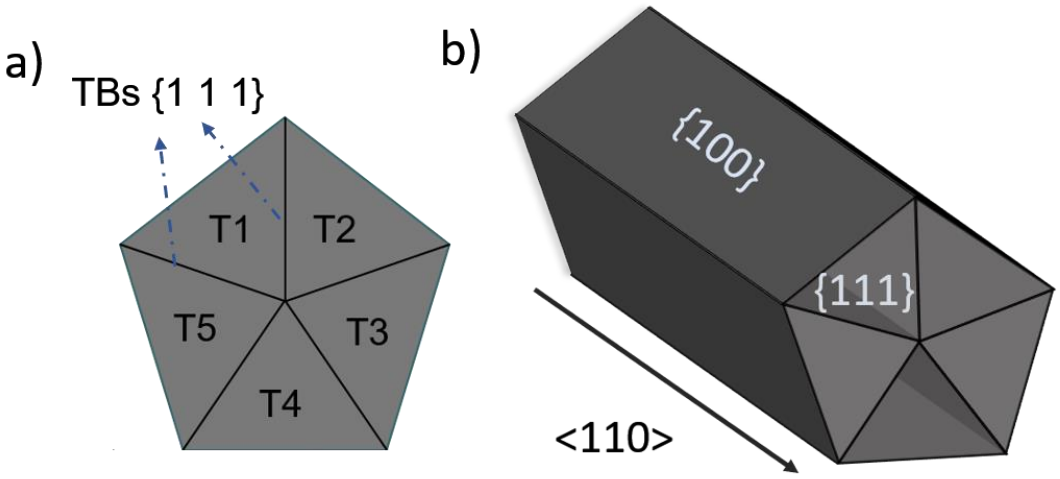

Figure 2-2. Schematic of the pentatwinned NW structure. (a) Cross-sectional view, showing subcrystals T1 to T5 connected by TBs in {1 1 1} planes. (b) Perspective view depicting the <110>-oriented NW containing {100} free surfaces.

2.1.2 The interaction between TB and dislocations

The general method by which metals are strengthened is the creation of obstacles/defects to block dislocation movement. For most strengthening methods, e.g. alloying, strength is normally improved at the expense of reducing ductility.[25,41] Twinning, especially nano-twinning, has attracted much attention in the past few years, as materials containing nano-twins have been reported showing high strength, while maintaining good ductility (14% for

Cu)[25,42–44]. A nanotwinned microstructure also shows much higher thermal and mechanical stability than microstructures with nanometre-sized grains.[27] This behaviour is attributed to the highly coherent structure of TBs. The twinning structure provides a barrier to dislocation motion and hence makes the strength of the materials increase. This is proved by observation of dislocation accumulation at the twinning boundary[45,46]. On the other hand, unlike the high angle grain boundaries that are so effective in obstructing dislocation movement (due to their disordered structures), TBs can allow dislocations to pass in some conditions and accommodate deformation, thus improving the ductility of materials.[47]

Knowledge about the interaction between dislocations and TB is necessary to understand the deformation mechanisms of nano-twinned materials. Based on the orientation of slip planes on both sides of the TB, the relationship of incoming dislocations and TBs can be classified into conjugated slip planes and unconjugated planes (Figure 2-3a).[48] On considering the dislocations that may react with TBs, four cases can be discussed respectively.[49] The two-dimensional Thompson tetrahedron is shown in Figure 2-3b. Taking ABC as the twin plane, dislocations on the other three planes on the tetrahedron have the same slip systems. If the dislocations glide on ABD planes, the four interaction cases are (1) a 30° Shockley partial dislocation, like the partial's Burgers vector Aγ forming a 30° angle to the dislocation line AB; (b) a 90° Shockley partial dislocation, like Burgers vector along Dγ; (c) a screw perfect dislocation with the Burgers vector parallel to the dislocation line; (d) a 60° perfect dislocation. Zhu et al.[49] systematically explored the reaction between dislocations and TB based on this classification, and listed all possible dislocation reactions and corresponding energy barriers. In this review, we mainly use the third classification standard to discuss the interaction between dislocation and TB: the TB planes direction with respect to the loading direction, as this will facilitate our next research on the mechanical properties of pentatwinned Ag NWs.

In the compression tests of columnar-grained copper Cu with preferentially oriented nanoscale twins,[46] loading directions with respect to the twin planes can be classified as perpendicular direction (Figure 2-3c-1), parallel direction (Figure 2-3c-2) and inclined direction (Figure 2-3c-3). Changing the loading direction with respect to the twin planes can alter the deformation mechanisms, thus affecting the yield strength and strain hardening.[46,50] Specifically, when the loading direction is normal to the TBs, dislocations starting from GBs first pile up against the TBs, then dislocations cut through the TBs under further deformation, which has been confirmed in post deformation transmission electron microscopes (TEM) images. When the loading direction is parallel to the TBs, the main plastic deformation mechanism changes to dislocations propagating along an inclined slip plane between two adjacent TBs. The shape of these dislocations under TEM is hairpin-like loops with Burgers vector parallel to the TBs. In the cases of 45 ^{o} compressions, the materials behave in a much softer manner than compared with the above two conditions, which is because the soft-mode slip is activated in this case when the resolved shear stress on the twin plane is maximized. Also, TB migration is observed experimentally because of the gliding of Shockley partial dislocations along the TB.

In addition to the interaction direction between the dislocation and TBs, the distance between two adjacent twin planes (the twin thickness) also has an important impact on materials strength and plasticity. It is found that the yield strength of electrodeposited Cu increases as the twin thickness decreases. This behaviour follows an empirical power law with an exponent identical to the empirical Hall-Petch relationship ($d^{-1/2}$) relating grain size to strength. [25,51] This size effect is thought to indicate that lower stress is required for thick twins because dislocations can form a pile-up to concentrate stress between the twins, while for thinner twin structures, such pile-ups are not possible, thus higher stress needs to be applied to make dislocations penetrate the TBs.[51] TEM observations reveal that few dislocations

exist inside the twin lamellae when the thickness is up to a few tens of nanometres, supporting the above assumptions. Similar to the Hall-Petch relationship, the size effect shows an inverse trend when the grain size is below 30 nm,[52] the strength of nano-twinned Cu also decreases when the twin thickness is smaller than 15 nm, as pre-existing partial dislocations at some TBs have a stronger effect on strength in samples with thinner twins. As to the strain hardening, the interaction between dislocations and TBs become the dominant mechanisms compared with dislocation-dislocation interaction in thick twin lamellae, leading to a higher strain hardening coefficient of nano-twinned Cu with twin thickness decreasing, so increased plasticity is observed in thinner twins, even though the twin thickness is only about 4 nm.[53]

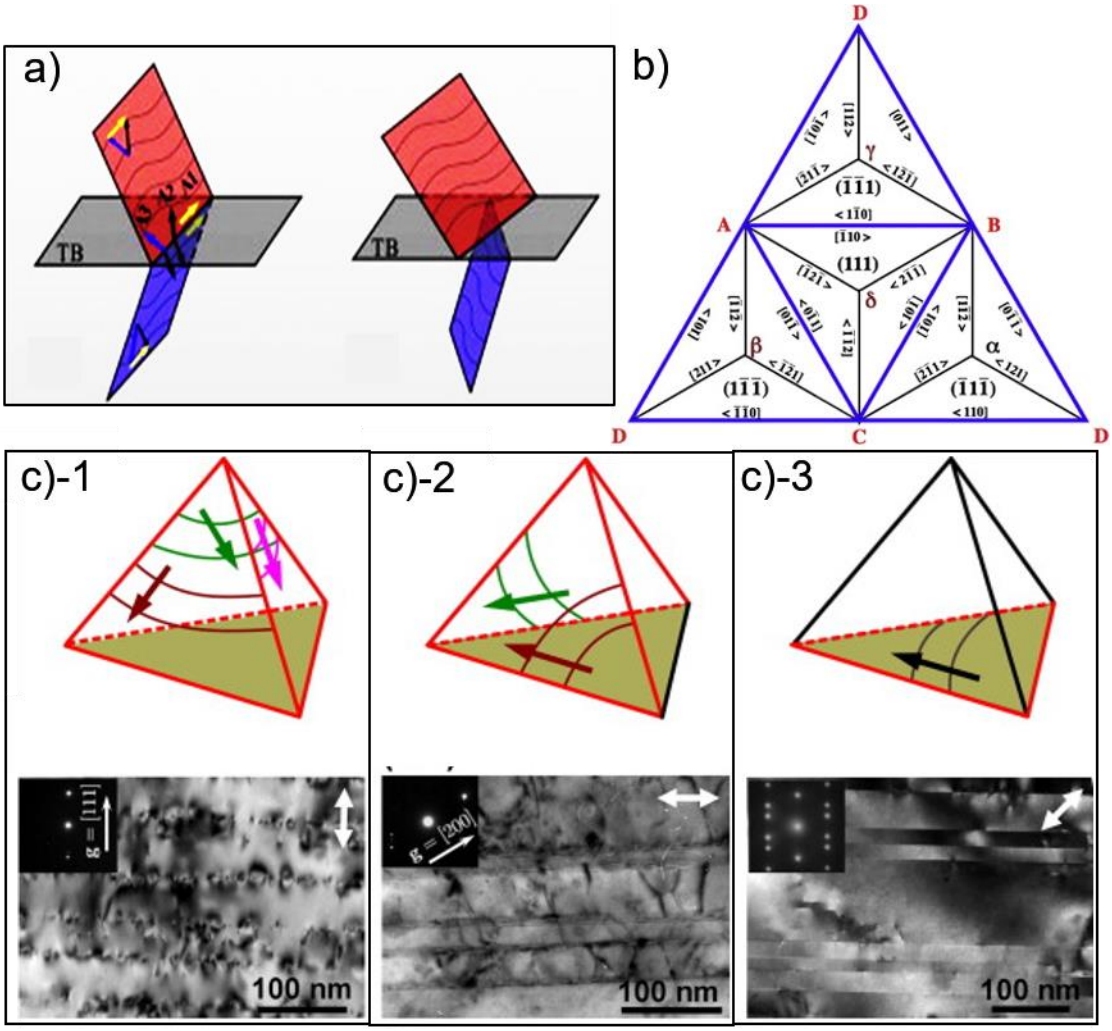

Figure 2-3. The classification on the interaction between TBs and dislocations. (a) TBs and the relationship of the slip systems (red and blue squares) on both sides. [48] (b) Spread Thompson tetrahedron with all the possible slip planes and the Burgers vectors of dislocations in FCC metals.[49] (c) Characteristic deformation processes in the nano-twinned Cu with compression axis oriented at 90°,0° and 45° with respect to TBs. Schematic diagrams illustrating the active slip systems for the three compression directions: c)-1, 90°; a)-2, 0°; a)-3, 45° and corresponding TEM images.[46]

2.1.3 Fatigue behaviour of metals with ultra-fine crystal grains or nanotwins.

In addition to understanding the role of TBs on dislocation motion, exploring the damage resistance and tolerance of nano-twinned metals is very important, as these determine the reliability of fabricated devices. Currently, most research is about the fatigue performances of

bulk metals/metal films with nano-scale twins. To our knowledge, there is limited research on the fatigue performances of nano-twins in NWs but a review of the fatigue performance of bulk metals with nano-scale twins can help us understand the underlying mechanisms.

Under cyclic loading, cracks nucleate from the surface of bulk metals followed by a period of growth until a critical crack size is reached, above which the materials fracture under the current load. Surface extrusion and intrusion contribute to the formation of persistent slip bands that serve as crack nucleation sites.[54] When the crystal grains decrease to nanoscale, the observed increased fatigue resistance of metals is widely attributed to the improved resistance to fatigue crack initiation.[54–56] In addition to the surface extrusions and intrusions, subsurface internal defects can also be crack nucleation sites, which is probably due to the decreased critical crack-length in nanocrystalline metals.[54] At the same time, the crack growth speed is higher in nanoscale grain microstructures compared with coarse grained metals because of the diminished resistance on the crack propagation. Several crack tip shielding mechanisms, like tortuosity of fatigue cracks and surface roughness induced crack closure, are decreased when the size of grains reduces to the nanoscale. Unlike high angle grain boundaries that hinder dislocation movement, it is observed that coherent twin boundaries not only provide a barrier to dislocations, but can also act as a sink or source of dislocations.[25] Therefore, as a special coincident site lattice boundary, the influence of TBs on fatigue performances is highly interesting and should be explored. Fatigue cracking mechanisms near twin boundaries were explored by Zhang et al.[48] , and they found that in Cu alloys with a high density of annealing twins, TB cracking is seriously affected by stacking fault energy, differences in the Schmid factors between matrix and twin, and the dislocation slip mode. After this, bulk Cu bi-crystals with a Σ3 TB fabricated through Bridgman growth have been studied to explore the cracking behaviour as influenced by TB orientation and the loading orientation.[50] [,57] Results shown that when the TB is parallel to the loading

direction(Figure 2-4a), incident screw dislocation composed of two Shockley partials can go through the TB under applied shear.[58] For TB perpendicular to the loading directions (Figure 2-4c), some slip bands hindered by the TB could also pass through.[49] In these two conditions, the strain incompatibility and stress concentration at the TB will be released through the passage of dislocations, so the crack resistance of TBs is higher than compared with high angle GBs and slip bands becomes the preferred crack nucleation sites. When the TB is inclined at 45 ^{o} to the loading direction (Figure 2-4b), slip bands parallel to the TB.

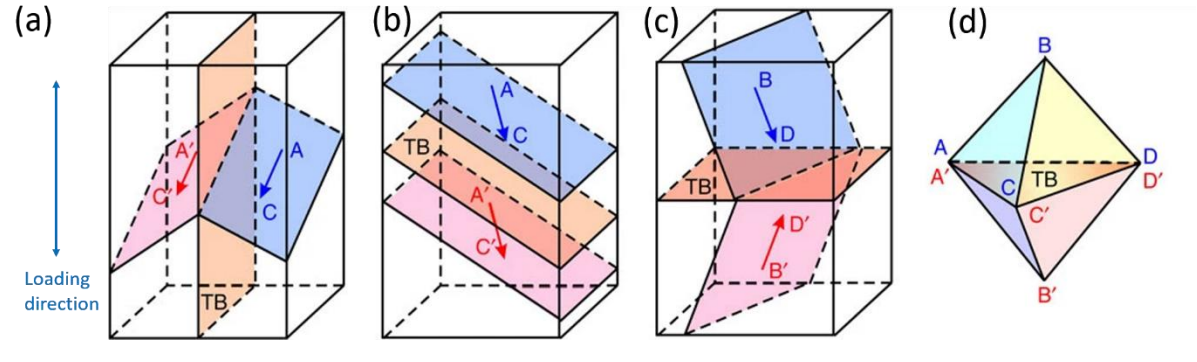

Figure 2-4 The TB and slipping systems relative loading direction. Primary slip systems predicted by Schmid's law for the bicrystals with a twin boundary (TB) (a) parallel (b) inclined at 45° and (c) perpendicular to the loading direction, respectively. (d) The double Thompson tetrahedron.

operate easily on both sides of the TB, and they are finally stopped and accumulate at the TB, leading to strain localization and subsequent crack nucleation under cyclic deformation.[57] Even though these results are observed in twinned bulk bi-crystals, they are still helpful for understanding the possible deformation mechanisms of NWs with TBs.

2.2 Uniaxial deformation of nanowires and associated size effects.

It is widely known that the internal microstructure dominates the mechanical responses of metals. In 2004, Uchic et al.[59] revealed that the physical dimension of materials also affect the strength and other deformation behaviours of metal pillars under uniaxial compression in the absence of deformation gradients. This reported a significant size effect with the plastic

flow strength of the pillars increasing as the pillar size decreased. Following this, further research confirmed the size effect in a number of different metals, however there is still not a widely accepted theory to reveal the underline mechanism of these observations. This thesis focuses on the tensile behaviour of metal nanowires. However, most of the exploration of the size effect reported in the literature is based on compression tests because of the relative ease of fabricating materials for small scale tests in compression rather than tension. Hence, the behaviour of nano/micron pillars under compression is reviewed first.

2.2.1 The influence of sample size on the compression behaviour of metallic pillars

Following the work of Uchic et al.,[59] many studies have revealed that the strength of metal micropillars is dramatically affected by their size. Greer et al.[60] found that flow stress of Au nanopillars, fabricated by focussed ion beam (FIB) milling, at 10% strain increases with reducing diameter, which is shown in Figure 2-5a. The smallest pillar tested, with a 400 nm diameter, reached compressive stress of 550 MPa. By comparing the results with electroplated Au pillars, they excluded the possibility that the increased strength was caused by Ga+ implantation into the specimen during milling. Afterwards, they published several papers for the improvement of the experiments and proposed the dislocation starvation theory[61,62]. The details of this theory will be discussed later. At the same time, Kiener et al.[63,64] also observed an apparent size effect on the flow stress of single crystal Cu columns (orientation <110>) with the side length in the range of 1 to 10 μm. Unlike the circular cross section of Greer, it is worthy to note that Kiener's work used a square-shaped cross section to avoid the variation in diameters of pillars due to the unavoidable taper that occurs during FIB milling.

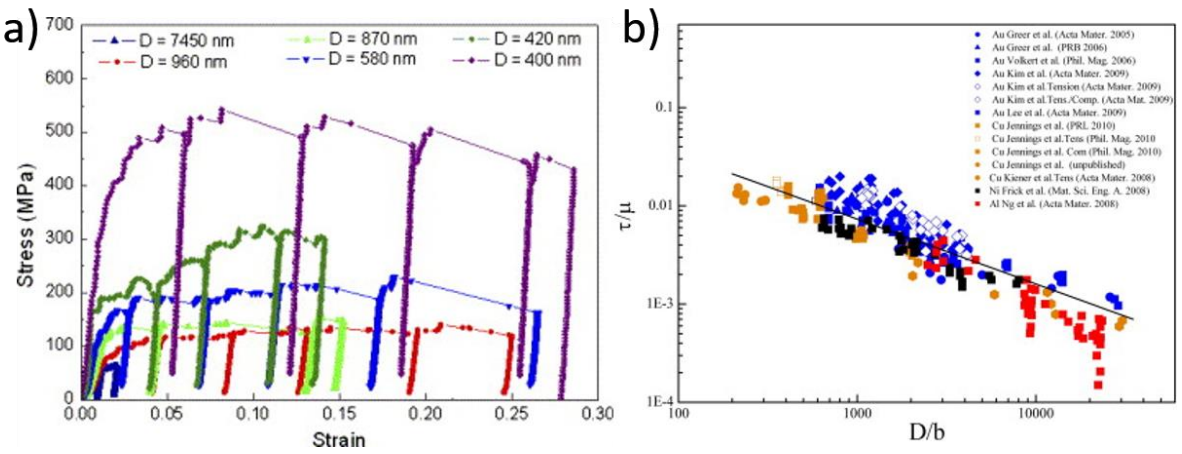

Figure 2-5 (a) Stress–strain curves of <0 0 1>-oriented Au pillars: flow stresses increase with decreasing diameters[60]. (b) Shear flow stress normalized by shear modulus on appropriate slip system in function of diameter normalized by Burges vector for FCC metallic pillars tested in compression and tension[65].

Based on the existing experimental results, some relations have been proposed to describe the relationship between the strength and diameter of pillars. For single crystal metal NWs, one of the empirical formulas is shown as follows[66]:

$$\frac{\sigma_{rss}}{\mu} = A\left(\frac{d}{b}\right)^{n} \tag{2}$$

Where σ_{rss} is the yield stress resolved onto the slip system with the highest resolved shear stress; for FCC metals {1 1 1} <1 1 0>), μ is the shear modulus resolved on the slip system; d is the pillar diameter and b is the magnitude of the Burgers vector; for FCC metals, A is 0.71 and the power law exponent n is about -0.66. This relation or a very close approximation to it, is seen following compression or tension tests on Au[67,62,60,68], Cu[63], Ni[69] pillars or wires (Figure 2-5b). This formula is presented based on the opinion that the controlling physical property for dislocation motion is the dislocation line tension, which is determined by its Burgers vector and the elastic modulus. It is coherent with published strength data and widely recognized. However, it is an empirical relationship with no theoretical foundation.

Besides the effect of sample diameter, the original dislocation state in pillars is found to have an impact on the strength of micro/nanopillars. The dislocation densities inside the samples

are controlled through pre-straining (high dislocation density) and annealing (low dislocation density) of Au nanopillars[70]. Compression tests show that the flow stress decreases after pre-straining and recovers to pristine pillars level after annealing to pre-strained samples, which is controversial to the traditional strain hardening in bulk metals. It is believed that the plasticity is controlled by the sources of dislocations in the pillars, leading to a reduced strength for samples already containing dislocations. Apart from these, there are also many questions that need to be explored on sample dislocation states, like dislocation nucleation sites and the form of dislocations in nanopillars (partial dislocations or single armed dislocations). These will be discussed in detail later.

Jennings et al.[71] studied the effect of strain rate on the deformation of micropillars. The results clearly indicated that both sample size and strain rate can affect the stress of Cu pillars, as shown in Figure 2-6 a. Also, the slopes of stress vs. strain rate are different for different pillar diameters. Stress data at 10% strain as a function of diameter is extracted from Figure 2-6a and presented in Figure 2-6b. Burgers vector b and shear modulus μ are constant in this experiment. According to Eq. (2), the power law exponent n describing size effect also changes with strain rate.

Above all, even though there seems to be a relatively constant power law exponent for all FCC metals, the strength of the micro/nanopillars is still variable due to some parameter differences, such as dislocation density and strain rate, leading to different power-law exponents. More attention should be paid when testing the NWs and analysing the data to explore the size effect.

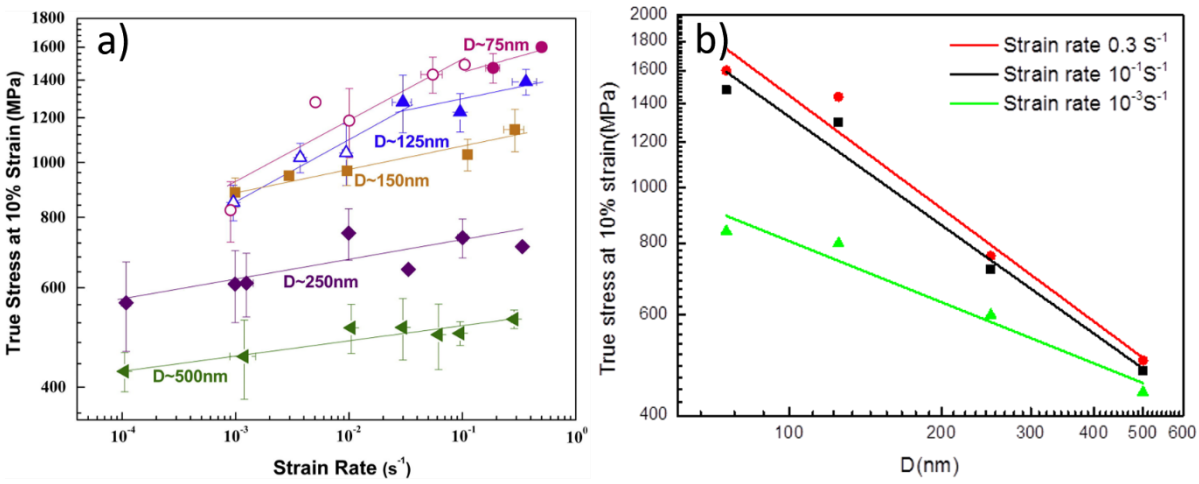

Figure 2-6 (a) Flow stress of Cu pillars at 10% strain as a function of strain rate for five different diameters shown around each data set. Two smallest diameters, 75 and 125 nm, show a discrete transition[71] .(b) Stress at 10% strain as a function of pillar diameter for Cu pillars under different strain rates. The data is extracted from Fig 4 (a).

Along with the size effect, deformation by strain bursts (seen in Figure 2-5) is another characteristic feature of metal pillar deformation compared with bulk materials. It is universally observed in micro/nanopillars under compression. A single large strain burst after elastic loading can, for example, be caused by twinning, dislocation slip distributed over the whole pillar volume, or localized dislocation slip. For micropillars, there are many dislocations inside, so a deformation burst should involve the motion of a large number of these dislocations. It is proposed that in microcrystals some dislocations can be mutually trapped due to crystal lattice constraints, and the strain busts may be the results of the destruction of this jammed configuration.[72,73] A slightly increased dislocation density after deformation is observed under TEM, which is thought to be the evidence of dislocation accumulation caused by mutual obstruction.[72] The potential physical mechanism for the nanopillars is explained by the competition of dislocation nucleation and annihilation rates, i.e. dislocation starvation theory.[60] The deformation stress increases when the number of active dislocations is insufficient to accommodate the deformation rates, allowing the nucleation of new dislocations. If there are enough mobile dislocations to accommodate the

imposed deformation, a stress drop will be observed. The load fluctuation accompanied by dislocation bursts has been captured in Ni pillar (150-400 nm) tested in situ in the TEM [74].

It seems that the strain bursts are reasonably explained by two mechanisms depending on the relative diameter of the specimen. However, the transition point for these two mechanisms is not clear. Frick et al.[69] found that the relationship between strain burst length and pillar diameter is not obvious. Another research revealed that the strain burst size becomes more scattered in TRIP steel pillars when the diameter changed from 0.5 to 3 μm[75]. These results indicate that we do not have a full understanding of the mechanisms leading to strain bursts. Other factors, like original dislocation source[76], strain rate[71] and temperature[77], can also result in a change of strain burst behaviour. On comparing the behaviour of submicron Ag pillars fabricated by nanoimprinting and FIB, found that the imprinted pillars showed more pronounced strain bursts, which may be because the better surface finish of the imprinted pillar surface leading to fewer dislocation sources for plastic deformation [76]. Due to the difficulty of carrying in-situ compression test in TEM, as well as recording mechanical responses simultaneously, only limited data on microstructure observation has been reported, so more in-situ structure characterization is needed to further confirm the above theory.

Strain hardening means that the strength of materials increases with increasing plastic deformation. In bulk materials, this is due to dislocation movement and dislocation multiplication, while for submicron/nanopillars, dislocations can only travel for a short distance before annihilating at the surface, leading to a smaller dislocation multiplication rate. Some studies show that the strain hardening effect in nanopillars is not obvious in FCC,[78, 79] and the hardening in the initial part of the stress-strain curves of Au [001] single crystal pillars is thought to be caused by the imperfect contact between the indenter and the top of the pillar. [79] This supposes that dislocation starvation (discussed later) is the predominant deformation factor in FCC nanopillars. In another compression test of FCC Ag nanopillars,

strain hardening is also not observed in submicron pillars, while large nanopillars (diameters above 2 μm) show strain hardening like the bulk materials[76].

However, strain hardening in some FCC nanopillars, [111] Ni nanopillars for example, was observed in some research. The strain hardening rate of these samples increases with diameters decreasing from 2 μm to about 200 nm.[69] It was proposed that the size effect of strain hardening is the combination of dislocation entanglement and increased stresses required to activate dislocation sources with decreasing size scale. Higher dislocation activation stress for smaller wires may explain the strength increase for smaller pillars, but this assumption did not fully explain why strain hardening appeared in FCC Ni nanopillars, as preformed crystallographic slip steps may serve as new nucleation sites to eliminate subsequent strain hardening.[78]

2.2.2 Sample fabrication for tension and test methods

Compression tests on metal nanopillars have been widely conducted in the past few years. However, the pillars prepared for compression tests have a limited aspect ratio to prevent buckling under compression, and it is difficult to fabricate pillars with the diameter of about or below 100 nm. Other problems, such as constraints rising from friction where the load is applied and compliance of the sample base also introduce some uncertainties to test results, promoting researchers to explore new methods to conduct tensile tests to study the performances of nano-sized one-dimensional materials. [80–82] The development of flexible electronics has promoted research on the failure mechanism of conductive flexible transparent electrodes made by metal NWs. Since the failure of nanowire networks is predominantly the results of tension loading,[83,84] it is necessary to carry out these tests in tension. The tensile testing of individual metal NWs is very challenging experimentally due to the difficulty in sample preparation.

In 2007, Kiener et al.[81] reported a new method to perform tensile tests on single crystal copper specimens with side lengths from 0.5 μm to 8 μm. Rods cut from bulk materials by a diamond wire saw were mounted on Cu holders for FIB shaping. Then these samples were milled into a dog bone shape with a square cross section (Figure 2-7a). A lower current beam was used after initial coarse milling to minimize the ion-induced damage. Subsequent tensile tests were performed inside the SEM using a micro-indenter. In order to perform tensile loading and ensure a good connection between the indenter and samples, the indenter was equipped with special dovetail-shaped tips serving as the sample gripper. This method was subsequently adopted by Kim and Greer afterwards[68]. The disadvantage of this method is that it is hard to fabricate small wires with a diameter of about 100 nm using FIB. Afterwards, Jennings et al.[82] fabricated samples through electrodeposition with intentional over-plating to achieve a "mushroom" end, and the sample diameters could be reduced to 75 nm. After reinforcing the connection between the substrate and the pillar bottoms using tungsten hexacarbonyl deposition, the pillar tops are gripped by a special shaped indenter to load in tension. However, it is not easy to get a mushroom cap with a proper size, and the crystal orientation and dislocation states are hard to control through electrodeposition.

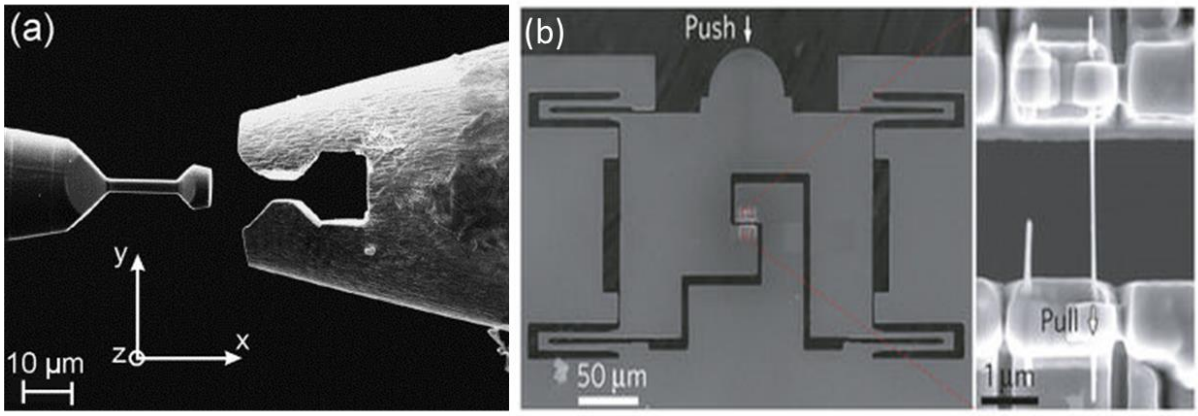

Figure 2-7 (a) SEM image showing a single-crystal Cu tension sample and the corresponding tungsten sample gripper[81]. (b) Push-to-pull device with a secured NW[85].

To perform the tensile experiments, the use of a nanomanipulator inside the FIB is also described in some reports[86–90]. Normally, a nanomanipulator is installed in a FIB system. One end of the NW is fixed on the nanomanipulator using Pt deposition; the other end is attached to AFM silicon cantilever or other fixed parts to measure the applied force in the SEM. The force can be read out from the manipulator or from the bending of the AFM cantilevers. Zhu et al.[89,90] used this way to test the mechanical properties of silicon and Ag NWs inside a SEM. Samples were clamped between the manipulator and Si wafer in the SEM chamber; both force and elongation were directly measured from the SEM images. It is easy to test samples with relatively simple equipment compared with other methods. The drawbacks are also obvious, such as difficulties in specimen alignment and applying loading with a uniaxial force.

(3) Thermal actuators

In 2007, Zhang et al.[91] designed a testing set-up which is mainly composed of two plates. Because of the difference in thermal expansion coefficients, these two plates bend in opposite directions serving as deformation actuators when heated in the TEM. It was first used to test the super-plasticity of SiC NWs. Then It is also developed to observe the tensile deformation of Cu NWs [92] and metal glass [93], but the stress data cannot be obtained using this technique.

(4) Push to pull device

The push to pull (PTP) transformer serving as a micro/nano-mechanical test system for tensile testing was developed by Hysitron, Inc[94]. The PTP device is microfabricated on a silicon-on-insulator wafer and made of two parts. They are connected by flexible elements which ensure that the force loaded on the PTP device is linearly proportional to the displacement length imposed on the outer surface (Figure 2-7b). The two ends of samples to be tested are firmly fixed on the two parts of the device separately by FIB deposition of

platinum (Pt) patches. Through the force and displacement curves obtained from the nanoindenter, combined with the known stiffness of the PTP device, the stress and strain state of the samples is measured accurately. Guo et al.[95] used this device to test elastic properties and structural phase transitions of single VO_2 nanowires under in situ TEM. The tensile deformation performances of Mo and Pb were also obtained through the PTP device. [96,85] Through in-situ TEM observation, the distribution and movement of dislocations can be explored. This device makes it possible to test NWs with a very small diameter using pico-indenter, and the tests experiments can be conducted both in SEM and TEM, so it is adopted to test the tensile behaviours of individual Ag NWs in this research.

Other advanced equipment has also been adopted for tensile testing NWs specimens. Chen et al.[97,98] mounted an individual NW onto a Micro-Electro-Mechanical Systems (MEMS) tensile testing stage in a SEM. This was actuated by Joule heating-induced thermal expansion of polysilicon chevron beams. Forces on the specimen and their elongations were deduced from displacements of compound flexure beams of polysilicon on the opposite grip and digital image correlation (DIC) of images separately. A detailed image of the MEMS device can be seen in Figure 2-8.

.

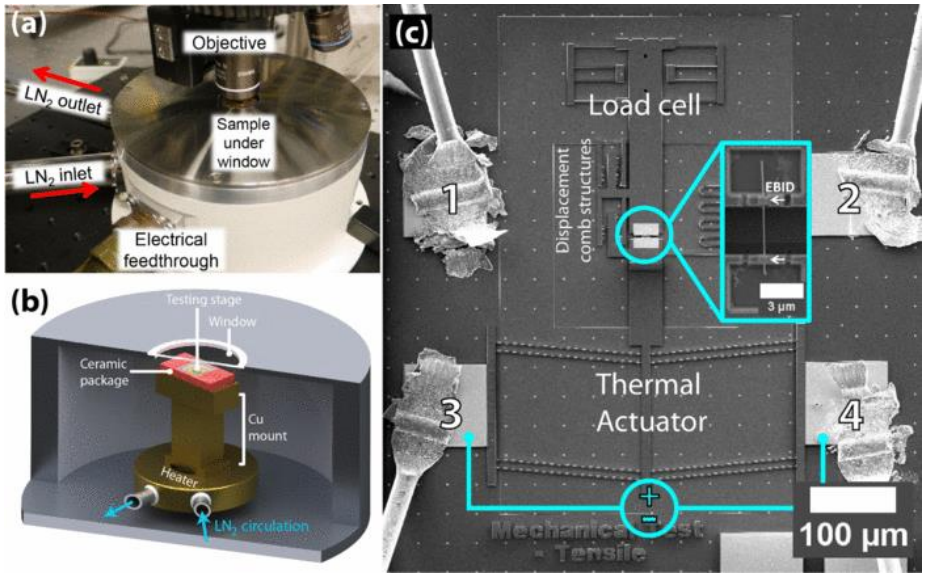

Figure 2-8 (a) Picture of the vacuum cryostat setup under the optical microscope. (b) Schematic of the inner chamber. (c) SEM micrograph of the MEMS-based tensile testing stage. Inset shows a zoom of the grips after attaching a Pd NW specimen using Pt-containing deposition[98].

2.2.3 Size effects for NWs tested under tension and comparison.

A size effect has also been observed in tension tests of NWs with diameters in the range of tens of nanometres to micrometres in FCC metal such Cu[81,99,82], Au[68], Ag[100,10]. The ultimate tensile strengths of NWs follow a similar power law dependence on diameter as reported with compression studies on FCC metals micropillars. To explore the mechanical test result differences between compression and tension, Kim and Greer[68] compared the mechanical properties of metal nanopillars fabricated by FIB under compression and tension. Similar tensile and compressive flow stress was observed in Au except for that shorter, slower discrete strain bursts and more pronounced strain hardening was seen with the tension test. This was explained by differences in testing methods and sample geometry, e.g., different contact areas, constraints between samples and grips/indenters during testing and different aspect ratio. Similar analysis was also concluded by Kiener et al. [101]. By electroplating Cu into porous polymethyl methacrylate (PMMA) templates, Cu nanopillars were produced and tested. No tension–compression asymmetry was showed in the tested range (75nm to 165

nm)[82]. Thus tension-compression asymmetry was not found to exist in FCC metals regardless of the fabrication method of samples.

2.2.4 Dislocation behaviours inside NWs under mechanical tests.

2.2.4.1 Dislocation nucleation and the effect of initial dislocation states

In bulk materials, the deformation behaviour is controlled by dislocation interactions. When the size of the NWs is decreased to the nanoscale, the sample width limits the distance that a dislocation moves inside samples, thus decreasing the possibility of dislocation interaction, so the dislocation nucleation becomes the dominant process. To have a better understanding of dislocation nucleation, a review of research on the form of nucleated dislocations, nucleation sites and the relationship between NWs strength and nucleation, is necessary.

Generally, three are three kinds of surface nucleation: (1) a full dislocation, with complementary leading and trailing partials (2) a single leading partial dislocation and (3) deformation twinning.[102] Current research indicates that sample size has an impact on the kinds of dislocation nucleation occurring. In bulk materials, dislocations are believed to originate from the double-pinned Frank-Read source. With the sample diameter decreasing, it has been proposed that the double-ended source will by truncated be a free surface upon operation,[103] and the possibility of dislocation multiplication is also reduced. A single armed dislocation source has been observed under TEM for submicron samples with a diameter above 100 nm.[80,104] Further decreasing the samples size is believed to result in partial dislocation nucleation becoming the dominant deformation mechanism for metal NWs.

When the NWs are deformed under tension, both a single leading partial dislocation and deformation twinning are widely observed in experiments. The former deformation modes lead to the brittle failure of pristine NWs, like Cu[86] and Ag[13,105] (Figure 2-9 a). In the second case, defect free Au, Pt and Au/Pt NWs with diameters from 40 to 250nm shows ductile

behaviours through long range twinning propagation (Figure 2-9b).[88] Size dependent twin propagation stress is also found in this experiments, which is supposed to be related to the differences in surface energy. Deformation through twin propagation is not only found in materials with low stacking fault energy, but also observed in Al NWs.[33] These two different deformation modes are believed to be determined by the competition between the energy barrier for twinning and the barrier for slip.[33,105] It has been shown that the pre-existing structures and shape of the cross section (e.g. width and length aspect ratio) are the factors that affect the energy barrier, but more research is still needed to have a complete understanding of underlying mechanisms. It is notable that deformation twinning of FCC samples is only be observed in nearly defect-free NWs, which should be because that twinning requires higher stress for activation than slip in FCC structure metals.

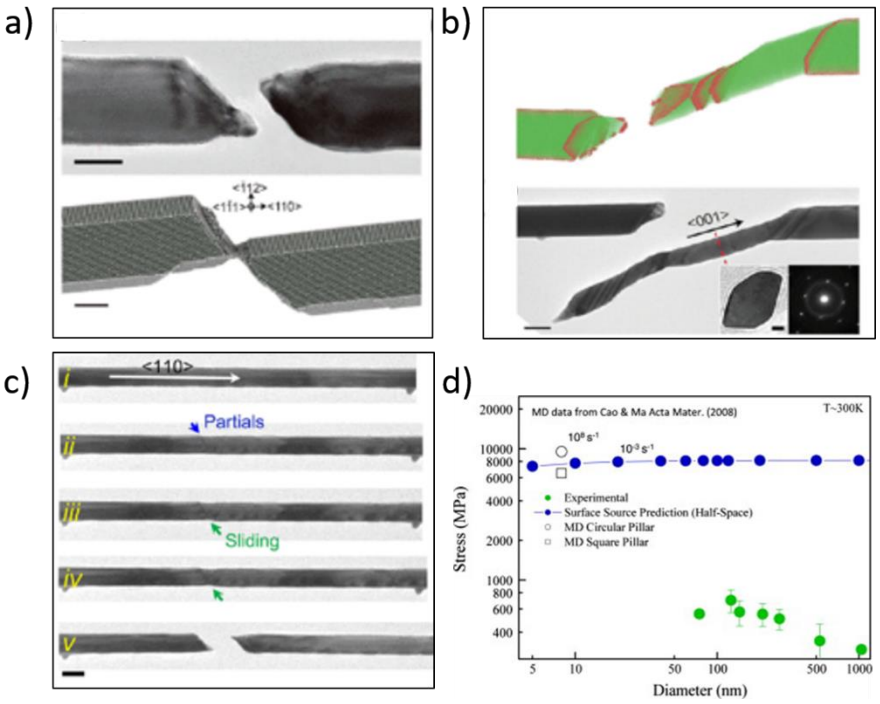

Figure 2-9 (a), (b) is the fractured Ag NWs failed through slipping and deformation twinning.[106] (c) shows the nucleation of partial dislocation from the surface of Ag NWs.[106] (d) The strength of Cu NWs from modelling and experiments.[107]

For single crystal NWs, the surface is thought to be the preferred nucleation site for partial dislocations when the sample size is at the nanoscale. This has been widely predicted in

simulation, [108,107] and observed under TEM for Au and Ag NWs (Figure 2-9c).[92–94] The dislocation nucleation strength of several pristine FCC NWs is calculated using the model developed by the Jennings et al.[107], but the strength is a factor of 10 larger than the strength tested through experiments (Figure 2-9 d). This is explained because the model assumes that the NWs have a perfect lattice structure, while there are defects on the surface of the tested Cu pillar fabricated by electrodeposition and the non-zero dislocation density affects the internal elastic fields of pillars. Compared with pillars made by electrodeposition, the NWs grown under near-equilibrium conditions are of high crystalline quality, and no pre-exiting dislocations are observed under TEM.[85,110] Research shows that the tested strength of Pd is also lower than the value from nucleation-controlled strength theory, as the calculated activation energy based on experimental data is more than an order of magnitude lower than the simulation results.[85] It is possible that some surface defects are not detected, such as atomic surface steps and vacancies, but their activation energy is higher than the calculated values based on experimental results, so the surface diffusion is deemed to serve as a precursor to dislocation nucleation. This may be the reason that the tested strength of Pd whiskers do not present diameter, length and strain rate dependence, but is sensitive to temperature changes. Although some atomic modelling work predicts a difference in the strain rate sensitivity of nucleation stress, the weak size dependency of nucleation is also found theoretically, [102] consistent with the above work. Therefore, the power-law exponent of the size effect is expected to be lower below 100 nm when dislocation nucleation dominates the deformation. This has not been observed in experiments due to the difficulty in testing NWs below 100 nm.

Apart from nucleation, most of these publications show that the initial dislocation state has a strong impact on the mechanical performance of metal NWs. C. Chisholm et al.[96] adjusted the dislocation density of Mo NWs (150-550 nm) by pre-straining. They observed that

dislocation free NWs deformed elastically before abrupt yield, and heavily pre-strained NWs with high dislocation density showed continuous plastic deformation after the yielding at lower stress. In NWs contained intermediate density of dislocations, exhaustion hardening followed by catastrophic yield was confirmed, which can be explained by self-multiplication process. In addition, the initial dislocation state can also lead to different performances in strain rate sensitives. In the tension test of Cu NWs fabricated by FIB, strain rate sensitivity is obvious and higher than electro-deposited Cu pillars in compression[99,71]. It is apparent that the initial dislocation status of the two kinds of samples is different, which leads to different performances. However, there are still some questions that need to be solved, such as:

1. How does dislocation density affect the mechanical performance of NWs? Will the dislocations interact with each other under high density, even at the nanoscale?

2. Is the size effect strongly related to the dislocation density? If yes, what is the critical point of that density?

More research is necessary to explore these problems.

2.2.4.2 Partial dislocations and single-armed dislocation sources found in NWs with different diameters.

Exploring the form of dislocations during deformation is critical to understand the plastic deformation process. In the present research, operation of single armed dislocation and nucleation of partials dislocation, mainly referring to Shockley partials dislocation have both been observed in metal micropillars, which identify different mechanisms. Partial dislocations are normally present as a decomposed form of a perfect dislocation within materials. Shockley partial dislocations generally refer to a pair of dislocations on a single slip plane of FCC materials separated by a stacking fault of width l_c. The length l_c can be

determined by equation 2-1,[111] which is calculated through comparing the critical stress of producing partial dislocation and full dislocation based on classic dislocation theory[112].

$$l_c = \frac{2\alpha\mu(b_F - b_P)b_P}{\gamma} \qquad (2-1)$$

Where α reflects the character of dislocations (0.5 for the edge dislocation and 1.5 for the screw dislocations[112]); b_F and b_p are the magnitudes of Burgers vectors of the full dislocation and the Shockley partial dislocation; μ is the shear modulus and γ is the stacking fault energy. This equation shows that an increase in stacking fault energy for materials will be reduced the critical distance between two partial dislocations, as the repulsive force of two decomposed partial dislocations can be offset by the stacking fault to produce stable structures. With the sample size decreasing to below l_c, it is no longer possible for the wire to contain a pair of partial dislocations. For silver, research suggests that partial dislocation will replace full perfect dislocations below a critical length of 60 nm.[111]

Although the critical length can be calculated from equation 3, experimental results on dislocation nucleation and movement are still important to verify the theory. TEM observation is thought to be a direct way to capture the dislocation movements. On the other hand, simulation also plays an important role in advancing the understanding of the mechanical behaviour of nanometals. Both Molecular Dynamics (MD) and Dislocation Dynamics (DD) models have been used in previous work. In MD simulations, atoms are the basic unit and their position deviations from the ideal lattice sites represent dislocations. Atoms interact with each other through interatomic potentials and reducing the total potential energy of the system is the principle of the simulation. As computational power limits the number of atoms that can be modelled, the simulation size is constrained (< $(200\ nm)^3$). DD simulations originate in modelling the plastic deformation of bulk materials. In this model, dislocation lines are the important elements, which are regarded as an elastic inclusion

embedded in an elastic medium. When the loading is imposed, the movement and interaction of dislocation lines are modelled using the elastic properties of the materials. When using DD to model the deformation of micropillars, the impact of image stresses on the dislocations due to the free surface needs to be considered[113]. Table 2-1 summarizes experimental and simulation studies of single-armed dislocation sources and partial dislocations during the deformation of micro/nanopillars or wires.

Table 2-1 Summary of prior work on the deformation mechanisms of micropillars reported in the literature.

Metals	Diameter(D)	Initial Size/density of dislocations	dislocations	Modelling or Experiment
Al	420 nm (square)	$\sim 2\times10^{13}\ m^{-2}$	Single-armed dislocation	Experiment[80]
	750 nm	$\sim 4\times10^{14}\ m^{-2}$		Experiment[114]
Cu	100-200 nm	$5.6\pm0.3\times10^{14}\ m^{-2}$	Single-armed dislocation	Experiment[104]
cubic cells	4-10 μm	$2\times10^{12}\ m^{-2}$	Single-armed dislocation, 1 μm source exhaustion	3D-discrete dislocation simulations (DDS)[115]
cubic cells	0.5-1 μm (square cross section)	$\sim 2\times10^{13}\ m^{-2}$	Single-armed dislocation,	3D-DDS[116]

Au	~10nm	Carved	Partial dislocation (Shockley)	MD simulations [117]
	2-5nm (square cross-section)	none	partial dislocation	atomistic simulations[118]
	< 10 nm	none	partial dislocation	Experiment[119]
Pt	43 nm	none	Partial dislocations	MD simulations[120]
Ag	1-25 nm (pentatwinned)	none	Partial dislocations	MD simulations[121],[122]
Ag	<100 nm (pentatwinned)	none	Partial dislocations (Shockley)	Experiments (stacking fault decahedrons)[13]

From this survey of the literature, we can conclude that single armed dislocation sources are normally observed in nanopillars with larger diameters and simulated using DD models. Partial dislocations are found in low stacking fault energy materials when the pillar diameter is < 100nm, such as Au, as perfect dislocations tend to split into ribbons bounded by the leading and trailing partials to reach the lower energy status[123].

2.2.5 Mechanism models for the size effect of FCC metals

(1) Dislocation starvation theory

A number of models have been proposed to explain the deformation process in NWs[62,80,96,104,109]. Among these, dislocation starvation has drawn much attention[62,60]. This model is proposed based on the observation of compression experiments and can be extended to explain the size effects of metal NWs under tension. Specifically, the model assumes that in small diameter specimens, dislocations can travel only very small distances before annihilating at free surface without interaction. When a pillar is loaded to stress sufficient for dislocation motion, its density will decrease sharply because dislocations leave the crystal more rapidly than they multiply, forming a dislocation starvation state. To continue the plastic deformation, higher stress is required to promote new dislocation nucleation processes. This model has been supported by many experimental results[96,76]. Shan et al.[74] observed mechanical annealing in single-crystal Ni pillars ranging from 150 to 400nm through in situ TEM experiments. The density of dislocations was observed to decrease during compression tests and dislocation free nanopillars were found in some situations. The extent of mechanical annealing is related to the sample diameter and thus corresponds with smaller being stronger. These observations provide direct evidence for dislocation starvation. Moreover, some molecular dynamics modelling has also found that a dislocation starvation state can be reached after some dislocations escape from Ni NWs between 4-16 nm diameter, resulting in elastic deformation until new dislocations form[124]. This provides atomic-level simulation support for the proposed dislocation starvation model. It is worth noting that dislocation starvation means that the density of dislocation decreases but not to zero under TEM. The definition of a starved state in the dislocation starvation model is not very specific. It is just a state that requires new dislocation nucleation to accommodate the deformation process.

(2) Source truncation/ single arm theory

In 2007, Parthasarathy et al.[103] tried to explain the size effect by considering the stochastics of dislocation source lengths in finite sample diameters. When the sample dimensions are

decreased to the size that is similar with the length of the dislocation source, all sources can potentially interact with the free surface forming single-ended shape, which can be seen in Figure 2-10.

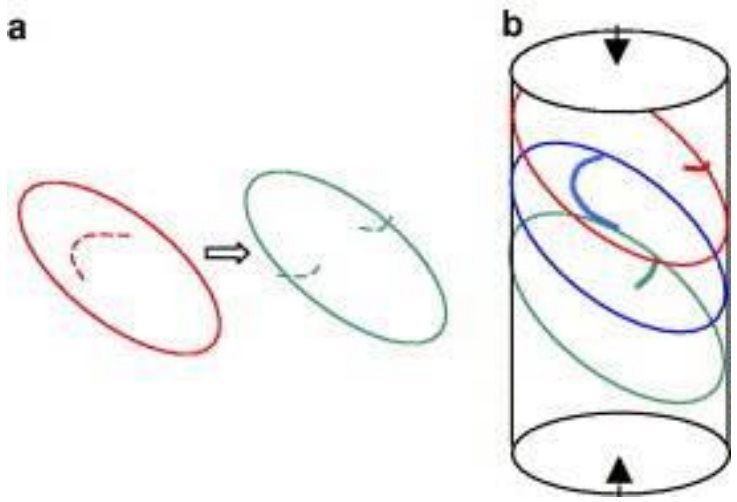

Figure 2-10 (a) A schematic sketch of how double-pinned Frank–Read sources quickly become single-ended sources in samples of finite dimensions. (b) Schematic diagram of single-ended sources in a finite cylindrical sample. The longest arm among the available sources (blue in this case) determines the critical resolved shear stress. Thus the statistics of pins within a sample of finite size determines the yield strength of the sample. [103]

The critical resolved shear stress (CRSS), defined as stress required for the first movement of a dislocation across the sample, is shown as follows:

$$CRSS = \frac{\sigma G b}{\bar{\lambda}_{max}} + \tau_o + 0.5\mathrm{G\ b}\sqrt{\rho_{tot}} \qquad (2\text{-}2)$$

where σ is a geometrical constant, G and b are the shear modulus and Burgers vector separately, τ_o is the friction stress (Peierl's stress) and ρ_{tot} is the total dislocation density. $\bar{\lambda}$ is the mean value of the source length. It is shown that the size effect of samples can be rationalized by stochastics of dislocation source lengths .This equation also matches well with much of the data published and it rationalizes size effect[59,125]. As the model assumes that the stress is not limited by dislocation nucleation but by the glide resistance of a partial dislocation, it is not valid for nanowhiskers. In addition, it can only be applied in microcrystals and predicts only the initial stress for plasticity. This model is supported by

experiments and theory[80,114–116]. Single-ended sources were firstly observed under in situ TEM, which escape the crystal before multiplication[80]. Particularly, the samples are aluminium with both width and thickness smaller than 500nm, and the initial dislocation density is about 2×10^{13} m^{-2}. This conflicts with the notion that single arm source strengthening occurs in micro-sized pillars while dislocation starvation followed by surface nucleation prevails in the sub-micron regime[65]. Furthermore, the dislocation starved state was not found, and a steep increase of dislocation density was even achieved by quickly increasing the strain rates. These findings are contrary to the dislocation starvation model and indicate that a new model needs to be proposed to rationalize the distinctive mechanical performance of metal micropillars and NWs.

(3) Other possible theories

For the dislocation starvation theory, the reason for the size effect is that more stress is required for new dislocation nucleation after reaching the dislocation starved state[60], while for the single arm theory; the size effect is the result of the change in average dislocation source lengths in samples of finite size[103]. Recently, through in situ TEM observation of Cu NWs in the range of 100-200 nm, except for exhaustion hardening, a spiral dislocation source was also found and pre-existing dislocations can be pinned by defects[104]. This is coincident with the source truncation model, so Kiener and M. Minor proposed that both mechanisms should be considered simultaneously. This provides a new view to understand the extant mechanical performance of metal NWs.

At the same time, there are also many other models trying to explain the size effect through 2D/3D discrete dislocation simulation, and the details can be seen in Uchic et al.'s review[126]. Through more and more experimental and modelling exploration, our understanding of the size effect becomes more complete. A prevalent opinion is that the size effect is governed by

different mechanisms in different diameter ranges,[65,127] like single-armed dislocation source appears in micron sized FCC samples and dislocation starvation theory becomes predominant when the diameter is reduced to nanoscale. [65] However, these theories are proposed based on the mechanical test results of NWs above 100 nm with limited structure information, and there is no systematic research on the deformation behaviours of NWs from micrometre to tens of nanometres as far as we know. Also, it seems not very persuasive to explain the size effect with a uniform empirical power law exponent using several sets of theories. To solve these problems, some systematic studies for NWs with a large diameter range, as well as enough structure information to serve as strong evidence to support the assumptions are needed.

2.3 Metal NWs and NWs containing twins.

Current studies on deformation behaviours of metal NWs are constrained by sample preparation sometimes, so in this part, the NWs fabrication methods will be briefly discussed as a beginning. Then the mechanical responses of several kinds of NWs containing TBs are discussed to have an initial understanding of their deformation mechanisms with the existence of TB. Since the metals NWs are used as networks under cycling loading, the failure of these networks is reviewed in the end.

2.3.1 Fabrication of metal NWs

Currently, there are many different methods to fabricate metallic NWs[32,86,128–131]. Among them, the templates assisted electrodeposition and solution-processed routes are the main choices. Using porous templates, the shape and diameter of the metal NWs can be controlled effectively. On the other hand, the NWs made by this method are free-standing in the normal direction of the substrate and can form regular arrays, which expand their application in sensor fabrication[132] and compression tests[133]. In this study, templates assisted

electrodeposition method is adopted to fabricated single crystal Ag NWs. The details can be seen in the experiment section.

The solution-process route, including hydrothermal synthesis, reduction of a precursor solution and catalytic synthesis, is a simple and high-yield method to produce metal NWs.[8] Ag NWs produced by polyol process have been commercialized. This process is briefly described as follows: typically silver precursors, e.g. silver nitrate, are reduced in ethylene glycol solution in the presence of agents such as $MnCl_2$; the presence of a surfactant, such as Polyvinyl Pyrrolidone (PVP), directs the growth and long twinned pentagonal section prismatic wires are formed[32,35]. The mixture is reacted under controlled temperature for some time and the precise chemical conditions (composition of salts, PVP concentration and temperature) control the length and diameter of the NWs. Synthesized Ag NWs are separated by centrifugation and washed before the user.

There are some other ways to synthesize metals NWs. Physical vapour deposition is used to fabricate single crystalline nano-whiskers with high crystal quality, like Cu, Au and Ag[134]. Kim et al. [33] adopted stress-induced growth method to synthesis Al NWs. Using carbon-nanotube filling with precursor metal precursor, metal NWs are synthesised followed by heat treatment.[135] Various NWs with different compositions, shapes and crystal quality are fabricated using these methods, which promote the research on the deformation mechanisms and applications of metal NWs.

2.3.2 Mechanical behaviours of pentatwinned Ag NWs and NWs containing twin structures.

2.3.2.1 The deformation behaviours of Pentatwinned Ag NWs

Wu et al.[136] carried out bending tests on pentatwinned Ag NWs using a lateral force atomic force microscope (AFM). The Ag NWs displayed abrupt brittle failure without plastic

behaviour after super elastic deformation. When the twin boundaries were removed by thermal annealing, a transition to lower strength following plastic deformation was observed, which proved the critical roles of twin boundaries on the brittle failure. Further experimental and simulation studies have confirmed the effect of twinning boundaries in enhancing the mechanical performance and strain hardening behaviour of Ag NWs.[39,90,137–139].

By analysing the cross-section geometry, it seems that dislocations prefer to nucleate from the corners of the free surface.[140] During tensile tests, the dislocation emission and propagation in pentatwinned NWs are constrained by the internal twinning structures, leading to steep necking and subsequent brittle failure.[138] However, the dislocation movement process in pentatwinned NWs has not been reported experimentally. Narayanan et al.[139] found that the dislocation density near the fractured surface is higher than that far from the fractured surface. They also observed the cross-slip of the Shockley partials at the twinning boundaries. These findings are consistent with MD simulations, while they can't prove the role of twin boundaries on dislocation nucleation and movements directly.

Different from the brittle fracture observed in bending, size dependant plasticity was observed in pentatwinned Ag NWs ranging from 40-130nm through in-situ tensile tests in the TEM[13,139]. It showed that dislocation nucleation and propagation take place in discreet localized zones, and these plastic zones increase with smaller diameter NWs.[13] MD simulation revealed that partial dislocations nucleate from the surface area between two twin boundaries, then stacking fault decahedrons (SFDs), the shape of which is supported HRTEM images (Figure 2-11 a-b), will quickly form under the assistance of twinning structures (barriers) and promote subsequent nucleation of SFDs at other locations. The plastic strain is the result of the formation of SDFs. A similar ductile plastic deformation process was also observed in pentatwinned Cu NWs[141].In these reports, the formation of SFD during plastic deformation has not been observed in TEM clearly. Furthermore, pentatwinned Ag NWs with

relatively larger diameters (> 150 nm) shows complex structure at the fractured surface (Figure 2-11c),[142] which is postulated to show that more dislocations in bigger wires can create some nucleation sites inside the wires, rather than from the surface for smaller NWs. All these assumptions seem reasonable, but they are mainly supported by MD simulation works.[13,139] Detailed structure information with high resolution microscopy is necessary to reveal the effect of the TB during deformation. In addition, it was reported that bicrystalline Ag NWs shows brittle to ductile transition at a high strain rate 0.2 /s, owing to grain boundary migration and dislocation interactions[143]. At a low strain rate, defects on the surface of NWs lead to localized plasticity, resulting in brittle-like failure. This reminds us that other factors, e.g., strain rate, may seriously affect the mechanical performance of pentatwinned NWs, which needs to be considered when comparing the behaviours of NWs with different diameters and tests conditions.

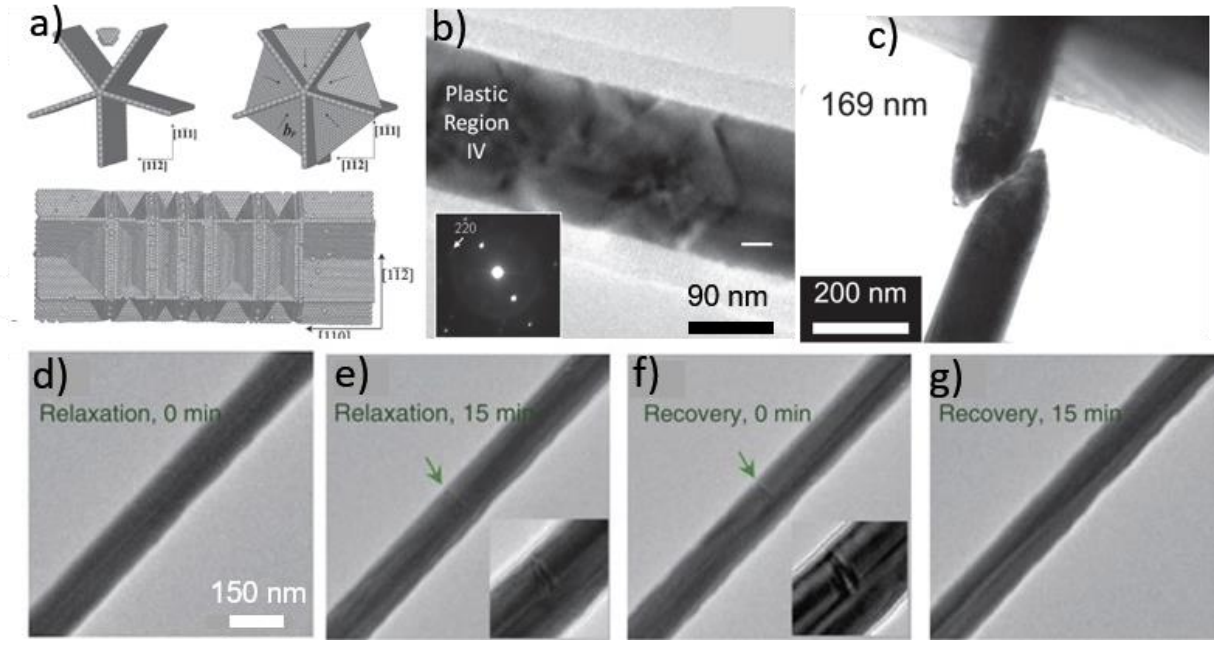

Figure 2-11 TEM images of pentatwinned Ag NWs deformation (a)(b) are the SFD modelled and corresponding TEM observation.[13] (c) is the fractured NWs with a diameter of 169 nm.[142] (d)-(g) is the sequence images of recoverable plastic deformation process of the NWs.[11]

Under tensile tests, the strength of pentatwinned Ag also proved to follow the size effect, and the power law exponent is still the same with other FCC metals, about -0.6.[90,142] Zhu et al.[90] think that this is the statistical nature of surface dislocation sources, as they found that the yield strain is related to side surface area of the NWs. In this assumption, they did not consider the role of TBs that may alter the size effect. Even though the barrier effect of TB for larger wires is still under debate, dislocation arrest after meeting TBs has been observed experimentally for NWs ranging from 30-120 nm in some research, leading to the recoverable plasticity of pentatwinned Ag NWs under tension.[122,11]. For example, Qin et al.[11] found dislocation annihilation during stress relaxation and strain recovery respectively (Figure 2-11 d-g). MD simulation indicates strain recovery is caused by the partial dislocation retraction effect facilitated by TB obstacles and its intrinsic stress field. Moreover, these behaviours are not found in single crystal Ag NWs,[11] while bi-crystalline NWs with a single twin boundary exhibit a similar behaviour in simulation, confirming that the TB can from a barrier to dislocation movement for pentatwinned NWs below 120 nm. Although there is still no research comparing the strength of pentatwinned Ag NWs with single crystal NWs directly, it is reasonably expected that the strength of pentatwinned Ag NWs will be increased due to the barrier effects of TB, which make it questionable that whether the power law exponent of size effect is similar with other FCC metals. The tested mechanical performances of NWs under tensile tests are very sensitive to the defects, making the data scattered in experiment, so more systematic experiments are expected.

Young's modulus, which is often referred as the elastic modulus, reflects the stiffness of materials. The size dependence of Young's modulus in pentatwinned Ag NWs, which is that the value of Young's modulus increases with smaller diameter NWs, has been reported in many publications. [10,90,139] This is the same sense as the size effect in yield strength[90]. Significant increase in the Young's modulus of the smaller NWs is revealed to originate from

the central area of quinquefoliate-like stress-distribution over the 5-fold twin, rather than from the surface tension that is often considered as the main source of such size-effects found in nanostructures[137]. Nevertheless, there are discrepancies in the reports of the size dependence of Young's modulus. Using AFM nanoindention system, Chen et al.[144] discovered that the values of elastic modulus showed no clear size dependence from 65.9 to 141.4 nm. A size dependence of Young's Modulus is also not observed in Filleter et al.'s experinments[13].

2.3.2.2 Deformation of nanowires containing twins.

Metal materials with nano-twinned structures other than penta-twins have also been reported in some research. Reviewing their mechanical responses can help us have a better understanding of the effect of TBs in NW deformation. In this part, the twinning structure is parallel with each other, and the direction of which can be parallel, inclined or normal to the NW growth direction.

The bi-twinned plane parallel to the growth direction in Ag NWs is fabricated by PVD methods.[106] In this research, the partial dislocations nucleate from the surface of the NWs, then two kinds of deformation occur, which are localized dislocation slip and tensile detwinning. In the former cases, MD simulation shows that a stair-rod dislocation across the TB forms after the partial dislocation transits the TB, which facilitate the trailing partial nucleate then sweep through the NWs. In the other case, multiple dislocations nucleate and propagate in two {1 1 1} planes, the interaction of a TB with multiple dislocations can lead to the detwinning of the TB. The different deformation processes may be the results of NWs

volume ratio and cross section shape changing.

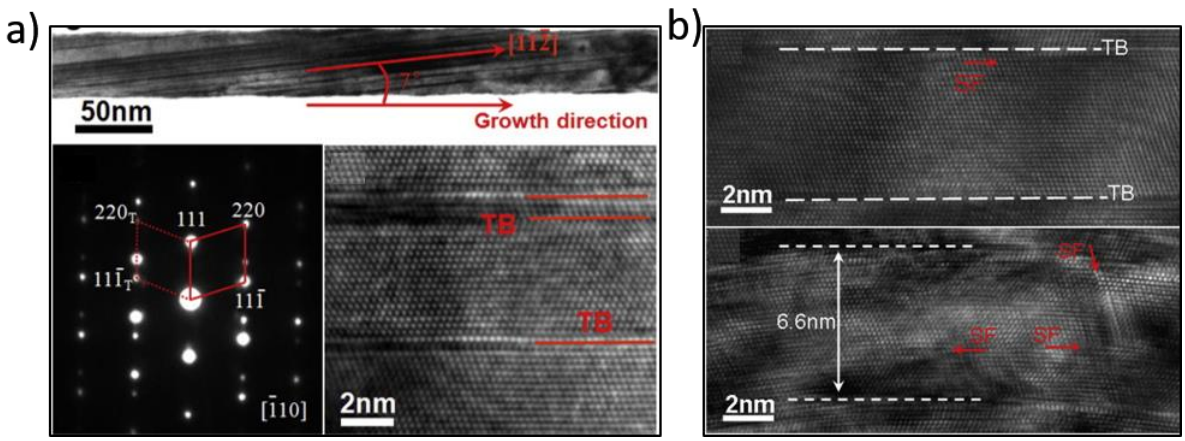

Figure 2-12 TEM images of Nickel NWs and part of deformation process. [145](a) Nickel NWs with inclined TBs (b). Sequence HRTEM images of partial dislocations intersecting the TBs when the twin thickness is about 6.5 nm.

When the TB is inclined to the NW growth directions, there are some interaction points between TB and surface (TB-S). These places are predicted to be the dislocation nucleation sites in simulation work.[146] The Ni NWs with twin planes inclined to the growth direction was bent under TEM to explore the dislocation nucleation mechanism (Figure 2-12a), and the deformation process is in-situ observed at the atomic scale.[145] Nevertheless, this work proved that compared with other surface places, TB-S interactions were not the preferred nucleation sites. With the twinning thickness reducing to 6.5 nm, the type of dislocations changes from perfect to partial dislocations (Figure 2-12b). As the twin thickness increases to 12 nm, the plasticity is controlled by perfect dislocations. Between this range, both partials and perfect dislocations can be observed. This critical length 12 nm is five times smaller than Ag (seen in equation (3)), which is mainly due to the different stacking fault energy and shear modulus of Ni[147] (120-130 $mJ*m^{-2}$,shear modulus 93GPa) than Ag[111,145], (22 $mJ*m^{-2}$, shear modulus 30 GPa). The interaction between TBs and partial dislocations changes from dislocation pile-up then cutting through to parallel movements with TBs with twin thickness decreasing, while it is worthy to note that this parallel movement is only observed in bending

tests, not in the uniaxial test, where the only dislocation passed through TBs is observed under TEM.[47] In tensile tests of NWs with slanted twin-boundaries, de-twinning is observed due to the interaction between dislocations and TBs in NWs.[14] This experiment reveals that the twin thickness increased from 1.2 to 15 nm after deformation (Figure 2-13a-b). A possible explanation is that the detwinning is the result of massive dislocations nucleated from the interaction of TB-S slips along the TB under continuous deformation, which is not captured in experiments but supported by MD simulations.

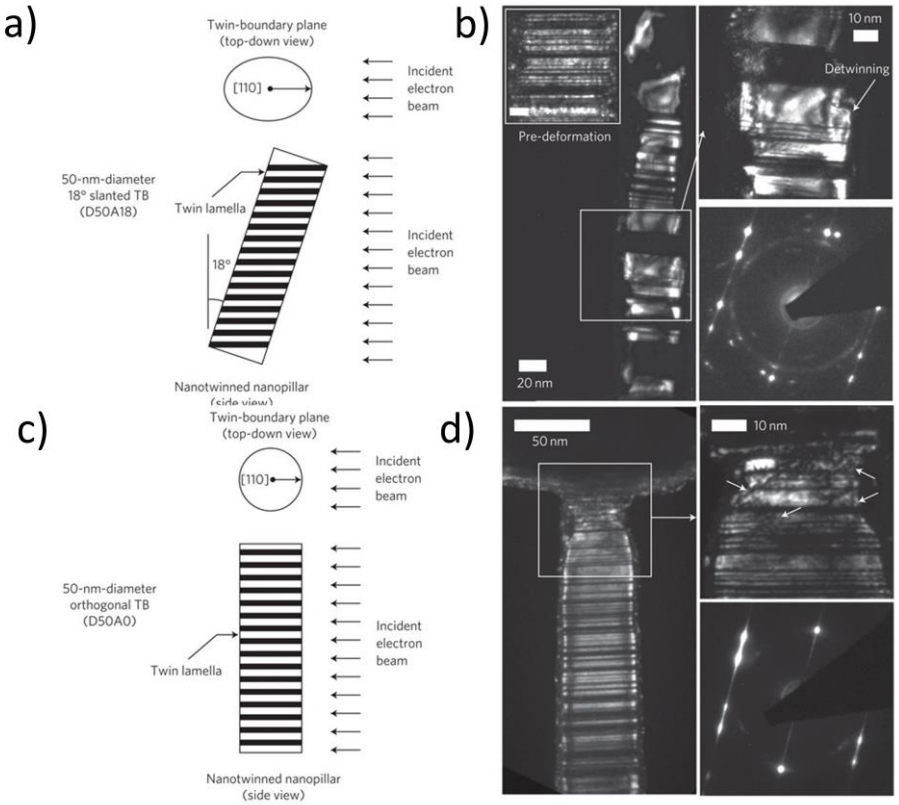

Figure 2-13 Tensile deformation of Cu NWs with TBs.[14] (a) (c)Schematics describing the relative position of incident electron beam and Cu NWs. (b) TEM dark-field images and electron diffraction pattern of deformed NWs with TBs inclined to the growth direction, and typical undeformed samples is presents in the left (d) TEM dark-field images and electron diffraction pattern a deformed NWs with TBs normal to the growth direction. (Scale bar, 10 nm).

Metal NWs with TBs ({1 1 1}) normal to the growth directions can be produced by single-step chemical synthesis[31] and electrochemical electrodeposition with/without templates[14,148] experimentally. The TB thickness can be changed through adjusting some parameters. The

representative structure of nanotwinned NWs can be seen in Figure 2-13d. These NWs/nanopillars are predicted to have high strength, resulting from the formation of Lomer-Cottrell locks on the TBs.[149] The high strength is observed in tensile tests of Cu NWs with TBs normal to the growth direction with the average value of 2.12 GPa, which is 1.5 times higher than the nanopillars with the same diameter.[150] Simulation work indicates that dislocations nucleate from the intersection of TB-S. There should be no resolved shear stress on the TB, so nucleated dislocations glide on the slip planes until meeting the TBs. Several parallel dark contrast lines across the TBs are observed under TEM (Figure 2-13c-d), which is believed to be the result of the interaction between these dislocations and TBs. Similar to the bending behaviour of Ni NWs with TBs,[145] the deformation behaviours are also changed with TB thickness decreasing, which is that the fracture will transfer from ductile mode to brittle mode when the spacing of twin boundaries decreases below the critical value. This might be related to the intrinsic brittleness of twin boundaries.[14]

Above all, these initial studies indicate that the test methods and direction of TBs relative to the NW growth direction have a strong effect on the underlying deformation mechanism. In the bending test of Ni NWs, the preferred nucleation sites are not the interaction of TB-S, while they may be the preferred nucleation sites under uniaxial tensile test, even though this has not been proven experimentally. Under continuous loading, the dislocations will interact with TBs and pass through if there is no resolved stress on the TBs. Under resolved shear stress, dislocations will glide along the TBs followed by detwinning. However, most explanations of dislocation nucleation and gliding are based on atomic simulation. More experiment observations, like in situ TEM, are necessary to reveal the role of twin boundaries and related deformation mechanisms.

2.3.3 Cyclic bending behaviours of Ag NW networks

Metal NWs is normally used in the form of networks to serve as flexible transparent electrodes, so research on the mechanical responses of NW networks under cyclic loading is important for the device reliability. The fatigue resistance of individual crystal NWs is believed to be better than bulk materials due to the reduced dislocation accumulation inside the wires during defromation.[74] High fatigue resistance has been observed in ZnO NWs.[151] Furthermore, the strain may be accommodated due to the mechanistic movement of complete nanowires leading to network deformation rather than the stretching of individual Ag NWs,[152] so the fatigue resistance performances of metal networks should be very good. This is also confirmed through comparing the electrical resistance of Ag NW networks with a 100 nm thick Ag film under cyclic deformation. After 500 000 fatigue cycles in a bending rig at 1% strain, the resistance of the Ag NW network increased 1.5 %, while the resistance of the Ag film increased 78%.[152]

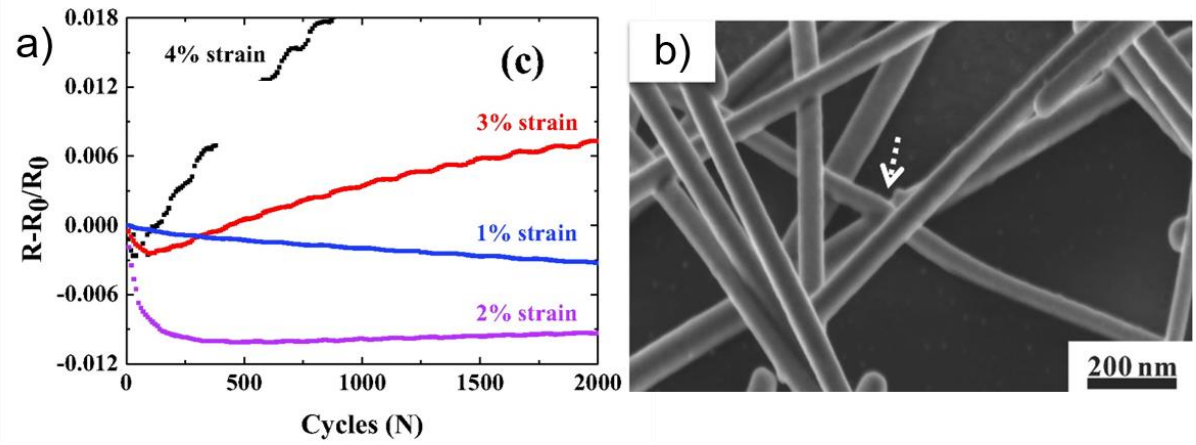

Figure 2-14 Properties of Ag NWs networks under cyclic loading. [152] (a) The resistance changes as a function of fatigue cycles (b) SEM images of the NWs networks after imposing 500 000 cycles with strain 1%.

On the other hand, the fact that the Ag NW network's resistance increases suggests that some NWs failed during fatigue.[83,153,154] Current papers report on the fatigue behaviour of Ag NW networks after cyclic bending of the networks on flexible substrates and do not focus on the

behaviour of individual NWs within the network. The failure of Ag NWs networks is normally characterized by two experimental observations: resistance changes and microstructure characterization. An initial decrease in network resistance at the beginning of the fatigue test is widely observed (Figure 2-14a). This is interpreted as the repeated bending allowing the network to relax after deformation and possibly enhance the contact and adhesion between NWs in the network.[152] Some welded junctions that form after fatigue can be observed in SEM images (Figure 2-14b). In addition, it has been proposed that the initial density of the Ag NW network will affect the reliability the NW networks, but conflicting conclusions have been reported.[83,154] One research found that the resistance of the low density Ag NW networks increased to 2.54 times after fatigue while the high density of Ag NW networks, the resistance increased to 1.38 times.[83] This enhanced reliability in high density Ag NWs networks was explained through modelling electrical conductivity of the Ag NW network using a percolation approach. However another report found that an increase in NW density results in a degraded electrical performance of the network after fatigue testing.[154] However, It should be noted that the first of these conflicting reports applied tensile strains on the NW networks though cyclic bending, while the later ones applied compressive strains. Hwang et al.[24] compared the compression and tension bending behaviour of Ag NWs, where buckling within the length of NWs is observed under SEM and TEM (Figure 2-15a) for compressive strain and under tensile strain junction failure occurs as a results of stress concentration. These different deformation behaviours still can't explain the contradicting conclusions on the relationships between NW density and network reliability. Also, given the small numbers of images published and a lack of quantitative analysis, it is still not certain whether the NW networks fail at the junctions between NWs or through individual NW fractures. Systematic fatigue tests combined with TEM observation are thought to be an

important method to improve our understanding of the deformation processes during the fatigue of metal NW networks.

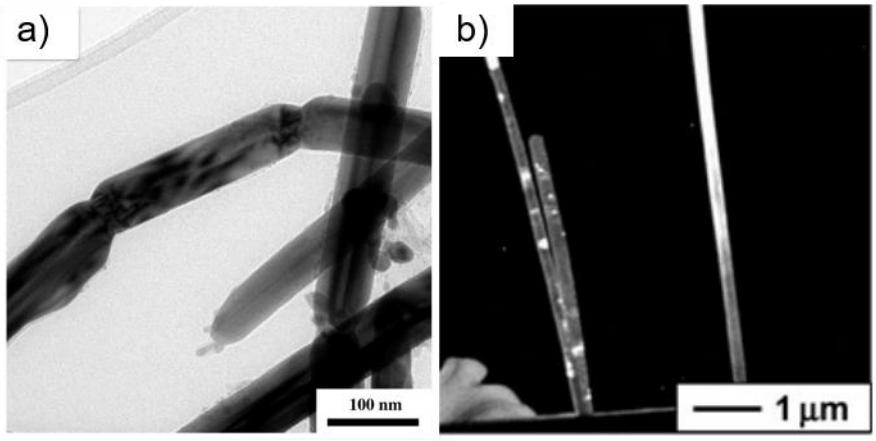

Figure 2-15 TEM images of NWs after cyclic loading. (a) Pentatwinned Ag NWs deformed by compressive bending.[24] (b) Dark filed images of pristine Cu-Si NWs and deformed ones after cyclic tensile tests. [155]

As to the fatigue behaviours of individual metal NWs, there are very limited reports in the literature due to the challenging experimental conditions. One study indicates that individual NWs fail under low-cycle fatigue when testing in the elastic deformation zone.[156] By comparing the microstructure of pristine Cu-Si NWs with other deformed NWs under cyclic tension-tension loading, another study proposed that their microstructure changes from polycrystalline to almost single crystal states, shown in Figure 2-15b.[155] Although above two studies did not explore the underline mechanisms of observed results in detail, these initial works inspire us to further explore the fatigue behaviours of metal NWs. It is promising and necessary to reveal the microstructure changes in nano-scaled samples under cyclic loading using advanced structure characterization techniques.

2.4 Summary

In this chapter, current research related to the deformation of FCC metals NWs has been reviewed. The fundamentals of crystal defects and pentatwinned Ag NWs were discussed

firstly. Line defects and planar defects are mainly introduced for researching the mechanical responses of Ag NWs. The structure of grain boundary defects can be analysed using CSL model. As one of the main defects in pentatwinned Ag NWs, the properties and impacts of Σ3 boundary (twin boundary) on the mechanical properties of materials were discussed. The dislocation movements when interacting with TBs in bulk metals are affected by many factors, such as loading directions relative to TBs and twin thickness. The fatigue performances of materials with nanotwins were discussed, where the fatigue resistance has been found to be improved, and TB exhibit high stability under cyclic loading.

Afterwards, the size effect, which is that the strength of materials increases with the diameter decreasing, was reviewed. Since most work explored the size effect by compression tests, the mechanical behaviours of these tested pillars are introduced in the beginning. The difficulties in conducting tensile tests of NWs limit the related studies, so the tensile test methods are reviewed next. Then we had a discussion on the dislocation behaviours in NWs under tensile tests. Different mechanisms explaining the size effect of materials were introduced in the end. The debates among different mechanisms still exist, so systematic research on the mechanical responses of metal NWs combined with detailed microstructure information are in highly demand.

In the final part, the applications of metal NWs were introduced, and fabricating flexible, transparent electrode is their main application. The methods fabricate metal NWs are various. The solution-processed routes and electrodeposition are the popular ones. Studies on the mechanical behaviours of the pentatwinned Ag NW were reviewed then. To have a complete understanding of the impacts of TBs in NWs, the mechanical properties of other metals NWs with TBs inside were also discussed. As NWs applied in flexible electronics are under fatigue loading conditions from a long-term view, the cyclic deformation behaviours of Ag NWs in networks were summarised in the end. In the above research, there is limited microstructure

information of the deformed Ag NWs. Mechanical tests followed by advanced structure characterization will be useful to explore the deformation mechanisms.

3 Experimental methods

3.1 Single crystal Ag NWs fabrication through electrodeposition

To explore the effect of five-fold twin boundaries on the mechanical responses of Ag NWs, single crystal Ag NWs are fabricated by electrodeposition for comparison in this work. The nano-porous templates used for electrodeposition is thin film aluminium oxide, which can be synthesized by a two-step anodization process.

3.1.1 Porous aluminium oxide template fabrication by a two-step anodization process

A two-step anodization process was used to prepare anodized aluminium oxide (AAO) templates for the electrodeposition of metal nanowires in the diameter range 30 – 100 nm [133,157] . The process flow diagram is shown schematically in Figure 3-1. Firstly, pure Al sheets are cleaned and electropolished in a solution of perchloric acid and ethanol (volume ratio 1:19) to get a smooth surface. Following this the sheets are anodized in 0.3 M oxalic acid solution at 40 V for 12 hours (10 ^{o}C). To improve the pore regularity, two-step anodization is conducted. The AAO film formed in the first anodization is removed by 1 M phosphoric acid at 60 ^{o}C for about 1 hour. The second anodization step is carried out under the same conditions (constant voltage

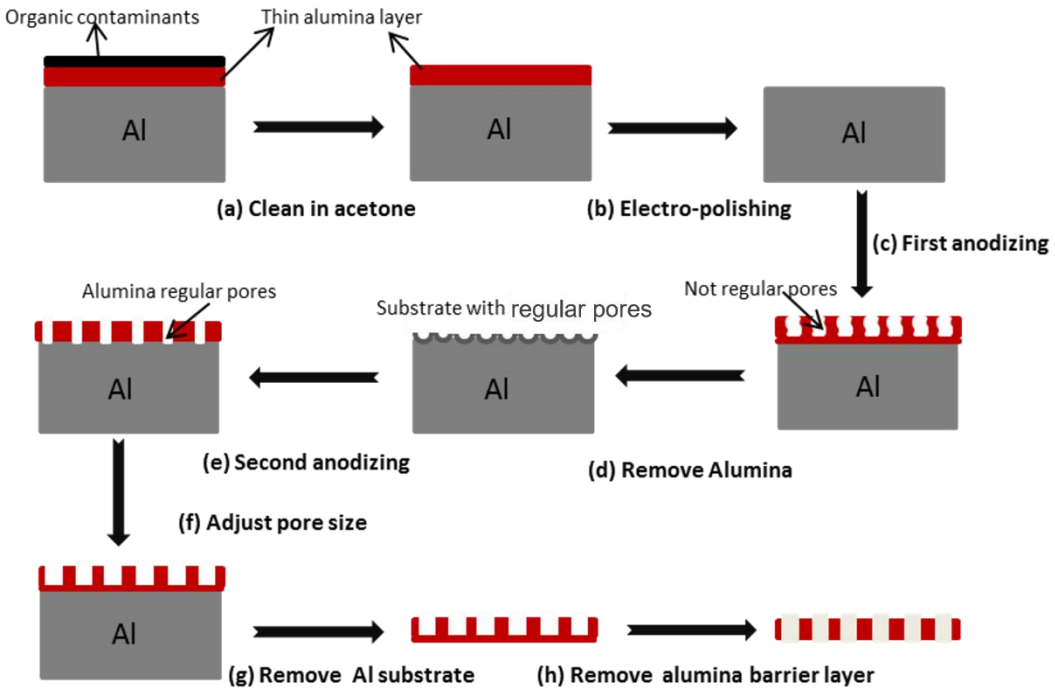

Figure 3-1. Schematic of the two-step anodizing procedure.

of 40 V in a 0.3 M oxalic acid solution at 10 ^{o}C). The thickness of the final AAO film is controlled through varying the second anodization time (about 220 nm/min).

The process steps outlined above produce an AAO film with regularly spaced nanopores of a mean diameter of about 30 nm that extend through the thickness of the film. Nanopores templates with different controlled diameters in the range of 40 – 100 nm were obtained through chemical etching in phosphoric acid (0.1 M) at 30 ^{o}C. Figure 3-2 shows examples of the nanoporous AAO films with hole diameterd of 40 nm, 80 nm and 100 nm. The side view of the fabricated AAO film is shown in Figure 3-2 (d), which is straight and uniform.

To remove the AAO film from the parent Al sheet the film is protected by coating with poly methylmethacrylate (PMMA) applied from solution (0.1 g/mL in acetone). Then the aluminium substrate is removed by etching in 0.1 M CuCl solution. The exposed barrier layer is etched by 0.1 M phosphoric acid for about 60 min at 30 ^{o}C to remove the non-conductive

barrier layer that forms at the Al/AAO film interface during film growth. A thin gold film is applied by sputter coating to form the electrode for electrodeposition. Finally, the PMMA protection layer is removed by dissolution in acetone at room temperature to produce the finished AAO templates for fabrication of Ag NWs.

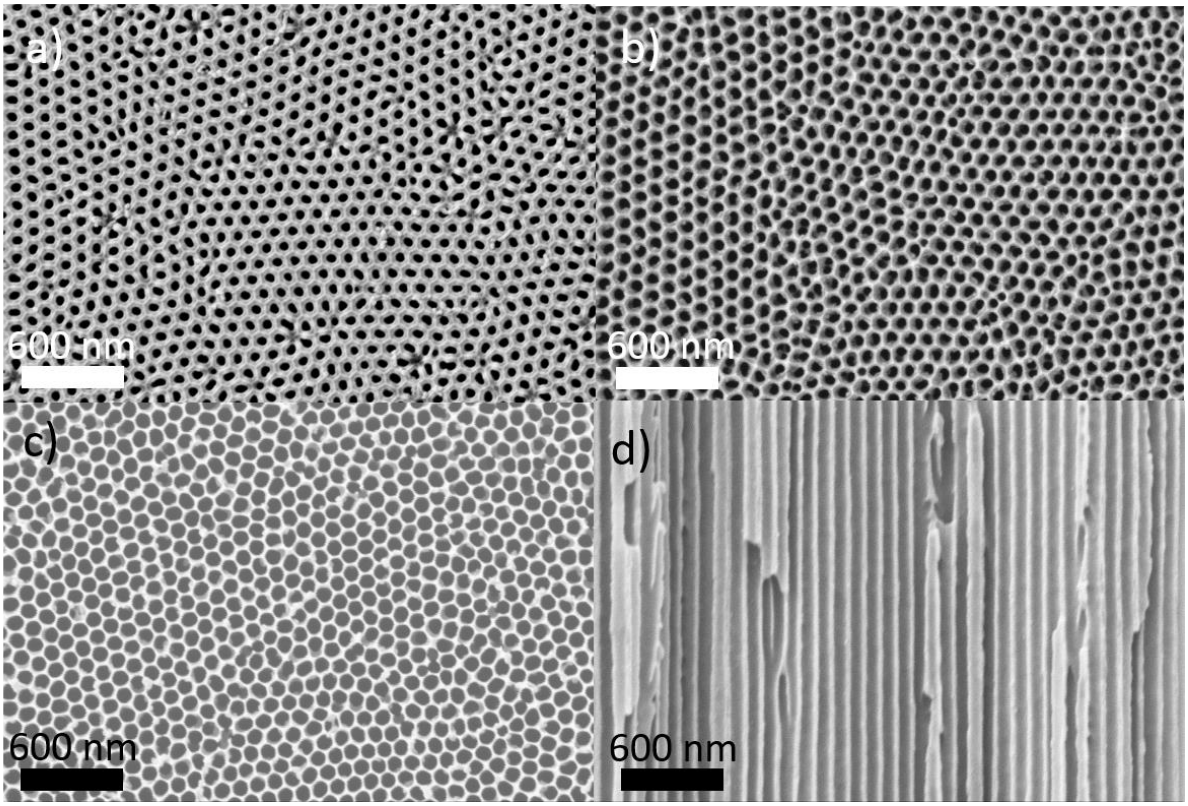

Figure 3-2 Porous AAO template fabricated by two-step anodization with different diameters of (a) 40nm (b) 80 nm(c) 100 nm. (d) Side view of the AAO template.

3.1.2 Electrodeposition of Single crystal Ag NWs

Ag NWs are fabricated by electrodeposition using AAO templates in a beaker filled with 0.05 M Ag_2SO_4 +2.3 M KSCN solutions under a constant voltage.[131] A three-electrode cell with a platinum mesh counter electrode was adopted and an Ag/AgCl electrode was used as a reference, so all the potentials in this work were referred to this electrode. The AAO templates produced before were fixed on Cu sheets and acted as cathode and other areas of the cathode to be immersed in solutions except for the AAO templates were coated by lacquer (lacomit 'stopping-off' lacquer, MarcDermid, Connecticut, United States)). Then Ag

NWs was electrodeposited at a constant voltage and temperature. By adjusting some parameters, e.g., voltage and temperature, the density of dislocations can be controlled.

During the electrodeposition process, two mechanisms occur simultaneously: (i) Growth of existing nuclei and (ii) nucleation and formation of new grains. For the fabrication of single crystal NWs, the first process should dominate.[131] As higher temperatures can reduce the cathode polarization, facilitate ion transportation to electrode and increase surface diffusion, the growth of existing nuclei is favoured under these conditions according to the report.[158] The temperature of the solution is increased to 20 °C, 40 °C, and 60 °C separately. Corresponding TEM image and SADP can be seen in Figure 3-3. It shows that Ag NWs contain fewer dislocations with increasing temperature. When the temperature is 60 °C, the diffraction pattern is much more regular, which indicates that its structure is single crystal. Figure 3-3c shows that the zone axis of the tested Ag NW is [$\bar{1}$10], indicating that the grow direction may the same with the preferred growth direction [110].[131]

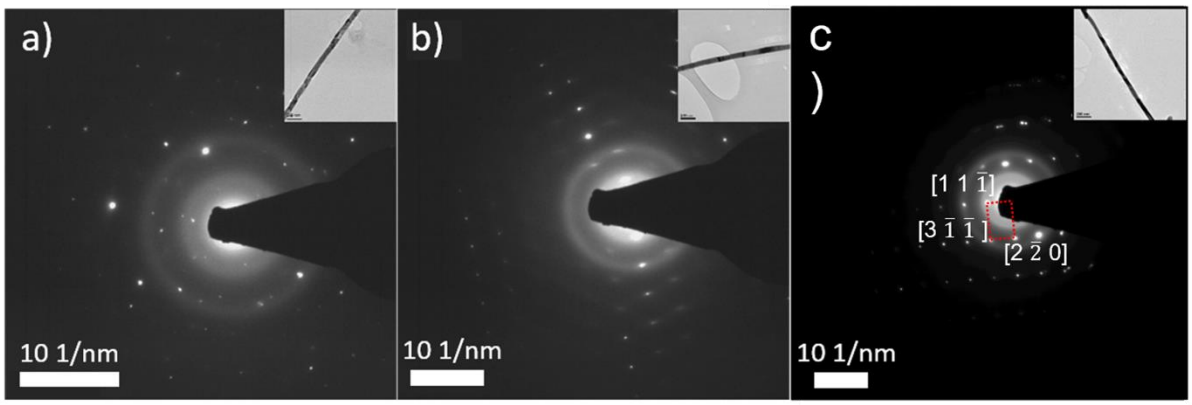

Figure 3-3. TEM diffraction patterns of Ag NWs fabricated by electrodeposition (-50 mV) under different temperatures of (a) 20 °C (b) 40 °C (c) 60 °C.

Commercially available polycarbonate (PC) track-etched templates with a diameter from 100 nm to 800 nm are also used for electrodeposition, as it is difficult to fabricate NWs with diameters larger than 150 nm using AAO templates. Before the deposition process, one side

of PC templates was coated by sputtered Au as a conductive layer. Single crystal Ag NWs were produced under the same condition as mentioned before (-50 mV, 60 ^{o}C). The diameter of fabricated Ag NWs is uniform, as shown in Figure 3-4a. The diffraction patterns in Figure 3-4b indicate that the NW is also single crystal one.

For the electrodeposition of Ag, a 2-dimensional nucleation process followed by crystal growth has been previously proposed.[159] It is well known that for FCC crystals, the close-packed surface is {1 1 1}, which has the lowest energy, followed by the {1 0 0} and {1 1 0} faces. Therefore, the {1 1 1} is the preferred exposed crystal plane during crystal growth process if only consider the thermodynamical growth process. However, the preferred crystal growth direction is not only decided by the equilibrium properties of crystals, but it is also influenced by factors controlling electrodeposition kinetics, such as electrolyte composition, potentials and temperature. Hence, it has been proposed in prior research that the overpotential could induce a thermodynamic to kinetic transition, making {1 1 0} a favoured growth face under overpotential conditions, and that the adsorption of H^{+} ions on the cathode may stabilize the {1 1 0} plane.[160] This theory only considered the surface energy of the growth front in electrodeposition. It was further refined by Muarer et al.,[161] who calculated the energetics of electrodeposited nanowires by considering both the side surfaces and the growth surface. They found that the preferred growth direction of NWs is related to their aspect ratio (length to diameter). Above rather small aspect ratios (about 1), <1 1 0> rather than <1 1 1> becomes the energetically preferred orientation. This condition is easily achievable for NWs with a very small diameter (at the nanoscale) in the initial stage of electrodeposition, so it can also be used to explain the observed preferred growth direction <1 1 0>. However, a complete model that can explain the preferred growth direction of Ag NWs is still under exploration.

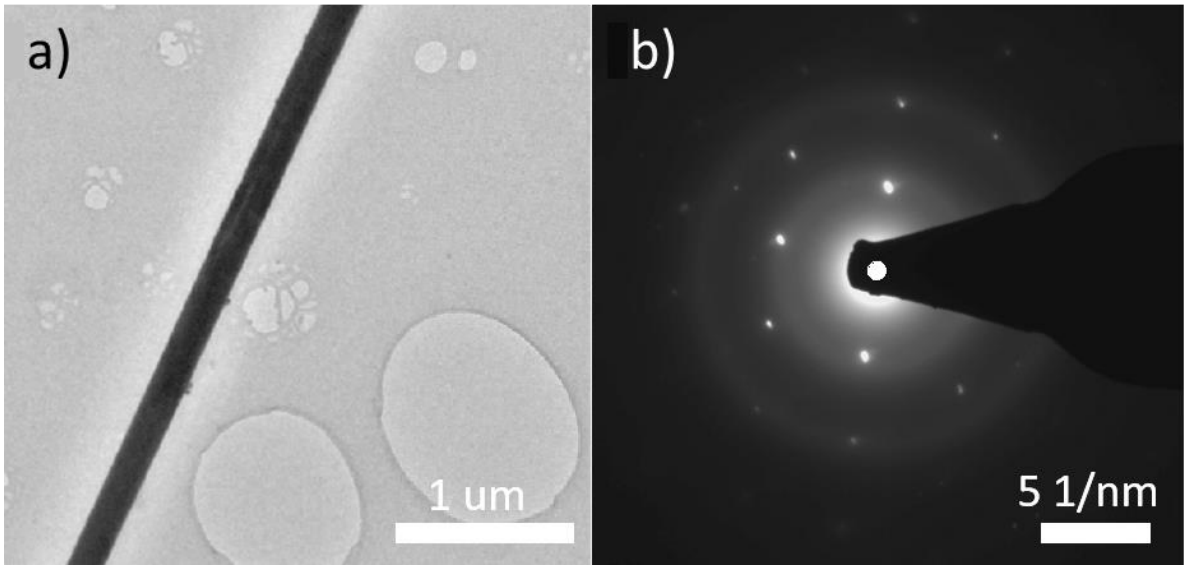

Figure 3-4 Ag NWs with a diameter of about 150nm grown in polycarbonate templates. (a) is the high magnification image of fabricated Ag NWs and (b) shows that corresponding electron diffraction patterns.

3.2 Scanning precession electron tomography and data analysation

3.2.1 High resolution and sensitivity crystal defects characterization in nanoscale

Understanding the deformation mechanism of nano-structured metals requires detailed microstructure characterization. The key techniques developed for microstructure analysis are EBSD and transmission electron diffraction in TEM.[15–19] EBSD in is acquired inside SEM though collecting electrons diffracted by surface materials using charge couple device (CCD) camera. After being scattered by the atomic planes, the electrons satisfying the Bragg condition will form a group of paired large-angle cones, which are typically the Kikuchi bands on the detector screen. To get the crystal structure information, the Hough transform is adopted to locate the position of collected Kikuchi pattern, then comparing this result with data base of crystal structure. EBSD is widely applied in the determination of crystal orientations that are important to many properties of polycrystals, like mechanical behaviours

and electrochemical behaviours.[162,163] For examples, through combining EBSD with microelectrochemical techniques, the differences between the (0 0 0 1) and the (h k i 0) planes were found to be the main factor that determined the electrochemical properties of Ti polycrystals.[163] Besides these, EBSD is also explored in many other aspects of materials characterization, like strain measurement, 3D microscopy et al.[164–166] The changes in the local strain field will lead to the shift of EBSD patterns, so the strain in one position can be determined by comparison with reference patterns from the crystal in a known state or from simulated patterns. The small shift is determined from cross-correlation analysis, and resulted strain sensitivity reached $\pm 2*10^{-4}$.[165] The details of this approach can be found in other work.[165,167] Using EBSD, the strain in $Si_{1-x}Ge_x$ epilayers grown on Si substrates is measured in early stage,[165] and quantitative strain measurement is also reported in plastic deformation process research of structure material, like steel.[168,169] On the other hand, if locating the patterns in Hough space, the precision is limited in the order of 0.1 °.[19] With the development of CCD camera resolution and data processing theory, high-angular resolution EBSD (HR-EBSD) is proposed to measure the shift between two similar features in two EBSD precisely (±0.05 pixels) using cross-correlation method, corresponds to lattice rotation accuracy of 0.01 °.[17] The crystal misorientation between adjacent points is normally used to estimate the geometrically necessary dislocation (GND), like in equation (3-1) [170] :

$$\rho_{gnd} = \frac{\omega}{b} \qquad (3-1)$$

Where ρ_{gnd} is the GND density, ω is the curvature to accommodate and b is the Burgers vector. The improvement in measuring misorientation and angles accurately contributes to estimating the GND density. For example, Wallis et al.[171] using HR-EBSD to estimate the internal GND density and distribution, facilitating our understanding on the creep behaviours of geological minerals olivine.

Despite these advances of EBSD in determining crystal orientation, there is a complementary technique that routinely offers higher spatial resolution and greater potential sensitivity to small structural changes, which is the TEM based diffraction patterns analysis. For nanostructured materials with complex structures, like pentatwinned NWs, EBSD also can't characterize the inner crystal structure. Therefore, TEM based diffraction pattern analysis, like convergent beam electron diffraction (CBED) and parallel beam electron diffraction, has attracted much interest, especially for studying the structure of nanomaterials.[18] CBED uses a convergent beam to form diffraction patterns with convergence semi-angle ranging from 50 to 20 mrad, resulting in large disks in diffraction patterns. The patterns contain zero-order Laue zone (ZOLZ) intensity patterns (similar with the spots in SADP) and the higher order Laue zone (HOLZ) Kikuchi line pairs. Away from the low index zone axis, there are high order Laue Zone (HOLZ) lines in the disk, the position which is sensitive to the changes in lattice parameters and can be reproduced by semi-kinematical calculations to obtain the lattice parameters information.[172 ,173]. The other choice is adopting a parallel electron beam to produce diffraction pattern, including selected area diffraction (SAD) and nano-beam electron diffraction (quasi-parallel illumination). Limited by the size of SAD aperture, the smallest materials area stimulating electron diffraction patterns is ~0.5 um, which is still larger than most crystal defects and crystal grains in nano-metals. Therefore, in our experiments, we adopted a nanobeam electron diffraction technique to characterize the pentatwinned Ag NWs.

The nanobeam diffraction technique adopts quasi-parallel beam with convergence semi-angle below 1 mrad, and crystal structure is determined from the spots that satisfy Bragg reflection positions and intensities. Bragg conditions is listed below:

$$2\mathrm{d}\sin\theta = n\lambda \qquad (3-2)$$

Where d is the lattice interplanar distance, θ is the glancing angle, λ is the wavelength, and n is a positive integer. A small convergent angle ensures that the diffraction spots or discs are sharp, thus they are less affected by non-uniformity intensity. In practice, interpreting these diffraction patterns is generally done in a simple kinematic framework, which does not consider the interaction between the primary and diffracted waves (dynamic scattering). With sample thickness increasing, the dynamical effects, which results in the diffracted beams being re-diffracted by crystal further along the beam trajectory, is no longer negligible, leading to potential misinterpretation of the diffracted intensities.[15] To solve this problem, the precession system is introduced,[174] as shown in Figure 3-5a, where the incident electron beam is rocked in the hollow cone at a fixed angle along the optic axis above the sample, making the Ewald sphere rock in the reciprocal space, then the diffraction beam spots are integrated via a de-rocking below the sample. This process is equivalent to rocking the sample under a fixed electron beam, and every diffraction spot is integrated over a range of angles that include Bragg condition. Besides reducing dynamical scattering on reflection intensities by avoiding multi-beam excitation, using this nanobeam precession-assisted electron diffraction (N-PED) technique, more reflections can be excited through rocking (Figure 3-5b-d) the Ewald sphere thus facilitating subsequent analysis.[15] By scanning the electron beam, the crystal orientation in a relatively large area can be characterized with a high spatial resolution (1 nm or below) and an angular resolution of the order of 0.5 degrees. The acquired data is a 4D dataset composed of a 2D array of beam positions as well as a group of corresponding 2D PED patterns.

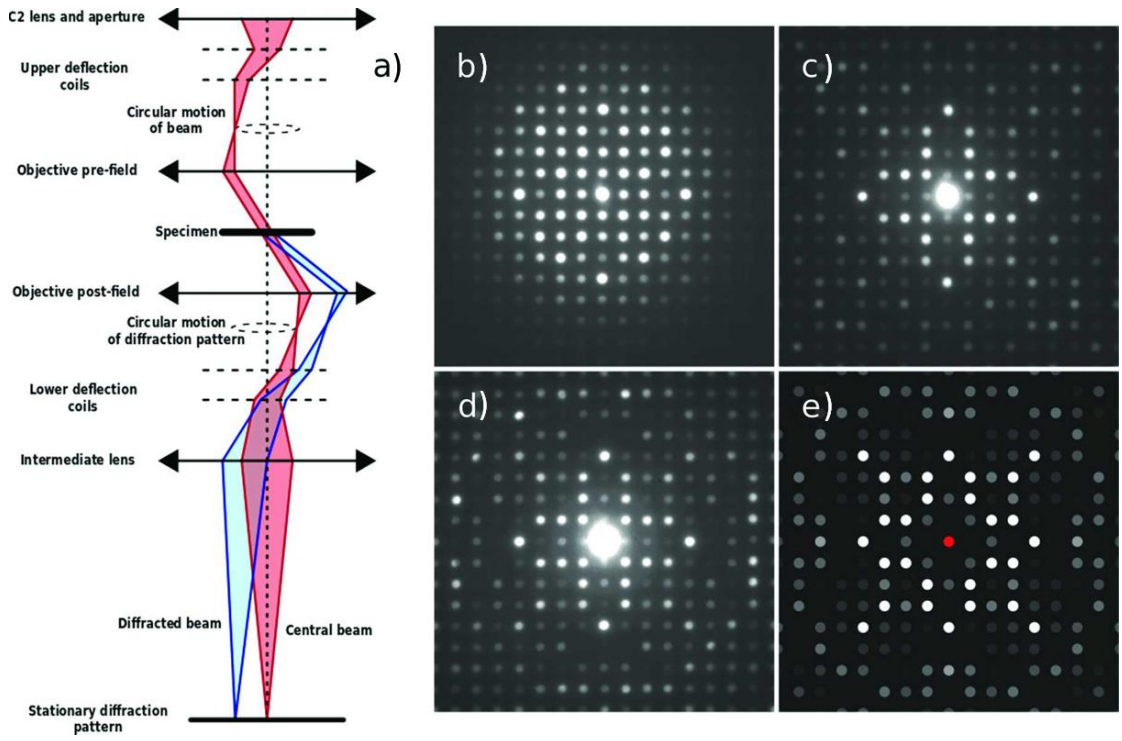

Figure 3-5 (a) The schematic of PED system. (b)-(d) shows how precession altered the resulted diffraction patterns. (b) Diffraction patterns from [001] zone axis of Er2Ge2O7 without precession, (c) with precession angle of 20 mrad and (d) 47 mrad. (e) Simulated patterns based on kinematic diffraction theory. (reprint with permission from reference [15])

Currently, two key applications of N-PED technique are crystal orientation/phase mapping and strain mapping.[175–177] Through comparing PED patterns with pre-calculated templates, crystal orientation of nano-sized ZnO grains with a mean size of 8 nm is confirmed, facilitating the understanding of the ZnO NW nucleation mechanism in chemically deposited ZnO films.[177] The high spatial resolution of this technique compared with EBSD make it widely applied to characterized other nanophase materials in many fields, such as Al-Cu-Mg alloys applied as structure materials,[178] SiC layers used in nuclear industry[179] and semiconductor materials used in electronics[180]. Also, the ability to study crystal structure at high resolution makes it possible to test the stoichiometry difference in some materials using N-PED. In research on Li insertion in $FePO_4$ and extraction of $LiFePO_4$ mechanisms in battery, N-PED is proved to be a powerful technique to distinguish $FePO_4$ and $LiFePO_4$ phases in nanoscale, despite the minor lattice parameter (<5%) difference between two

phases.[176] On the other hand, N-PED for strain mapping of semiconductor materials has also aroused much interest recently. Cooper et .al[175] use this technique to test the strain in 10-nm-thick SiGe layers grown in Si by epitaxy, which is determined from measuring the displacement of seconds order spots in diffraction pattern. Compares with other strain measurements methods, like dark field electron holography (DEFH) and High-angle annular dark-field STEM (HAADF STEM), PED shows best precision in strain mapping with a resolution about 0.02% in their experiments, higher than the results from nano-beam electron diffraction without precession.

Besides analysing the diffraction pattern directly, the virtual bright/dark field images (VBF/VDF), which are constructed through calculating the mean density for a virtual aperture at each beam position, are also powerful tools to analyse the physical extent of individual subcrystals.[18,181] This is similar to the traditional operation that inserting an objective aperture into the back focal plane, while the size, shape and number of the virtual aperture can be arbitrary through adjusting the software, thus increasing the flexibility on data analysis and saving time on equipment operation. An example of the application of VDF images is analysing the dislocation Burger vector (b) using the invisibility criterion $g \cdot b = 0$,[182] where g is the diffraction vector and the visibility can be judge through comparing the VDF images for different g vectors. It is worthy to note that the value of $g \cdot b$ cannot be exactly zero in most cases, so the invisibility method often relies on finding the diffraction vectors that produce weak contrast instead of invisibility. The dislocation state in deformed ferrite was analysed by comparing the VDF images of the same area,[183] which did not perform a complete Burgers vector characterization but do shown some initial valuable information about the defects inside materials. As the virtual aperture is computer generated, the shape of it can be arbitrary and is not limited to disk type holes. To study the spatial distribution of amorphous/nanocrystalline phases in materials, a ring type virtual aperture is

adopted to adapt the rings-like diffraction pattern produced by these phases.[183] Apart from these, the signal filtering capability of this ring-like aperture is also used to replicate the annular fark-field experiments, which are widely conducted to increase the atomic number (Z) contrast in the image.[18,184]

In the above applications, there is normally only one microstructure along the electron beam for the samples milled by FIB, so the diffraction patterns can be indexed through template matching without further processing. However, in some cases, the samples, like pentatwinned Ag NWs, may contain multiple microstructures along the electron beam path, so signal unmixing before templates match becomes necessary.

3.2.2 PED Data Unmixing

The direct way to unmix the overlapped signals is to separate the data layer-by-layer, which is achieved by subscribing the signature of the dominant crystal before reindexing the diffraction pattern using the software.[185] After several such subtraction-indexing cycles, the overlapped signals are separated to different groups that describing the crystal structure of subcrystals along the incident electron beam separately. This method is proved to be efficient to characterize the thin film that composed of a NiSi film stacked on a monocrystalline Si layer through subtracting the footprint of Si. Also, the overlapped grains in tungsten samples were also recognised, as after applying the data unmixing bigger grain appeared with the number of grain increasing.[185] The main drawback of this technique is also obvious, which is that the diffraction patterns shared by two/multiple subcrystals can only be allocated to one subcrystal and be removed in the beginning, resulting in decreasing indexing reliability with subtraction-indexing cycles going. Therefore, the results are not reliable anymore when unmixing the diffraction patterns from a relatively large number of subcrystals, and it is also difficult to recognise the phases of overlapping grains with close lattice parameters.

Since the number of measurements (diffraction patterns) recorded in a typical SPED experiment is much more than the number of basic microstructure elements it contains, the resulting redundancy provides a space for unsupervised machine learning to find patterns with minimal prior constraints in the dataset.[21] Typically SPED is used to analyse materials with some element of unknown crystal structure, be that unknown phases or orientations (or both). This lends itself ideally to blind source separation (BSS), which aims to identify source signals from the (mixed) measurements with little or no information on the source signals or the mixing process. This including some well-known approaches, such as principle component analysis (PCA), singular-value decomposition (SVD), independent component analysis (ICA) and non-negative matrix factorization (NMF).[21,186]

The electron diffraction patterns are formed on a camera or similar detector in TEM and so can only have zero or positive intensity.[187] Many of above algorithms, particularly PCA and ICA, can produce some negative values during matrix decomposition, thus making it difficult for direct physical interpretation of PED signals, even though the signals can still be distinguished mathematically. For NMF, the output matrices are the factor matrix (W) and the loading matrix (H) (Figure 3-6 a), both of which are constrained to be non-negative, resulting in simpler matrix inspection. In addition, it has been proved experimentally that compared with SVD and ICA, only the PED data unmixed by NMF yields patterns that better associated with the twinning structure of GaAs NWs (Figure 3-6 b-c).[21]

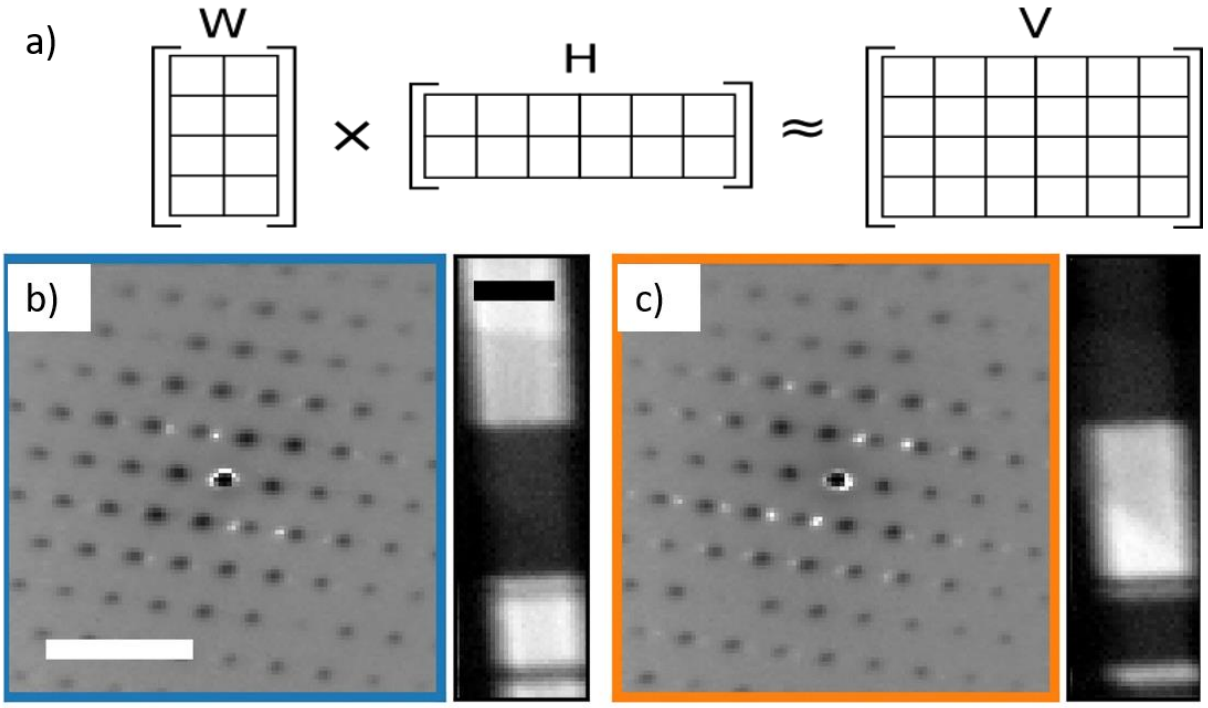

Figure 3-6 (a) illustration of rough NMF process, where non-negative matrix V can be represented by two smaller none-negative matrix W and H. (b) and (c) are the decomposed PED results from twinned GaAs NWs after removing the background, and two diffraction patterns are corresponding to the two twinned crystal orientation.[21]

In this study, the scanning precession electron diffraction data were analysed using machine learning approaches implemented in the 'hyperspy' multidimensional data analysis package.[188] This is a set of Python libraries that allow multidimensional data to be opened and retains the correct data structure. In this case the data is a 2-dimensional array of positions in the scan (the navigation axes), with each position linked to a 2-dimensional image of the diffraction pattern (the signal axes) resulting in a 4-dimensional data structure (Figure 3-7a). To speed up the analysis, a sub-set of the scan area was selected that included the nanowire and a small region of the vacuum surrounding it.

The decomposition was performed by initially transposing the data structure, so that the diffraction pattern dimensions became the navigation axes and the scan dimensions the signal. After this the entire structure was re-cast as double precision floating-point values and the

hyperspy implementation of non-negative matrix factorisation (NMF) was used to determine the factors of the data.

The number of factors needs to be defined by the user in advance. In some research, this value can be obtained under the guidance of the scree plot produced by SVD.[21,189] As the range of components number can be deduced in some samples, a trial-and-error method is normally used to avoid additional data processing to analyse the crystal structure assisted by crystal shape and location information in virtual dark field (VDF) images. For example, for the data collected from pentawinned Ag nanowires, the number of components is assumed to be equal to or above 6, which considered the existence of five subcrystals, the vacuum and some noise.

After the number of essential components has been assumed, the decomposition starts and a detailed mathematical process follows, as seen in previous reports.[190] In brief, the decomposition for NMF is performed through updating the components W and loading H following some rules, thus increasing the likelihood of generating matrix V from the estimated W and H with minimum mean square error (MSE) comparing with original experiment data.[186]

The components maps produced here are similar to DF images here and the loading maps for the decomposition showed those diffraction vectors that scattered intensity to the region indicated by each factor, as shown in Figure 3-7b. Hence, these could be analysed to determine the orientation of the cubic closed packing (CCP) silver crystal structure in that region of the scan, by comparison with a library of pre-prepared diffraction patterns. This process was done using the automated crystal orientation mapping (ACOM) software provided as part of the Nanomegas ASTAR package.

It should be noted that although there are many advantages of using NMF for data unmixing, this method may still produce some misleading results, especially when analysing the diffraction signals from heavily overlapping regions where there may not be a diffraction pattern arising from a single structure (i.e. a pure end-member pattern)[21] or unmixing signals from the crystals that are highly coherent since the NMF algorithm can incorrectly partition intensity between equivalent reflection positions in different components. VDF analysis can be used as a supplementary tool to provide more insight into crystallographic variations.

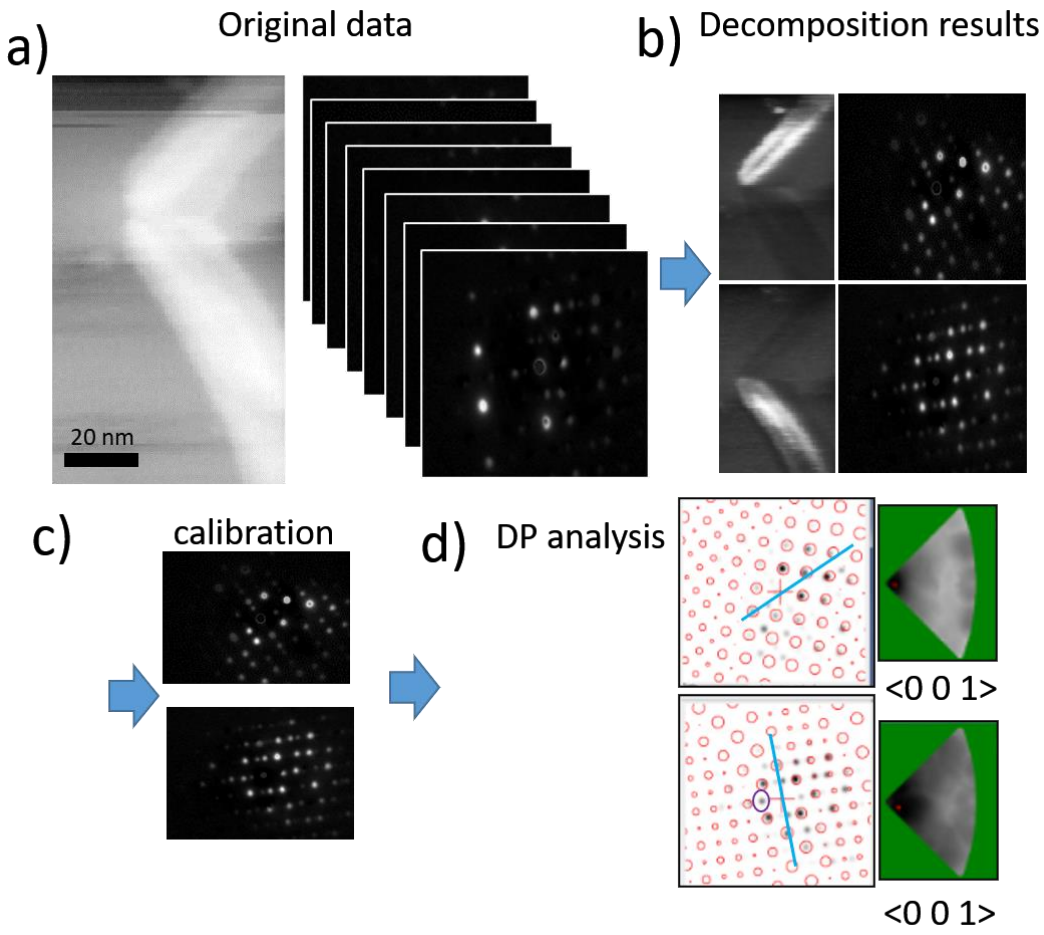

Figure 3-7 PED data decomposition and diffraction pattern indexation process. (a)original data obtained from scanning PED experiments. (b) The previous 4D data is decomposed to VDF images and corresponding diffraction patterns. (c) calibrate the diffraction patterns through distortion. (d) Diffraction pattern indexation through the correlation index, as well as considering other factors, which are the growth directions in this case.

3.2.3 Diffraction pattern indexation

It is worth noting that the diffraction pattern is captured from the tilted viewing screen by a high-speed digital camera outside the TEM. To analyse the diffraction patterns, the images are initially corrected for geometric distortions of the pattern (Figure 3-7c). This is typically done for a low-order zone-axis pattern and the correction is applied to all subsequent patterns. Then a correlation index is introduced to evaluable the degree of matching between experimental patterns and simulated templates, and the correlation index Q is shown in equation:[191]

$$Q(i) = \frac{\sum_{j=1}^{m} P(x_j y_j) T_i(x_j y_j)}{\sqrt{\sum_{j=1}^{m} P^2(x_j y_j)} \sqrt{\sum_{j=1}^{m} T_i^2(x_j y_j)}} \quad (1)$$

where P(x, y) is the diffraction patterns and Ti(x, y) is the template. For each template i, Q(i) is proportional to the sum over the entire range of coordinates (x, y) of the product of the intensities related to the diffraction pattern and the template. The correlation indices calculated for every orientation are plotted in the fraction of stereographic projection (indexation map), where all possible orientations are listed out and the darker region indicates the higher correlation indices Q. This algorithm is provided as part of the ASTAR system, and it has been successfully applied to determine the orientation of many materials, such as Ni-base superalloys with multi-phases[16] and ZnO NW nucleus.[177]

Eggeman et al.[16] used this method to analyse the crystal microstructure Ni-base superalloy ATI 718Plus, which contains a Ni-rich FCC matrix strengthened with many kinds of precipitates. Even though the superalloy contains about 20 main crystal components inside, they still obtained reliable matched diffraction patterns corresponding to every major phase, proving the great potential of the correlation indexation method following the NMF decomposition in crystal structure analysis.

However, the diffraction patterns produced by decomposition are difficult to precisely match with the simulated templates. One reason is that the algorithm cannot distinguish the proportion of the contributions from different subcrystals due to the coherence of some patterns from different zone axes. In this case, the brightness of the patterns may not be the same as the kinetic modelling results, so their presence and absence is the main consideration for analysis. On the other hand, the noise in the data and imperfections of decomposition still exist, so the possibility of a very small portion of the diffraction spots being misallocated should not be excluded. In this case, guided by the decomposition and template matching, some other factors/indicators also need to be considered to analyse the reliability of indexation. For example, for the data shown in Figure 3-7d, the NWs on two sides of the boundaries have the same growth direction but form an angle of about 70 ^{o} with each other, so the diffraction patterns should also be rotated by a similar angle in reciprocal space; if the zone axes of two subcrystals are the same and the indexation solution does not fulfil this condition, it should be abandoned. This behaviour is by the blue lines in Figure 3-7d, representing the <1 1 0> wire growth direction. While there are numerous possible angles between the <1 1 0> directions in these two patterns, this particular set are consistent with the other decomposition factors analysed and provide a complete description of the NW orientation on either side of the bend (Figure 3-7a).

4 Influence of Twin Boundaries and Sample Dimensions on the Mechanical Behaviour of Ag Nanowires

4.1 Introduction

Networks of silver nanowires (NWs) are promising candidates for flexible and transparent thin film conductors. They exhibit remarkable mechanical reliability under cyclic bending,

high conductivity and optical transparency.[22,36,192] Ag nanowires can be synthesised by the highly scalable polyol process,[32,193] and are readily available commercially from a number of suppliers. Ag NWs produced by the polyol process have a characteristic pentagonal prism structure consisting of five sub crystals sharing a common axis along the <110> direction, separated by {111} Σ3 twin boundaries,[194] and are conventionally described as pentatwinned Ag NWs. The apical angle of the prism is 70.53°, hence the 5 Σ3 boundaries with adjacent sub-crystals are accommodated by an elastic strain due to the 7.35° closure angle required to form the pentatwinned structure.[195,39,10] This can be modelled as a disclination defect, or possibly 5 symmetrically oriented disclinations with an individual angle of 1.47°.[196] For applications such as flexible or stretchable conductors networks of Ag NWs will be subject to significant elastic and plastic strains, hence an understanding of the mechanical behaviour of individual nanowires is required. The pentatwinned structure of the NWs and the considerable intrinsic elastic strain may influence the mechanical properties. Here we present a study comparing the mechanical properties of pentatwinned Ag NWs with single crystal Ag NWs of similar dimensions.

It is now well established that the compression strength of metallic micropillars with diameter < 5 μm increases with decreasing sample diameter. This observation was first noted by Uchic et al.[59,197] with experiments on Ni specimens and confirmed by other studies showing a strong dependence of compression strength on pillar diameter.[60,63,67,72] Similar size dependent mechanical behaviour is seen in other samples with reduced dimensions, e.g. in thin metal films.[198] It is generally believed that confinement of the reduced specimen dimension constrains dislocation processes and that the presence of the surface strongly influences mechanical behaviours.[198,199] Greer and Nix proposed the small sample size and proximity of the free surfaces leads to any mobile dislocation population exiting the samples, leading to dislocation starvation,[60] with further deformation requiring the generation of new dislocations.

An alternative mechanism was proposed by Parthasarathy *et al.* [103], who argued that conventional (Frank-Read) dislocation sources are likely to be larger than the pillar diameter and that the appropriate source will consist of a dislocation segment pinned at one end, with a free end intersecting the surface to form a "single-arm source". The dislocation starvation mechanism (or mechanical annealing) is supported by observation of the removal of dislocations during the deformation of Ni pillars *in situ* in the transmission electron microscope (TEM).[74] However, dislocation structures similar to those predicted for the single arm source model have also been observed in deformed micropillars.[80] There has been little consideration of the tensile deformation of submicron metallic structures but it is likely that similar size dependent phenomena occur.

A key difference between solution synthesised Ag NWs and the materials studied in most of the prior work on the influence of specimen size on mechanical properties is the presence of the 5 twin boundaries running parallel to the wire axis. In bulk metals, twin boundaries can act as both a source/sink and a barrier to dislocations, which may subsequently improve the strength and ductility of materials under some conditions.[25,44] Imrich et al.[200,201] studied the deformation of copper micropillars containing single twin boundaries oriented parallel to, or at small angular deviations from, the pillar axis. They reported little change in the pillar mechanical properties when compared with equivalent single crystal specimens, although they noted that the predominant dislocation activity did not cross the twin boundary. These observations were supported by dislocation dynamic modelling work,[202] where it was found that twin boundaries oriented parallel to the loading axis have little influence on mechanical properties. However, the pentatwinned structure of Ag NWs confines dislocation migration such that interaction between the twin boundaries and migrating dislocations is inevitable. In addition, there is a continuity constraint requiring deformation in each individual subcrystal

to correlate during plastic deformation. Recent work by the authors[194] has shown that there is also a strong crystallographic constraint during deformation of an intact pentatwinned NW.

There has been limited experimental investigation and modelling of the tensile mechanical properties of Ag NWs and the influence of the twinned microstructure. Nanomechanical testing of Ag NWs revealed a strong size effect, with the yield stress increasing rapidly with decreasing diameter and exceeding 2.5 GPa at diameters close to 30 nm. [90,142] Strong strain hardening was seen with the smaller diameter pillars and there is clear evidence of dislocation nucleation and storage after deformation.[139] However, because of the difficulties in sample preparation, most tensile tests are conducted using pentatwinned Ag NWs with diameter in the range 30 - 130 nm with a limited number of samples, which makes a definitive identification of a size effect difficult to confirm. Molecular dynamic (MD) modelling has suggested that co-operative deformation in parallel subcrystals leads pentagonal stacking fault pyramids (SFP) or decahedra (SFD).[13,139] Such structures may lead to local dislocation pile up generating kinematic hardening and provide a mechanism for plastic strain recovery reported after the cyclic deformation of NWs. [11,122] It should be noted that the proposed pentagonal SFP and SFD structures have never been clearly observed after tensile tests of pentatwinned Ag NWs. This study explores the mechanical responses of Ag NWs by comparing the pentatwinned Ag NWs with similarly sized single crystal NWs using *in situ* mechanical testing in a scanning electron microscope (SEM). Structural characterizations of deformed NWs using TEM is used to further understand the influence of sample dimensions and twin structures on the size effect.

This chapter is based on a paper. Hu Zhao, Halil Yilmaz, Craig J Williams, Alexander S. Eggeman and Brian Derby, 'Influence of Twin Boundaries and Sample Dimensions on the

Mechanical Behaviour of Ag Nanowires', in preparation for 'Materials Science and Engineering A'. Hu Zhao conducted the main experiments and prepared the draft; the preliminary experiments were done by Halil Yilmaz and Craig J Williams; Alexander S. Eggeman and Brian Derby provided guidance and helped revise the draft.

4.2 Materials and Methods

This study used pentatwinned Ag NWs synthesised by polyol process (ACS Materials, Medford, USA) with diameters in the range 60 - 250 nm and with mean length approximately 6 μm. Single crystal Ag NWs of similar dimensions were fabricated by electrodeposition within an anodized aluminium oxide template, full details of this method are published in an earlier study.[194] *In situ* tension tests were conducted using a Hysitron PI85 Pico-indenter nanomechanical testing stage (Bruker Hysitron, Eden Prairie, USA) mounted in a Zeiss Sigma VP SEM (Carl Zeiss, Jena, Germany). A 20 μm flat punch tip was used, with load and displacement resolution of 3 nN and 0.02 nm respectively. In order to achieve tensile loading of the nanowires, they finally were fixed to a push-to-pull (PTP) holder (Figure 4-1b). Microstructures of the NW specimens were characterized after testing using a Talos F200A transmission electron microscope (TEM) (Thermo Fisher Scientific, Eindhoven, Netherlands), operating at 200 kV with point resolution of 0.25nm.

The following procedure was used to prepare both pentatwinned and single crystal Ag NW specimens for testing. NWs were dispersed as a dilute suspension in isopropyl alcohol. Several drops of suspension were dispensed onto copper grids (1200 mesh) dried and examined within a dual beam focused ion beam milling device (FIB/SEM; Helios Nanolab 660, Thermo Fisher Scientific). NWs were selected where one end was attached to the grid and the other end was suspended freely. The free end of the NW was attached to the tip of the manipulator probe using platinum deposition. Subsequently, the other side of the wire was

severed using the ion-beam, allowing a single wire to be transferred to the PTP holder. Care was taken during transfer of the NW to ensure good alignment of the NW with the tensile axis of the loading device as it was placed over the gap between the two ends of the loading device. The aligned wire was fixed onto the PTP devices by further induced Pt deposition (Figure 4-1a).

Mechanical testing experiments were conducted under load control with a constant loading rate of 1 $\mu N.s^{-1}$ (Figure 1b). The value of the displacement was measured using the capacitive gauge in the indenter set up. Engineering stress was determined by dividing the load by the initial area of the NWs. Single crystal NWs were assumed to be of circular cross section and the area calculated from the measured diameter accordingly. The cross section of the pentatwinned NWs A_{p5} was estimated as an ideal pentagon using the apparent width of the NW as a diameter, *d*, from which the cross-sectional area is calculated, as follows:

$$A_{p5} = 5d^2/8(\sin 72)^2 \qquad (4-1)$$

There is considerable uncertainty in the precise gauge length of each nanowire tested because of the nature of the Pt deposition process used to secure the ends in the PTP holder, hence no attempt was made to calculate the strain in the specimen. It is also noted that the Pt deposition leads to irregular deposition of Pt along the nanowire with about 5 – 10 nm depth and this may also affect the accuracy of the calculated engineering stress.

4.3 Results and discussion

4.3.1 Undeformed NW structure

Pentatwinned NWs are straight and uniform in width (Figure 4-1c, inset). There is clear contrast evident in the TEM image from the twin boundaries parallel to the fibre axis. Selected area electron diffraction (SAED) patterns from individual NWs perpendicular to the

incident electron beam are shown in Figure 1c. Overlap of different sub-crystals means that this pattern contains a number of diffraction spots from different orientations of the Ag crystal structure. In Figure 4-1c, the solid red square indicates reflections arising from the [0 0 1] zone axis while the dotted red square corresponds to reflections arising from a crystal oriented parallel to $[1\,\bar{1}2]$. This particular combination of patterns is indicative of the electron beam being normal to one of the facets of the pentatwinned structure with crystal growth orientation [110].[203] Figure 1d shows TEM results from single crystal Ag NWs synthesized by electrodeposition. The TEM image (inset in Figure 4-1d) shows uniform contrast and the fluctuations in diameter are from the surface of the AAO template. The zone axis of the diffraction pattern in Figure 4-1d is $[\bar{1}12]$, which is consistent with previous observations that the preferred growth orientation of Ag NWs fabricated by electrodeposition is [110].[160] Both the penta-twined and single crystal Ag NWs show identical growth orientation. This facilitates the interpretation of the role of TBs on NW mechanical performances because both specimens are loaded along a common crystal direction. Cross sections of three pentatwinned NWs with different diameters are shown in Figure 4-1e – 1g. In all three images the pentagonal arrangement of the twinned subcrystals is evident. However, it is notable that the smallest diameter wires show a distinct surface curvature rather than a faceted pentagonal prism morphology. Previous work characterizing pentatwinned nanowire cross-sections has found that the five twin boundaries are not identical and that at least two of the five show significant defect levels, the presence of which accommodates the disclination associated with the pentatwinned structure.[11,196]

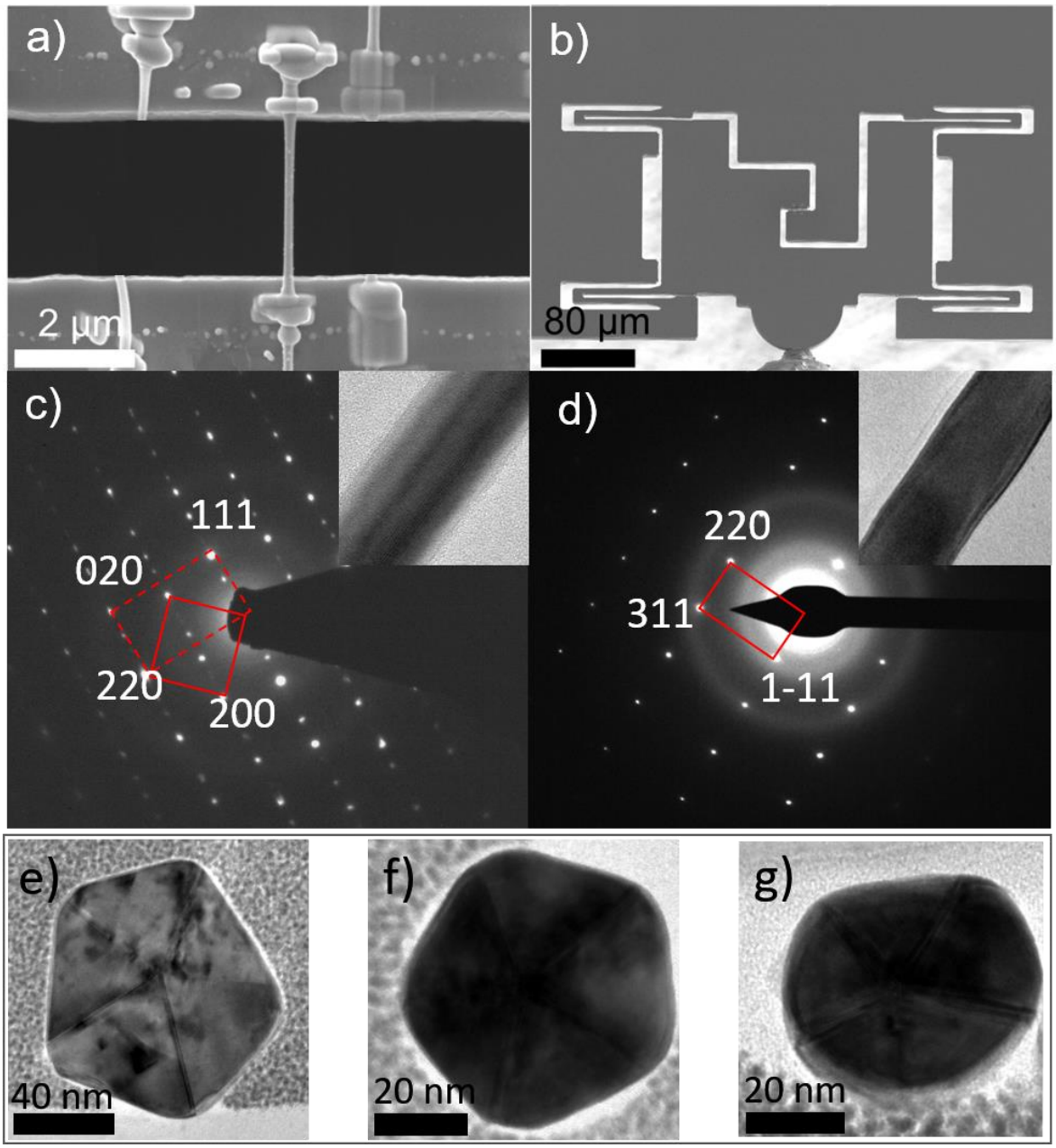

Figure 4-1 The tensile tests experiments process in SEM and Ag NWs microstructure characterization. (a) Prepared samples fixed on push-to-pull devices by Pt deposition for tensile tests (b) SEM in-situ tensile tests using pico-indenter. (c) are the selected area diffraction patterns of the pentatwinned Ag NWs (inset), where the indexed patterns show the overlap of two crystal zone axes, [0 0 1] (solid rectangular) and [1 $\bar{1}$ 2] (dashed rectangular). (d) is the diffraction pattern of single crystal NWs (inset), the zone axis of which is [$\bar{1}$ 1 2]. (e)-(g) Cross section of pentatwinned Ag NWs with different diameters of (e) 102 nm, (f) 58 nm and (g) 51 nm with the same scale bar.

4.3.2 Mechanical Testing

The Ag NWs fixed on PTP devices were tested in tension *in situ* in the SEM and a sequence of images showing deformation leading to fracture are presented in Figure 4-2a – 2c. The displacement-stress curves from all individually tested NWs are shown in Figure 4-2d. From Figure 4-2d, the ultimate tensile strength (UTS) of the strongest pentatwinned Ag NW tested,

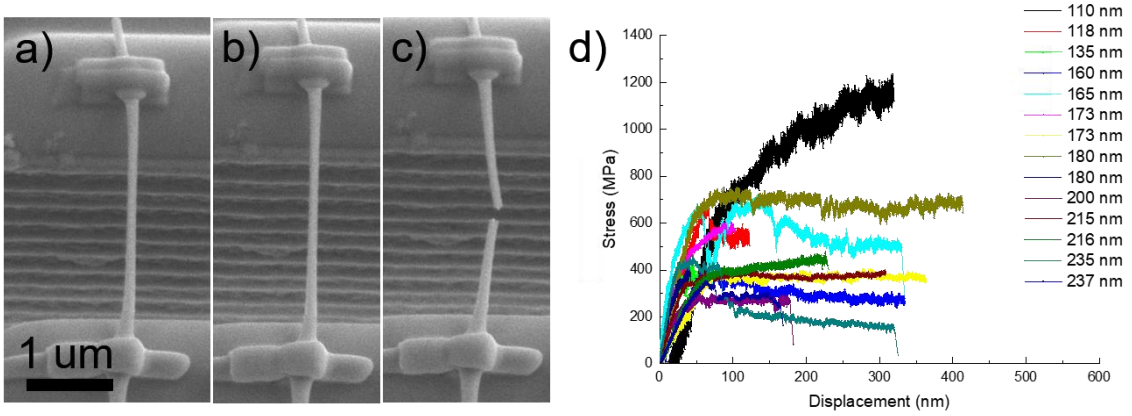

Figure 4-2 (a) - (c) Sequence SEM images recording the deformation of the individual NW during tensile tests. (d) displacement-stress curves of all pentatwinned Ag NWs tested individually.

with a diameter of 110 nm is approximately 1.2 GPa. Most of the wires tested show elastic-plastic behaviour with negligible work hardening after yield. When testing FCC metal submicron pillars under compression, discrete strain bursts throughout the deformation, without obvious stress reduction, is widely observed, which is interpreted as indicating a dislocation starvation state within the pillar after each burst.[60] We did not see strain bursts in our experiments. This may be due to the load-controlled testing, or possibly indicates that the instability of tension loading means a strain burst will lead to fracture. However, Filleter et al.[13] reported strain bursts during the tensile tests of pentatwinned Ag NWs with a diameter <

100 nm. They proposed this to be caused by the formation of linear chains of SFDs, and this will be discussed later in this study.

Even though all the wires are prepared carefully and tested with constant loading rates, the observed mechanical behaviours of wires with similar diameters are not identical. There is a noticeable scatter in the UTS value for wires of similar diameter and also considerable variation in the gradient of the stress/deflection trace in the elastic region. There are a number of possible reasons for these observations. First, as mentioned earlier, the NWs are fixed to the PTP device by Pt deposition during specimen preparation for tensile testing and hence the true gauge length cannot be determined, possibly explaining the inconsistent gradient of the elastic region of the test measurements; in addition, re-deposition of platinum on the NW surface is inevitable, which results in inconsistent NW diameter values and surface conditions of the NWs. It is also possible that the microstructures of the NWs with similar diameters may still vary from each other, e.g., differences in the shape and cross-section area of each subcrystal and initial dislocation densities; it is also possible that further defects may be created during sample preparation and transportation. These uncertainties suggest a large population of NWs need to be tested under uniform conditions to generate sufficient data to draw reliable conclusions.

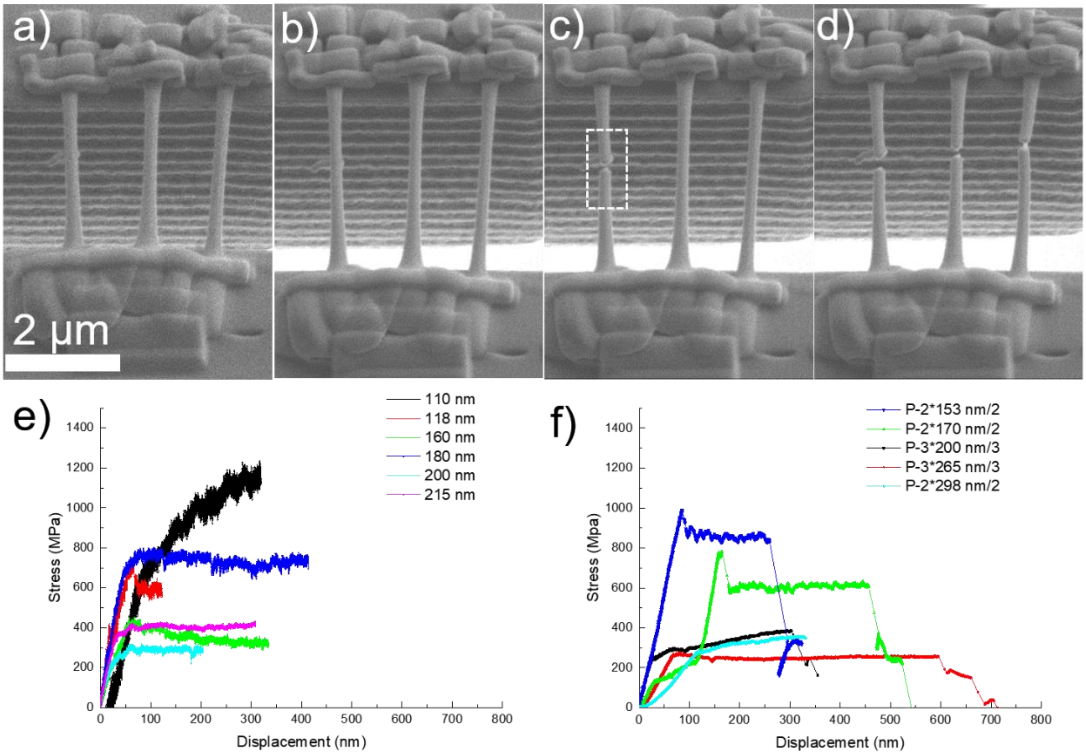

Figure 4-3 SEM images recorded during tensile tests of three pentatwinned Ag NWs simultaneously and the displacement-stress curves of pentatwinned Ag NWs. (a)-(d) are the sequence images, where one wire starts to fail in (c) first, and the other two fail subsequently. (e) Mechanical performances of some particular individual NWs (f)The average displacement-stress curves of pentatwinned Ag NWs that are tested two/three together; for example, p-3*200 nm/3 indicates the average displacement-stress curves of each 200 nm pentatwinned Ag NWs tested three together.

One method to check the mechanical response of the NWs is testing two/three wires with the same diameter simultaneously under tension, as the strength errors due to some defects in one NW introduced during sample preparation can be reduced through using the average strength of several NWs. In addition, the increased force supported by the NWs compared to the elastic response of the PTP device will decrease the noise floor, thus improving the measurement accuracy. The multiple NWs deformation process recorded from tests within the SEM are presented in Figure 4-3a-d. The strength of NWs with diameters from 150 to 180 nm (Figure 4-3f) is a similar range with the values of NWs tested individually (Figure 4-3e), which is around 600 MPa, higher than the strength of NWs above 200 nm.

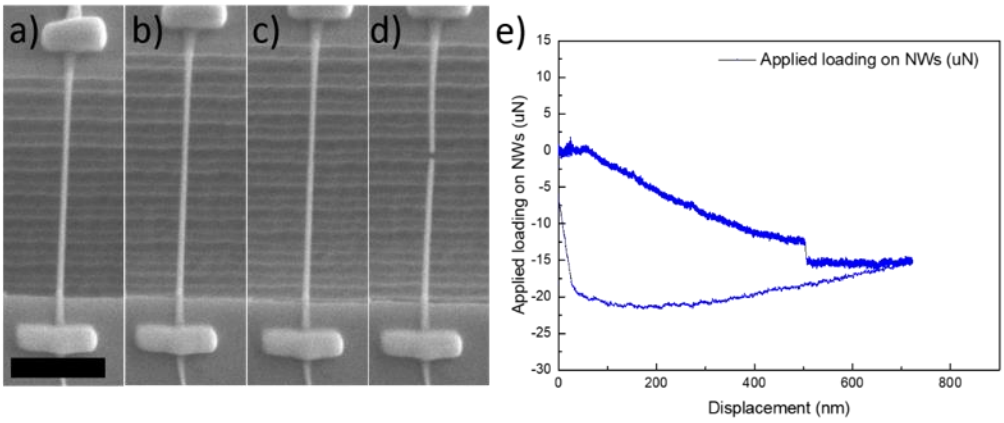

Figure 4-4 Tests of Ag NWs with diameter below 100 nm. Sequence images of tensile tests of pentatwinned Ag NWs with a diameter of 70 nm under SEM (a)-(d). (e) is the loading-displacement data after removing the spring stiffness of PTP devices from original data.

In this study, the PTP device was chosen to ensure the NWs alignment during tensile tests. Compared with the method using AFM cantilever to gain loading values,[90] this way makes it possible to monitor the mechanical responses of individual wires under high feedback frequency. However, the adoption of the PTP device, to allow tension loading, means that the loading-displacement data from the pico-indenter contains the stiffness of the PTP spring, and removing this value precisely becomes very difficult when testing wires of the diameter below 100 nm. On the other hand, the stiffness of the spring could not be too small to protect the samples from environmental vibration damages. One pentatwinned Ag NW with diameter of 70 nm tested under tension is shown in Figure 4-4. After removing the PTP spring stiffness from the original data, the loading could be even negative in some circumstances (Figure 4-4e), which is unreasonable and indicates that the stiffness of PTP spring is not constant. When the NWs are very strong, these minor changes on PTP spring value can be ignored, but for tests carried out on Ag NWs with the diameter < 100 nm the this is unacceptable. Regardless of the difficulties in getting reliable displacement-stress curves of Ag NWs below 100 nm, using the reduced values of loading when the NW breaks to calculate the UTS, which is defined as the maximum stress that the NWs can withstand under tension, is still

possible, as the feedback rate is 78 kHz for pico-indenter controller and the dropped value only relies on the strength of the NWs. Combining the data provided by the above process and the strength extracted from previously displacement-stress curves, the UTS of 25 pentatwinned Ag NWs and 5 single crystal Ag NWs with the diameter ranging from 70 to 320 nm was obtained.

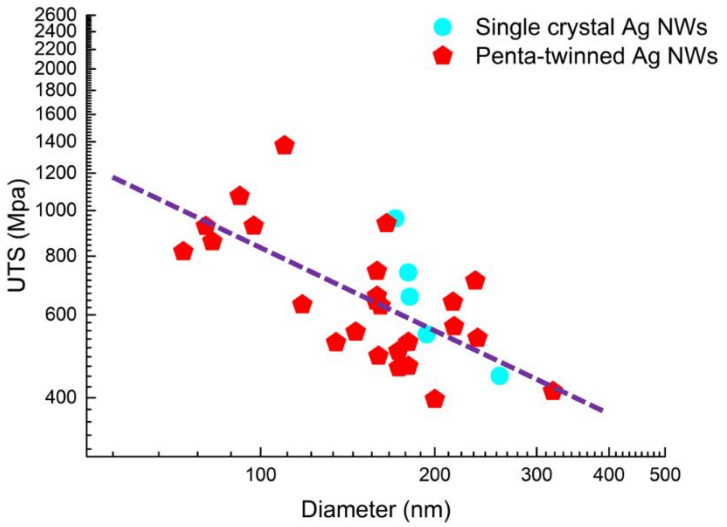

Figure 4-5 Ultimate tensile strength (UTS) of pentatwinned Ag NWs and single crystal Ag NWs tested in this work, plotted against pillar diameter. The line shows a linear fit to the plot producing a power law exponent for the Ag NWs of n = -0.57.

The UTS values obtained from our experiments are from pentatwinned Ag NWs (red symbols) and single crystal Ag NWs (blue symbols) with the diameter ranging from 70 to 320 nm are presented in Figure 4-5. There appears to be a clear size effect, with the gradient of the log-log plot (power law exponent), n = -0.57 (Figure 4-5). However, we must first consider the effect of the experimental uncertainties that have been identified and discussed previously on whether this apparent size effect is likely. These data are from both single crystal and pentatwinned NWs with the single crystal data identified in blue. Thus far we have ignored the influence of the Pt redeposition on the strength of the NWs but it will have an influence. The Pt forms an amorphous coating of thickness 5 – 10 nm on all the specimens

tested. The strength of this layer has not been determined but in the literature its strength is estimated to be 500 – 1000 MPa.[204,205] Thus, assuming a constant thickness of Pt on all the NWs tested, we would expect the smallest specimens to be about 150 MPa stronger than the largest in these tests, which is significantly smaller than the scatter in stress around a given diameter in Figure 4-5 and also significantly smaller than the observed difference in strength across the size range studied.

In addition to the impacts of redeposition on the measured strength of Ag NWs, the factors that may affect the strain measurement and their influences on strength measurement are also evaluated here.

There is a considerable variation in the apparent elastic modulus of the Ag NWs as indicated by the linear region of the load-displacement measurement. The gradient of this region is consistently lower than that expected from the bulk elastic modulus of Ag. Although the redeposition of Pt may have an effect, as discussed earlier this alone is insufficient to explain the discrepancy and would lead to an apparent increase in the gradient (a greater sample area should lead to a decrease in extension for a given load). The most likely mechanisms for this discrepancy are likely to be associated with the Pt fixing to the PTP stage and the introduction of uncalibrated deformation either within the Pt deposit or at the Pt/Si (PTP devices) or Pt/Ag interfaces. There could also be an unrecoverable strain (plastic deformation or interfacial sliding) within the deposited fixture that is not revealed because all tests were continued until nanowire fracture. Considering that the elastic deformation displacement for the above samples only ranges from 50 to 100 nm, the compliance of tens of nanometers may be not obvious in experiments while it could introduce large errors in elastic strain measurements, leading to the varies in elastic deformation region of these NWs. However, these mechanisms would not influence the load on the nanowire and thus do not affect the mechanical strength measurements despite reducing the apparent elastic modulus. This

hypothesis could be confirmed by a series of experiments loading and unloading the fibres within the linear deformation regime to see if any unrecovered deformation occurs. This is suggested as an area for investigation for a future study.

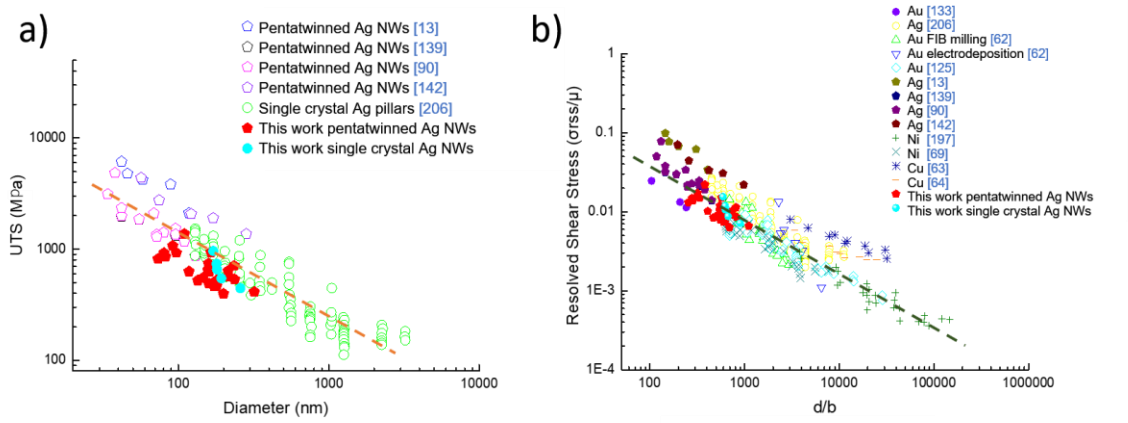

Figure 4-6 The size effect of Ag NWs and other FCC metals. (a) Strength of single crystal Ag nanowires/pillars and pentatwinned Ag NWs form this work and published papers, plotted against normalized pillar diameter. The power law exponent of all these samples is -0.75 (dashed orange line). (b) Flow stress/UTS of some FCC metals normalized by the shear modulus in the {1 1 1}<1 1 0> slip system, plotted against pillar diameter normalized by the Burgers vector. The power law exponent of the dashed green line is -0.66, which is the exponent in Dou and Derby's work.[66]

4.3.3 Size Effects

This study indicates that the mechanical behaviours of Ag NWs are most strongly influenced by the sample dimensions. A comparison of our data from both single crystal Ag NWs and pentatwinned Ag NWs with other published work on the mechanical behaviour of pentatwinned NWs and Ag micropillars is presented in Figure 4-6a.[13,90,139,142,206] Our data (solid symbols) sits amongst the published data and is consistent with the empirical size effect. All the published data shows a similar scatter in the strength values as we observed. A further comparison with the published data for a range of other FCC metals (tested as micropillars in compression) is presented in Figure 4-6b.[62–64,69,125,133,197] The comparison is achieved using the normalization proposed by Dou and Derby,[66] with NW diameter normalized by the Burgers vector and strength by the shear modulus resolved on the

dominant slip system, in this case $\{111\}\langle 1\bar{1}0\rangle$. Figure 4-6b also shows the empirical relation relating micropillar/nanowire strength to diameter proposed by Dou and Derby,[66]

$$\frac{\sigma}{\mu} = A\left(\frac{d}{b}\right)^{n} \tag{4-2}$$

where σ is the plastic flow stress, μ is the resolved shear modulus, d is the NW/micropillar diameter, b is the Burgers vector, and both A and n are empirical constants; in this case n = -0.67. These comparisons indicate that not only is there no discernible differences in the strength of single crystal and pentatwinned Ag NWs but also that the size dependent strength of these NWs follows a very similar trend to that seen with a number of FCC materials tested as single crystal pillars or NWs.

4.3.4 TEM Characterization of Deformed NWs

To investigate the microstructure of pentatwinned and single crystal Ag NWs after fracture, individual NWs were pulled to failure under tensile stress using the manipulator in a FIB. First, individual Ag NWs are picked up using the manipulator and Pt deposition in FIB (Figure 4-7a). Then the free end of the NWs is fixed on the TEM copper grids and fixed using Pt deposition (Figure 4-7b and c). The tensile loading is applied through moving the manipulator, and the rate is 100 nm/s. The failed Ag NWs fixed on Cu grids are observed in TEM subsequently.

The contrast differences in the TEM images are from a number of amplitude contrast and phase contrast mechanisms that alter the scattering of the incident electron waves by the samples[207]. In this research, most of the contrast are from changes to the diffraction condition and materials thickness. In Figure 4-8, a bright field image, the dislocations will show a dark line contrast as the strain field of the dislocation alters the crystal orientation allowing more

electron scattering compared with the pristine crystal and hence a reduction in the image brightness. Considering that the angle between NW growth direction <1 1 0> and the activate slipping planes {1 1 1} is 54 °, very close to the inclined angle of the observed line contrast, these contrasts should indicate the dislocation slips in the NWs.

Figure 4-8b shows a series of dislocations running through an individual subcrystal in a pentatwinned NW of diameter 135 nm. These images show that although dislocations are able to nucleate at the NW surface and propagate through the subcrystal, they end abruptly at the centre of the NW. This is not unexpected as the crystal orientation across the TBs means that slip systems able to accommodate the dislocation are unlikely to exist or else be under insufficient shear stress to be active. Furthermore, they may be impeded by the intrinsic stress field due to the angular mismatch (7.35°) associated with the pentatwinned structure. The barrier effect of TBs is also broadly supported by studies of TB-dislocation interactions in bulk twinned FCC metals, [25] where a similar behaviour to the Hall-Petch relation for grain boundaries is observed.[43]

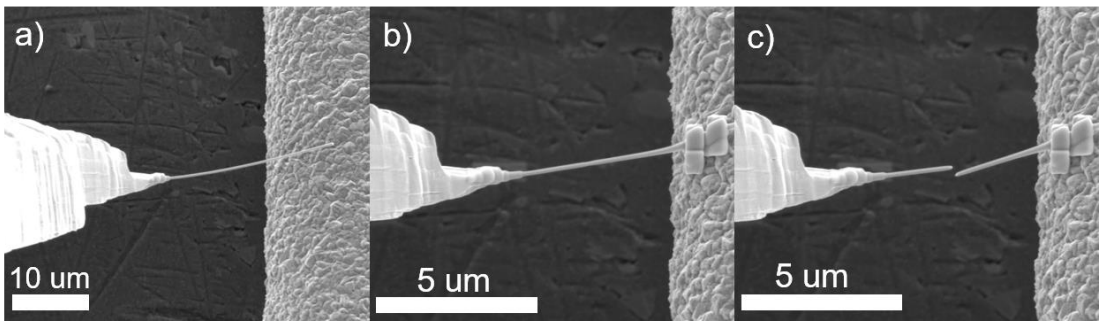

Figure 4-7 Tensile loading on individual Ag NWs to prepare samples for subsequent TEM microstructure characterization. (a) One Ag NW is pick up using the manipulator probe in FIB. (b)The other side of the NW is fixed on TEM Cu grids using platinum deposition. (c) The manipulator probe is moved horizontally to impose tension loading on the wire.

What is less clear, is whether the blocked dislocations transmit pile-up stress through the boundaries (or if partial dislocations can migrate across the boundaries at higher stress). Figure 4-8c shows that there is clearly simultaneous plastic deformation in multiple sub-

crystals close to the point of failure in the NW that may be the result of dislocation transmission between sub-crystals. One possibility is that slip blocking in one subcrystal will increase the local shear stress in the adjacent subcrystals. If slip occurs in multiple subcrystals in the same locality, then the overall increase in stress may be sufficient to activate dislocation transfer and so create a local plastic region where necking and subsequent failure occurs. Although the dislocations are rapidly stopped by the twin structure they do so in an extremely predictable way and the slip can easily expand to allow continual plastic deformation at a negligible increase in applied stress. The scatter in ductility would appear to arise from the likelihood of dislocations nucleating in multiple sub-crystals in close proximity (along the wire length). If nucleation is random, then we would expect significant plastic deformation before dislocations interact, whereas a defective surface might nucleate dislocations closer together.

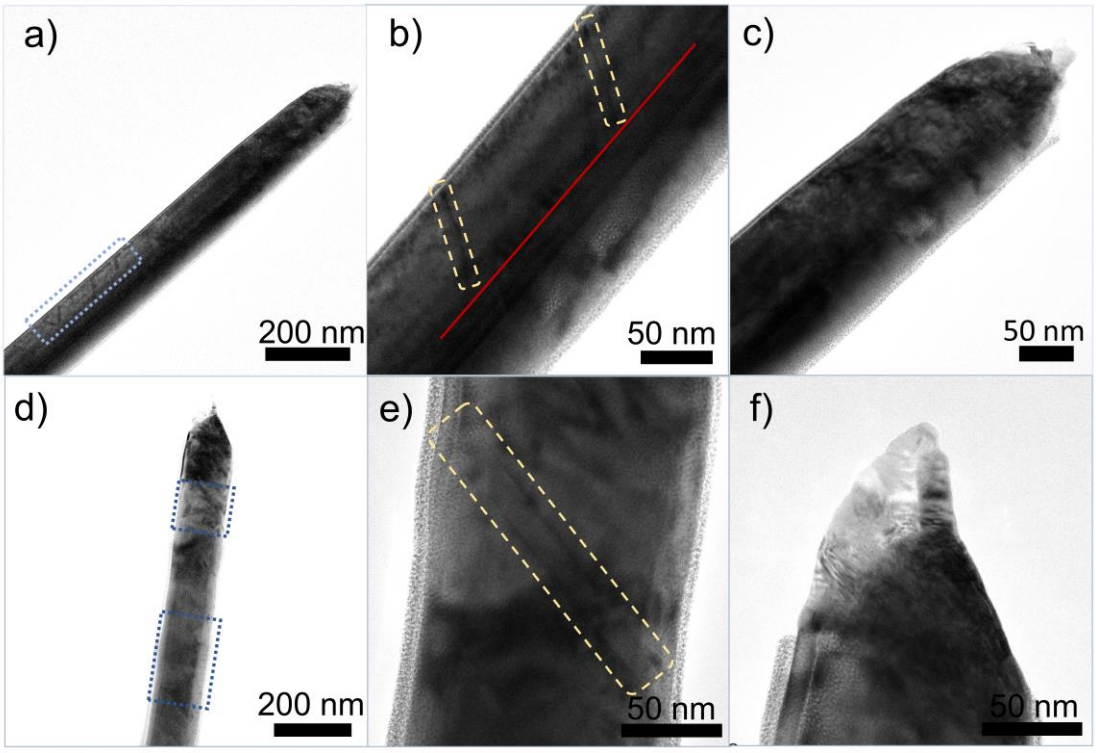

Figure 4-8 TEM images of failed Ag NWs under tension. Images (a – c) are from a 135 nm diameter pentatwinned NW; images (d – f) are from a single crystal NW also of diameter 135 nm. (a) A series of parallel inclined defects are visible in a single subcrystal of a deformed

pentatwinned NW at an angle consistent with a (111) lattice plane. (b) Enlarged image of the region outlined in (a), defects are seen to terminate at the centre of the NW, close to a subcrystal boundary (identified by the red line). (c) Image of the fractured end of the pentatwinned NW, with obvious necking and a high local dislocation density. (d) A deformed single crystal Ag NW showing intersecting defects along common {111} planes (in the dashed square). (e) A higher magnification image of the upper region identified in (d), the angle between the outlined defect and the NW growth direction is 54°, consistent with the {111} orientation. (f) image of the fractured end of a single crystal NW.

In contrast, the single crystal NWs do not display this internal dislocation blocking and hence behave more like a bulk metal with plastic deformation throughout the structure until intersecting slip systems lead to dislocation interactions. In the absence of such behaviour, single crystal nanowires would be expected to fail in simple shear once dislocation activity was triggered. The single crystal NWs show evidence of slip extending across the entire wire (such as in Figure 4-8d and e) and have far greater contrast associated with dislocation networks. The point of failure in these single crystal NWs (Figure 4-8f) has many similarities to those of the pentatwinned NW as this will likely be at a point of high local plastic deformation where the dislocation density and interactions are maximized.

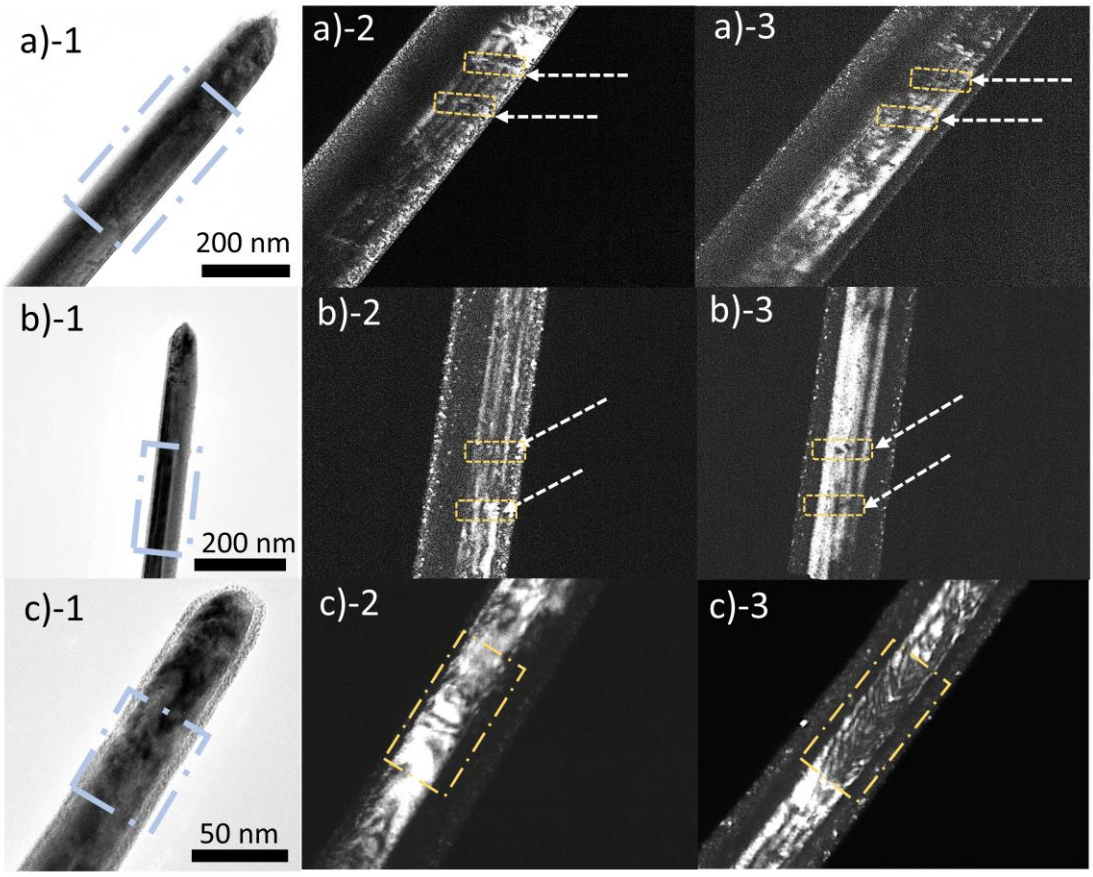

Figure 4-9 TEM micrographs of failed pentatwinned Ag NWs with diameter of (a)-1 135 nm, (b)-1 65 nm and (c)-1 32 nm and corresponding sub-crystal dark field images. (a)-1 to (a)-3 show in the failed NW there are several dislocations, and these slipping extend to adjacent sub-crystals. In the images (b)-1 to (b)-3, plastic deformation region across two sub-crystals still exists, while the dislocation density in the fractured end is reduced compared with above samples. (a)-3 to (d)-3 shows there are multi-plastic deformation regions in the deformed NWs, and the defects are normal to the crystal growth direction.

The effect of decreasing NW diameter on the deformation mechanisms in the pentatwinned NWs is explored in Figure 4-9 using wires of diameter 135, 65 and 32 nm, respectively. In Figure 4-9, the contrast in the DF images is complex but is still interpretable. When using a FIB to fix the NWs on the probe, some Pt particles are inevitably deposited on the surface of NWs, so there are some bright spots observed in the DF images of NWs (Figure 4-9b-2 and b-3). The line contrast along NW's growth direction in the DF images may be thickness fringes from dynamic scattering that appears due to the wedge shape of some subcrystals and the resulting change in the subcrystal thickness along the electron beam trajectory, as shown

in Figure 4-9a-2 and b-2. In addition to these, there are some lines with dark contrast inclined to the growth direction of NWs, which are thought to be the dislocations/slip activated during NW deformation.

In our research, here are five subcrystals in the pentatwinned Ag NWs, each with a highly coherent relationship to the neighbouring subcrystals, as a result diffracted beams in these samples can overlap and so the corresponding dark-field images can show more than one subcrystal. There is also the possibility of unexpected dynamical effects where a beam in one crystal transmits perfectly into a beam in a second or third crystal. The resulting dynamical intensity would be extremely difficult to interpret.

Hence it is difficult to index all the diffraction patterns in this system, thus increasing the difficulty to identify the direction of the beam that was used to produce the DF images. At the same time, the data of the diffracted beam for each DF images was unfortunately not recorded well during the experiment, however the DF images themselves are still valuable to visualise the dislocations distributions in the nanowires.

The two larger wires are shown in Figure 4-9a and b, with both NWs displaying discrete features parallel to the slip planes much like in Figure 4-8a. Dark field imaging presents some evidence that the slip appears in the same position within adjacent sub-crystals (white arrows), though the complex dynamical contrast from overlapping crystals may be influencing this. Thus, there is the possibility that some dislocation activity can transmit across the TBs. Nonetheless, in both sets of images, the slip deformation appears relatively discrete and localized, with no significant dislocation interactions in these two wires. The third, smaller NW of 32 nm diameter shows quite different behaviour (Figure 4-9c). There is a marked change in the deformation structures, with evidence for more complex dislocation networks

rather than discrete dislocations (Figure 4-9c-3) and possibly deformation twin structures (Figure 4-9c-2).

4.4 Discussion

The clear distinction between the two classes of Ag NWs used in this study is the presence or absence of growth twins running parallel to the tensile axis during testing. Previous work has shown that high densities of growth twins lead to strengthening in bulk Cu samples.[43] The parallels between twin boundaries and high angle grain boundaries as obstacles to dislocation propagation have been observed and noted in the literature.[43,208,209] Here, our observations indicate that there is some transmission of partial dislocations through the twins, which is also consistent with prior studies on the strengthening generated by dislocation/twin interactions.[25] The fact that: 1) we cannot find a significant difference between the mechanical performance of single crystal and pentatwinned Ag NWs in our study and 2) our data is comparable with data in the literature, suggests that the presence of the twin boundaries is insignificant when compared to the well-known intrinsic size effect presented by nanowires.

It is notable that outside the regions close to the fracture of the nanowires there is little evidence for highly localised deformation and although there is some dislocation activity in pairs of adjacent subcrystals, we found none of the characteristic five sided pyramid or decahedral defects predicted in a number of MD studies.[13,122,139] Filleter et al.[13] has suggested that the lack of perfection in experimental pentaprism structures may break the symmetry of predicted deformation structures and this is consistent with the TEM results of Qin et al,[11] who found significant differences in the local structures of the five twin boundaries in the structure. The only samples that showed multiple dislocation activity were the smallest NWs studied and this may explain the greater tendency for strain hardening seen with some of our

tensile tests with smaller diameter NWs and this would be consistent with other studies that suggest smaller NWs show stronger strain hardening.[90,139,142] It is notable that as the diameter of the pentatwinned NWs decrease to < 50 nm, the cross-section becomes more rounded (Figure 4-1). It is possible that a structural change such as this may influence mechanical behaviour, for example some MD studies of nanocrystal deformation have suggested preferential dislocation nucleation at corners.[140] Another well-known size effect in pentatwinned NWs is the elastic strain energy associated with the disclination. This increases with the second power of diameter and can be accommodated by walls of edge dislocations at the twin boundary,[196] which could also provide sites for dislocation nucleation during deformation. Such differences in NW microstructure might explain the greater prevalence for work hardening in the smaller diameter NWs observed in other reports.[13,139]

Previous work using MD modelling has predicted the formation of edge linked stacking faults in adjacent subcrystals by the co-operative action of partial dislocations, leading to SFP or SFD defects.[13,139] Experimental studies in the literature have not found strong evidence for these structures and nor has our work. Our study of penta-twinned Ag NWs deformed under tension found evidence for multiple slip events in a given subcrystal and some evidence for propagation into adjacent subcrystals (Figure 4-9). However, there was no indication of the first dislocation sweeping through all subcrystals to form a five-sided pyramidal SF across the whole structure.

4.5 Conclusions

We have found that the mechanical properties of Ag NWs in the size range of 70 – 320 nm show a size effect. Despite displaying large deformations before failure, neither pentatwinned nor single crystal Ag NWs showed extensive dislocation storage after deformation. In both cases there are parallel defects aligned at 54° to the tensile axis [110], these are stacking

faults on the {111} slip planes generated by the passage of partial dislocations as the agents for deformation of fcc nanostructures. Dislocations in the pentatwinned structures are seen to pass through the radial twins but no evidence was found for the presence of pentahedral defects propagating across all 5 subcrystals in a single NW. TEM studies also found greater retained dislocation density in the smaller diameter NWs. In summary, we have found that the tensile behaviour of single crystal and pentatwinned Ag NWs show considerable similarity and that this is also consistent with the scaled behaviour of larger diameter fcc pillars and wires. The radial twins, characteristic of the pentatwinned structure, appears to have little influence on the micromechanical behaviour of these materials and any influence appears to be minor compared with the observed physical size effect.

5 Geometrical Constraints on the Bending Deformation of Pentatwinned Silver Nanowires

5.1 Introduction

Conventional transparent conductive films are typically made of ceramic oxides such as indium tin oxide (ITO); however these are rigid and brittle, which limits their application where mechanical flexibility is required. Instead, for applications ranging from flexible electronics to wearable technologies, a range of different materials solutions have been proposed; these are mostly centred on 2D materials (such as graphene) or on networks of metallic nanowires embedded in a polymer. Figures of merit developed by De *et al*. indicate that networks of silver nanowires (Ag NWs) currently offer the best balance between optical transparency and sheet resistance, surpassing graphene.[37] Ag NWs may also offer cost benefits because of their well-established solution-based bulk synthetic synthesis compared to CVD grown or mechanically exfoliated graphene.[35,38,210]

One feature of the standard polyol process for Ag NW synthesis is the characteristic pentagonal prism structure of the nanowires, this is shown schematically in Figure 5-1. Growth of pentatwinned Ag NWs initiates from nanoparticle seeds with a decahedral shape displaying {1 1 1} indexed faces, which is the most thermodynamically stable.[211] During precipitation from solution, in the presence of surfactants and polyvinylpyrrolidone (PVP) that is proved to interacte more strongly with the {1 0 0} planes than with the {1 1 1} planes of silver,[35] the atoms are added to uncovered {1 1 1} facets making nanowires show a preferential $[0\,1\,\bar{1}]$ growth direction. Nucleation from multiply twinned decahedral seed crystals presents then they result in the growth of 5 parallel crystals separated by twin boundaries on common {1 1 1} planes with prism faces of type {1 0 0}. In Figure 5-1, the triangular growth facets (outlined blue) are {1 1 1} planes, slightly inclined to the growth direction of <1 1 0>, and the rectangular prismatic plane facets (outlined orange) are {1 0 0} plane. Thus, the nanowire has a multiply twinned structure comprising 5 linked triangular prisms of apical angle 70.53°, with each prism having a Σ3 twin relationship to its neighbours. This leads to an elastically strained prismatic structure with an imperfect angular closure of ≈ 7.35°.

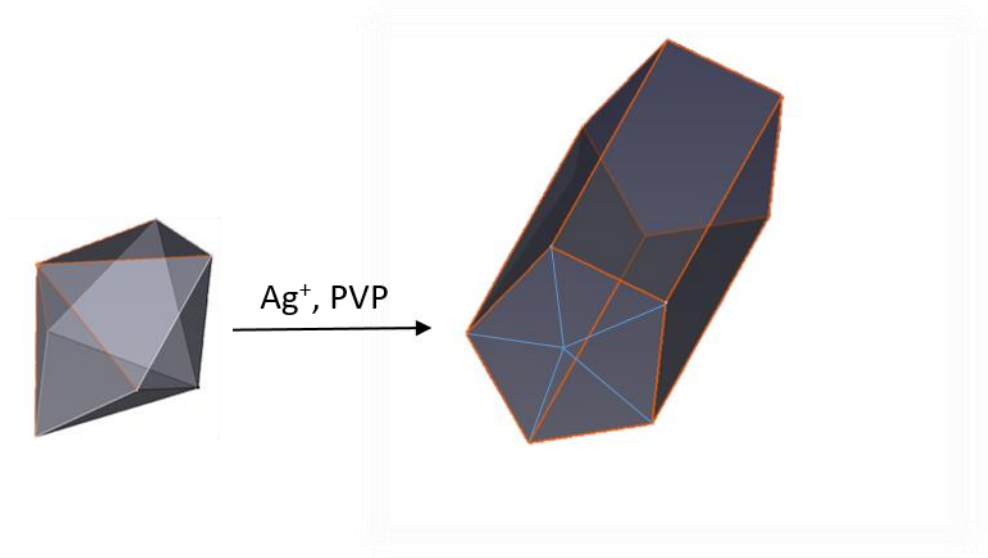

Figure 5-1 Growth of pentatwinned Ag NWs from nanoparticle seeds with a decahedral shape. The triangular growth facets (outlined blue) are {111} planes, slightly inclined to the growth direction of <110>, the rectangular prismatic plane facets (outlined orange) are {100} planes.

For flexible device applications it is essential to have not only predictive but also mechanistic understanding of the performance of materials under large numbers of loading cycles and complex loading geometries. For Ag NW networks there is a small but growing body of experimental work monitoring a decrease in electrical conductivity of the NW networks with increasing strain cycle number, showing a fatigue-like behaviour.[24,83,152] This is reasonable since the network conductivity will depend on the proportions of continuous (pristine) vs broken NWs or NW junctions in the network.[212] The mechanical performance of individual pentatwinned silver nanowires has also been studied. Tension tests carried out using *in situ* straining stages in the electron microscope have shown that Ag NWs have tensile plastic flow strengths much greater than the values for bulk Ag (typically several hundred MPa),[139,213] with the strength increasing as the wire diameter decreases, following a similar relation to that reported for fcc metal micropillars in compression.[66] There is one study comparing the behaviour of pentatwinned and single crystal Ag NWs in tension that reports full recovery of

the deformation of the pentatwinned NW after deformation, but it is not certain that the pentatwinned NW was loaded beyond the yield point in the reported data.[11] Interestingly, studies of the strength in bending of both Ag and Au nanowires show significantly larger values than those reported in tension.[214–216]

Despite this prior work there is still incomplete understanding of the nanomechanical deformation mechanisms of Ag NWs under tensile, compressive or bending stresses. One of the most powerful approaches for studies of individual nanostructures is *in situ* transmission electron microscopy (TEM). Not only can images of the NWs be recorded during deformation but the short wavelength of electrons accelerated to ~100s of kV allows a high spatial resolution as well as sensitivity to individual columns or planes of atoms in the structure. This allows the local atomic arrangement at the point of failure to be analysed. In this study we use TEM and associated analysis of electron diffraction patterns to characterise the bending deformation of Ag NWs, comparing the behaviour of single crystal Ag NWs with that of the pentatwinned structure; thus allowing us to interpret the crystallographic constraints on the deformation of pentatwinned Ag NWs.

This chapter is based on a paper. Hu Zhao, Alexander S. Eggeman, Christopher P. Race and Brian Derby, 'Geometrical constraints on the bending deformation of Penta-twinned silver nanowires', Acta Materialia 18, 110-118 (2020). Hu Zhao conducted all the experiments and prepared the first draft; Christopher P. Race, Alexander S. Eggeman and Brian Derby provided guidance and helped revise the draft.

5.2 Materials and Methods

5.2.1 Ag NWs preparation and their bending behaviour observation under TEM

Pentatwinned Ag NWs synthesised by the polyol process were acquired from commercial sources (NovaWire-Ag-A30 and A60, Novarials, Woburn MA, USA) with diameters in the range 30 - 120 nm. Single crystal Ag NWs were prepared by the method mentioned in experiment section. The manufacturing routes used to produce both sets of Ag NWs are expected to lead to straight, undeformed wires in the pristine state. However subsequent processing steps, e.g., removal of Ag NWs from the growth template (in the case of single crystal NWs), the washing away of the polyol solution (in the case of the pentatwinned NWs) followed by washing, drying and redispersion of the NWs, is expected to lead to their uncontrolled mechanical loading. To ensure that populations of both the single crystal and pentatwinned samples were observed after similar deformation histories, samples in dilute suspension/solution in ethanol were stirred and deposited by spraying on clean and flat Si substrates prior to observation in the scanning electron microscope (SEM). SEM observation was carried out using an Ultra 55 (Zeiss, Germany).

In order to characterise the Ag NWs in the transmission electron microscope (TEM), either in the as-received state or after deformation in solution, the NWs were first dispersed in ethanol as a dilute solution and then deposited by drop-casting onto a broken copper grid with a lacy carbon film. In order to examine the bending of individual NWs *in situ* in the TEM we followed the collodion film method as outlined in the literature.[217,218] First the copper grid with the NWs was put in the bottom of a petri dish (diameter 9 cm) filled with water. To make a collodion thin film with thickness of about 100 nm, 32 μL collodion solution (2% in amyl acetate, Scientific Laboratory Supplies, Nottingham, UK) was dropped on the water in

the flat petri dish. After several minutes, the amyl acetate solution was evaporated and a ≈ 100 nm thin collodion film was floated on the water. Then the water was removed slowly by siphoning and the collodion film became tightly attached to the copper grid with the Ag NWs. After the sample was totally dry, the grid was placed on a conventional TEM holder. Under the electron beam, the collodion film will shrink or bend together with Ag nanowires. Thus, the *in situ* bending deformation of individual Ag NW was observed in the TEM. Experiments were conducted using a Tecnai TF30 (FEI, Eindhoven, Netherlands), operating at 300 kV, with a field-emission gun and a point resolution of 0.14 nm. For scanning nanobeam diffraction experiments, the size of condenser aperture was 10μm corresponding to a convergence semi-angle of ~ 5 mrad, and the microscope spot size.

was 8, leading to a probe diameter of approximately 1 nm.

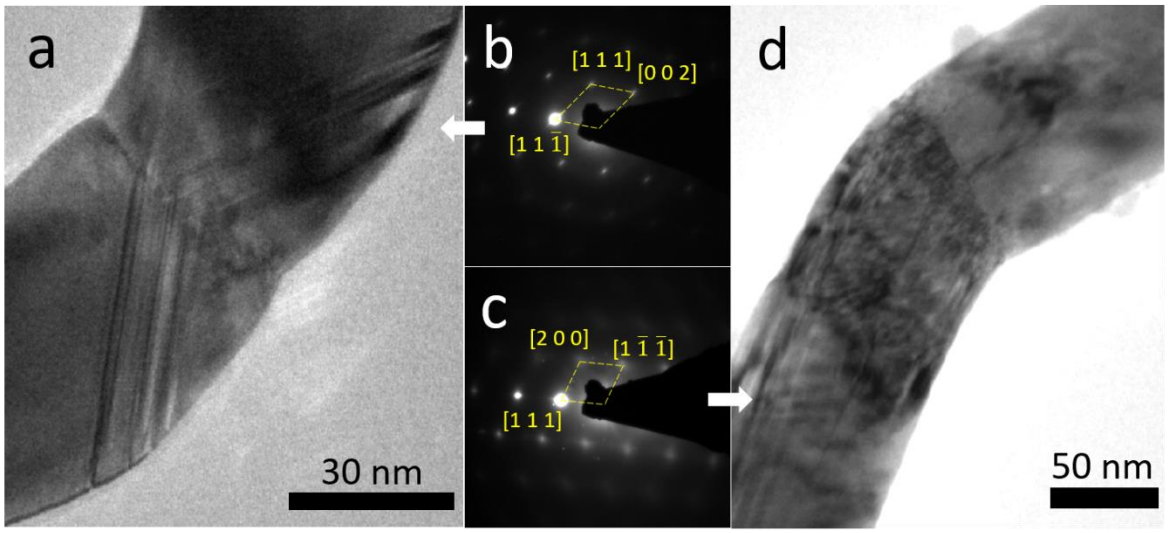

Figure 5-2 TEM micrographs of bent single crystal Ag NWs. (a) A bent single crystal Ag NWs with a diameter of about 52 nm. The corresponding diffraction pattern is shown in (b), which shows that the zone axis is [$\bar{1}$ 10]. (d) Another bent single crystal Ag NW (approximately 85 nm in diameter) with continuous bending area. From (c), the zone axis is confirmed to be [0 $\bar{1}$1].

5.2.2 Machine learning and data analysis.

The scanning precession electron diffraction data were analysed using machine learning approaches implemented in the 'hyperspy' multidimensional data analysis package.[188] This is a set of python libraries that allow multidimensional data to be opened and retains the correct data structure, in this case a 2-dimensional array of positions in the scan (the navigation axes) with each position linked to a 2-dimensional image of the diffraction pattern (the signal axes) resulting in a 4-dimensional data structure. To speed up the analysis a sub-set of the scan area was selected that included the nanowire and a small region of the vacuum surrounding it.

The decomposition was performed by initially transposing the data structure so that the diffraction pattern dimensions became the navigation axes and the scan dimensions the signal. After this the entire structure was re-cast as double precision floating-point values and the hyperspy implementation of non-negative matrix factorisation (NMF) was used to determine the factors of the data. The number of factors was set by the user and was set to be 6 by inspection of the results to see whether the returned factors comparable to virtual dark-field images of the well-defined subcrystals from the wire region (in addition to a vacuum component).

The loading maps for the decomposition showed those diffraction vectors that scattered intensity to the region indicated by each factor. Hence these could be analysed to determine the orientation of the cubic closed packing (CCP) silver crystal structure in that region of the scan by comparison with a library of pre-prepared diffraction patterns. This process was done using the automated crystal orientation mapping (ACOM) software provided as part of the Nanomegas ASTAR package.

5.3 Results

5.3.1 TEM Characterisation

It is well known from previous TEM studies of the deformation of sub-micron diameter metallic pillars and wires that there is little storage of dislocations within the deformed structures, presumably because of the proximity of the free surfaces.[74,219] Figure 5-2 shows TEM micrographs obtained from two single crystal nanowires deformed by bending. Figure 5-2a shows a bright field image from the deformed region in a single crystal NW. The crystal has rotated with a tilt of around 30° and the accompanying electron diffraction pattern (Figure 5-2b) shows that the nanowire has grown along the <110> direction. In this case the crystal rotation is accommodated by the formation of a high angle grain boundary in the bent region. Despite the severe deformation in bending there are few dislocations evident in the deformation zone, though there are a number of twinning defects present lying on parallel planes in the nanowire. Similar structures have been reported from TEM studies of bent single crystal Ni NWs[12]. In this prior work molecular dynamics simulations suggested that a tilt GB formed from a region disordered by the passage of many partial dislocations. Figure 5-2d shows the deformed region in a second single crystal Ag NW (the diffraction pattern in Figure 5-2c also shows a zone axis of <110>); this shows a tilt rotation of about 40° but, in contrast with Fig. 2a, there are few visible twins and a band exhibiting a darker contrast with the rest of the wire, which appears to be a result of increased dislocation density**.**

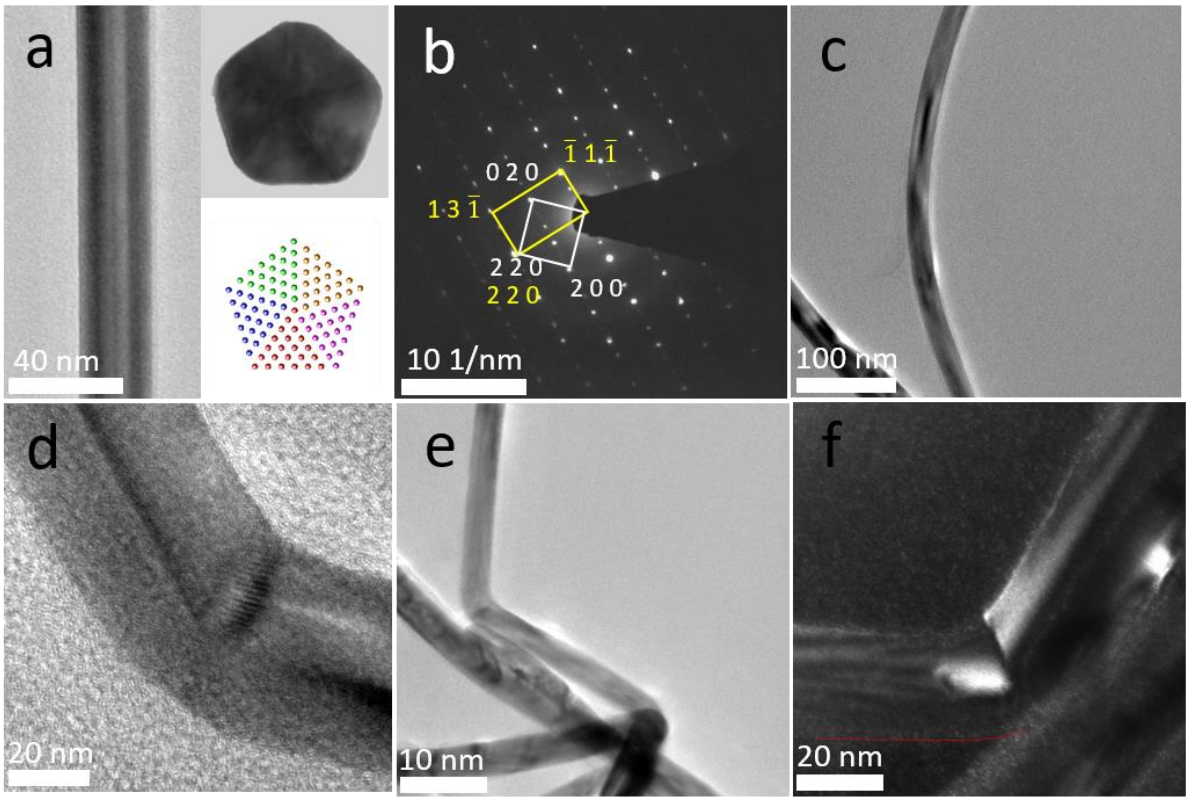

Figure 5-3 The structure of pentatwinned silver NWs and a series of images showing the in-situ bending test under TEM (a) High-magnification TEM image of the pentatwinned Ag NW with a diameter of 29 nm. The cross-section image is shown together with the lattice model (note the atomic structure is not to scale). (b) Indexed SADP of individual Ag NWs. (c) – (e) Series of TEM images showing the bending process of the individual pentatwinned silver nanowire. The deformation starts to become localized in (d) with the bending angle about 45 °. (f) Dark field images of the bent NW (bending angle is ~60 °), showing the shape of some sub-crystals in pentatwinned structure.

In contrast with the bending of single crystal NWs, the deformation of pentatwinned Ag NWs must be accommodated by processes in parallel in each of the five twinned sub-crystals. This is expected to constrain the deformation mechanisms and structures that form during bending. These have been monitored *in situ* in the TEM using the collodion film technique to load the NWs in compression and induce bending, with example structures shown in Figure 5-3. Figure 5-3a shows a bright field image of a pentatwinned Ag NW in longitudinal and transverse orientations prior to deformation. Polyvinylpyrrolidone (PVP) is used as a surface-capping agent during NW fabrication by the polyol process,[35] hence a transparent nanolayer can be seen on the surface of the Ag NW. The inset in Fig. 5-3a presents a cross-section of an

Ag NW with diameter ≈ 30 nm. The cross section is slightly rounded compared to the idealised prismatic structure also shown, presumably an effect of surface energy minimisation. A selected-area diffraction pattern (SADP) from the NW is displayed in Figure 5-3b. Diffraction patterns from two sub-crystals along [001] and $[1\bar{1}2]$ zone axes are indexed in the image. This indicates that the incident electron beam is normal to one prismatic plane surface of the pentatwinned structure[220] and the NW has grown along <110> direction. The second diffraction pattern showing the $[1\bar{1}2]$ axis is consistent with a 2π/5 (72°) rotation of the Σ3 twin between each sub-crystal. Figure 5-3c - 3e follow the deformation of a single pentatwinned Ag NW as it is deformed in bending following the shrinkage of the collodion film in the TEM. Figure 5-3c shows the NW initially deforming into a circular arc. As the bending angle increases to about 45^{o}, the deformation becomes localised into a small region (approximately 5-10 nm in width) that clearly undergoes some changes in the local crystallography as can be seen by the contrast change in Figure 5-3d. Afterwards, there is an abrupt boundary formed with a thickness of only a few nms extending across the full diameter of pentatwinned Ag NW as shown in Figure 5-3e, where the bending angle is approximately 60^{o}. The deformation structure has clear similarities to the behaviour of the deformed single crystal NWs shown in Figure 5-2. This behaviour, in which a region of high deformation recovering to a simpler structure, echoes the conventional ideas of recovery in deformed bulk materials but is also observed in deformed nanostructures[12].

Pentatwinned Ag NWs are of particular interest because they are formed by a simple solution growth process and thus are likely to be used for commercial applications of Ag NWs. However, the complexity of the atomic structure makes characterisation of the NWs more difficult, with usually more than one of the prisms overlapping along the electron beam path. This is seen in Figure 5-3b, where a SADP of the entire wire shows a range of different diffracted beams, which can be attributed to the different orientation of the segments within

the wire. Thus it can be difficult to interpret lattice images compared with other published research on single crystal NWs.[145,221,222] However, dark-field images can provide insight into the structure within a bent pentatwinned Ag NW; Figure 5-3f shows a dark-field image of a NW after the *in situ* bending process. This suggests that the sub-crystal prism segment under tension becomes narrower when approaching the location of the bend (a similar behaviour was seen in Figure 5-2a, while the sub-crystals under compression increase in apparent width. However the SADP from this region was very complex with the diffracted beams from each side of the bend (comparable to the SADP in Figure 5-3b present in the same pattern, this complexity can lead to diffracted beams from multiple regions of the sample being collected by the objective aperture, which explains the presence of bright regions across both sides of the abrupt interface in Figure 5-3f.

5.3.2 Scanning Nanobeam Diffraction Characterization.

The possibility that different regions of a complex (and strained) nanostructure are all scattering to the same point means that an individual dark-field image is often unsuitable for determination of the extent of any individual region within the pentaprism sample. Instead, the entire crystal structure of the sample needs to be considered to give an accurate means of determining the extent and arrangement of the different sub-crystal segments in the sample. This can be accessed through high spatial resolution scanning nanobeam diffraction, since this allows the local crystallography to be measured at 1-2 nm positions across the sample. Even with this resolution there will still be significant overlap of the different sub-crystals along the beam path, which can lead to a larger number of reflections and hence increased complexity in the diffraction patterns.

Machine learning approaches have been shown to be effective at partitioning such signals effectively, especially where precession electron diffraction is used to record the patterns

[16,174,223]. The machine learning method employed here is a blind source separation (BSS), where an algorithm attempts to find a set of representative signals (factors) that can be combined in varying amounts to accurate model the entirety of the experimental data [186]. The experimental diffraction data is usually highly redundant, that is there are far more experimental patterns recorded than there are unique (sub-)crystal structures/orientations present, even in relatively modest scan areas. Hence the algorithm can be compared to the numerical solution of a set of simultaneous equations where the individual experimental diffraction patterns are the 'equations' and the factors are the 'unknown variables'. Even if there is considerable overlap of the crystals along the electron beam path, the BSS allows the diffraction from the different crystals to be efficiently separated. BSS is performed typically on the reciprocal space dimensions of the experimental data, producing representative reciprocal space components or basis patterns that should represent the diffraction signals of the crystals in the sample. These are matched to complementary loading maps that highlight where in the scan that factor is significant, essentially acting like a dark-field image for the entire basis pattern.

However, given the high degree of coherency between the adjacent sub-crystals in the wire, it is expected that there will be many reflections that are common to more than one sub-crystal along the beam path. The commonly used approaches for decomposition (principal component analysis (PCA) or non-negative matrix factorisation (NMF)) are both susceptible to artefacts because the intensity of common reflections can be incorrectly partitioned between the representative factors [28]. In this situation it can be advantageous to decompose in the spatial domain. Here the decomposition factors and loadings are essentially reversed, with the factors being the most representative virtual dark field images (i.e., the intensity maps of the different pixels in the diffraction patterns) while the loadings are the pixels in the reciprocal space patterns that contribute strongly to produce that image. This is somewhat

less sensitive to the partitioning problem since the approach requires intensity from common reflections to exist in each loading 'pattern'. The absolute intensity may not be correct, but the overall pattern geometry should be faithfully recovered, and the presence of all reflections allows the orientation of the pattern associated with each factor to be determined.

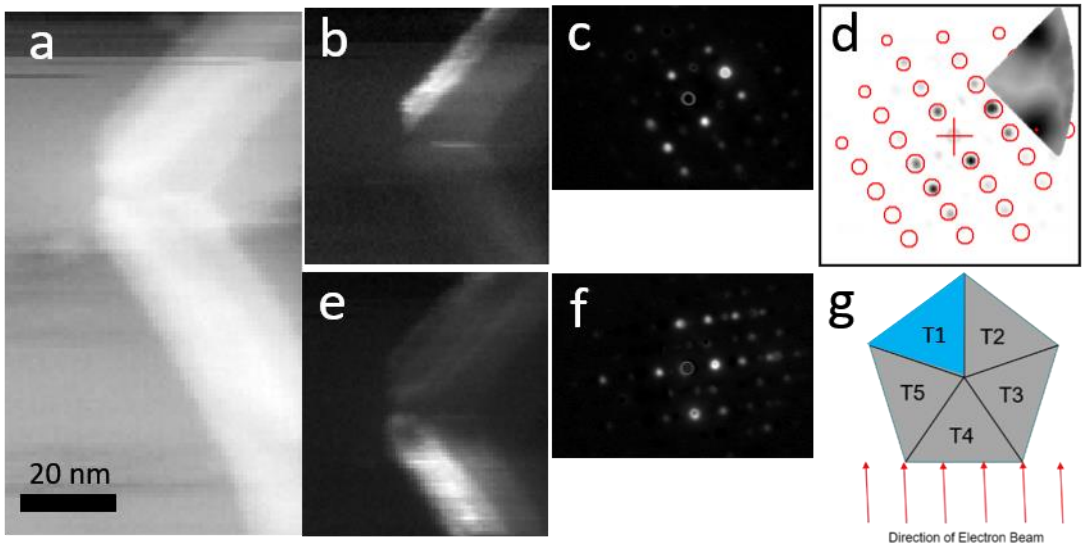

Figure 5-4 Structure characterization of bent pentatwinned Ag NWs. (a) The Virtual bright field image (VBF) of one bent pentatwinned Ag NW with bending angle about 70°. (b) The shape of the sub-crystal, and (c) the corresponding diffraction pattern. (d) is the indexation of (c) and the zone axis is <112>; the insert is the orientation of this pattern in the reduced stereogram. (e) The shape of the sub-crystal below the grain boundary, and (f) is its diffraction pattern. It has the same zone axis as (c): <112>. (g) Schematic illustration of the cross-section of the bent pentatwinned Ag nanowire and the incident electron beam. Both (b) and (e) are from region T1 (blue area).

Figure 5-4a shows a TEM image of a boundary in a pentatwinned Ag NW formed by bending. Scanning diffraction experiments were performed, and an example is shown in Figure 5-4b. The virtual bright field (VBF) image (Figure 5-4a) produced by mapping the intensity in a set of pixels around the direct beam position in each diffraction pattern in the scan. The wire appears brighter in this case because of saturation effects in the detector used to record the patterns, hence the increased background in the regions containing the sample cause the summed intensity to be higher than those regions comprising vacuum or support film. This image shows how the ~70° bend is localised into a very small region of the wire (with all of

the bending strain relaxed from the rest of the wire). The abrupt linear boundary within the wire is also visible.

Some of the results of a decomposition of the scanning precession electron diffraction (SPED) data from the bent Ag NW are shown in Figure 5-4b – 4f.Figure 5-4b shows the extent of the sub-crystal located at the outside of the bend in the upper region of the NW. Unlike the dark-field approach the decomposition has returned an almost unambiguous localisation of this sub-crystal and additionally recovers the complete diffraction pattern for this component which is shown in Figure 5-4c. This pattern was matched to a <112> diffraction pattern via an automated pattern matching method[224,225] as indicated in Figure 5-4d. Due to the coherence of the crystal structures (and hence the diffraction patterns) in the NW, patterns from different zone axes often exhibit intensity at the same positions in the patterns. The partition of intensity between the diffraction patterns from different subcrystals is imperfect and is sometimes not exactly the same as the simulated template. Although not all the spots can be well-indexed in experiments due to imperfect decomposition (as seen in Figure 5-4d), comparing the pattern with templates through cross-correlation provides a feasible solution for indexation of the loadings, thus improving the reliability of interpretation. The same decomposition method allows the extent of the subcrystals and their diffraction patterns in the lower part of the crystal (shown in Figure 5-4e and 4f respectively) to be recovered. This pattern could also be matched to a <112> zone axis but with a 70^{o} rotation, matching that of the overall bend in the wire. This suggests that this outer segment has undergone a simple in-plane bend with no rotation about the wire axis.

Analysis of the other decomposition results shows that the NW was oriented such that the electron beam travelled parallel to one of the prismatic Σ3 twins and perpendicular to one of the pentagon surfaces as indicated in Figure 5-4g. Each of the distinct sub-crystals in each section of the wire could be identified as having a <100>, <112> or <122> orientation

parallel to the electron beam, which matches the structure of the five twin-related prisms and in each case the 72^{o} in-plane rotation across the boundary was determined.

The decomposition results confirm the observation that the sub-crystals under greatest tension (indicated in Figure 5-4b and e) contract as they approach the boundary while those on the opposite side of the bend (under compression) widen slightly during the reorganisation of the material at the interface. However, to understand the geometry of the bend it is necessary to consider that the combination of the abrupt junction and the lack of 'twist' in the sub-crystals suggests that the new boundary is a symmetric twin boundary, albeit one that exists across the five different sub-crystals, each with its own unique orientation.

5.3.3 Geometrical Constraints on Deformation of Pentatwinned Nanowires

A symmetric twin can also be defined as a 180^{o} rotation boundary in the crystal, which is important because for two grains misoriented by a fixed angle around an axis, if there is a position where lattice point in one grain coincides with one in the other grain (called a coincidence site), owing to the periodicity of the two crystal lattices, there exists a coincidence site lattice (CSL). When the density of coincidence sites is large, we would expect the energy of the interface to be relatively low (at least compared to a random grain boundary) as the number of broken bonds across the boundary will be small.[226] The density of coincidence sites is described by Σ, defined as the ratio of the total number of lattice sites in the elementary cell of the CSL to the number of coincident sites in the elementary cell.

There exist a large number of CSLs associated with low Σ boundaries in FCC metals[227]. Hence it seems possible that there can exist certain 'magic' bending angles for specific bending axes that will result in a majority of the wire deforming by a set of cooperative twinning operations in the different sub-crystals.

The penta-twin structure comprises five parallel sub-crystals, with a common axis along <011>and an exposed face of {100}, with each crystal rotated 72° from its neighbour. The NW imaged in Figure 5-4 is oriented such that sub-crystal T4 is oriented with the electron beam parallel to <100>, i.e., normal to a prism face. Sub-crystals T3 and T5 are rotated +72° and -72° about the [011] direction from T4 and this corresponds to the electron beam along crystal directions close to [122] in the rotated sub-crystals. Note that the angle [122]:[100] = 70.5° and the discrepancy between this and 72° corresponds to the elastic strain that accommodates the pentatwinned structure. Sub-crystals T1 and T2 are rotated +144° and -144° and this corresponds to the electron beam close to the [211] crystal direction. These related sub-crystal orientations are confirmed by the decomposition factors from the sub-crystals and their indexation shown in Figure 5-5

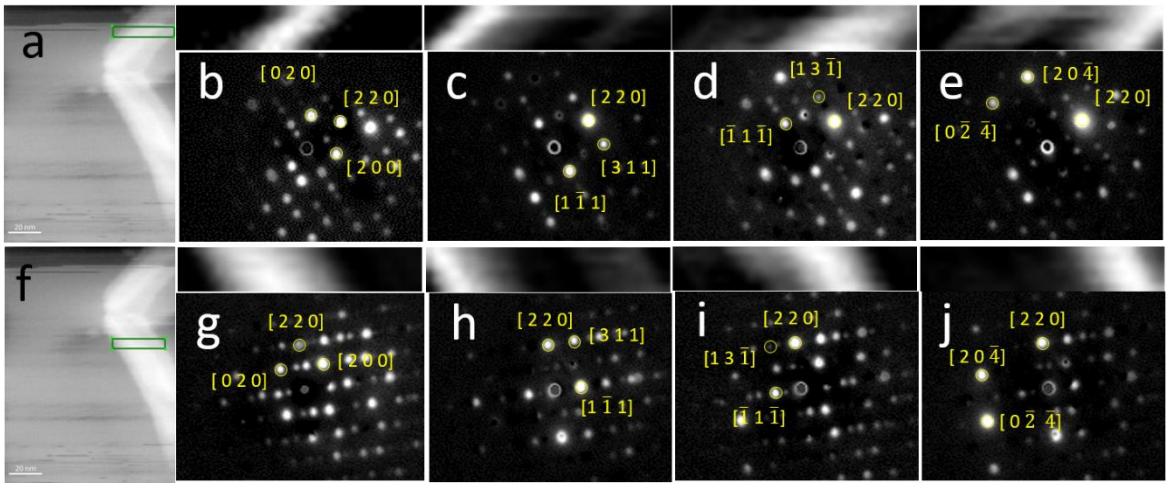

Figure 5-5 Sub-crystal orientations confirmed by the electron diffraction patterns from the sub-crystals and their indexation. (a) and (f) are the VBF images. Decomposition factors and loadings corresponding to the sub-crystals oriented along (b) <001>, (c) <112>, (d) <112> and (e) <221>. The corresponding parts below the grain boundary are also analysed, where (g) <001>, (h) <112>, (i) <112> and (j) <221>.

The CSLs for Σ up to 29 were found from the literature and in each case the symmetric tilt boundaries were determined. The possible coincident site lattices (CSL) for silver (face centred cubic structure) were determined using the rotation matrices provided by Grimmer *et*

al.[227] A CSL occurs for a given rotation axis (or crystal direction $[hkl]$) if the product of this direction vector and the rotation matrix returns an equivalent $< hkl >$ direction.

Further analysis of the allowed CSLs was performed to identify those that exhibited a rotation angle of 180º, since these are the boundary planes in the crystal structure that result in a symmetrical tilt boundary. The results of this analysis are summarised in table Table 5-1 below. Where a CSL is allowed for a given rotation direction the condition is marked with an 'x', those CSLs that are symmetrical tilt boundaries are indicated with a red 's'.

Table 5-1 Allowed coincident site lattices in fcc structured metals. For specific coincident site densities (indicated by Σ) if the lattice can be formed by a rotation about a specific axis, then the condition is marked by an '**x**', those conditions resulting in a 180° rotation boundary are

marked with an ‘s’.

Rotation Axis	Σ 3	5	7	9	11	13a	13b	15	17a	17b	19a	19b	21a	21b	23	25a	25b	27a	27b	29a	29b
1 0 0		x				x			x							x				x	
1 1 0	x			x	x					x	x							x			
1 1 1	x		x				x					x	x								
2 1 0	x	s	x	x				x						x	x				x		x
2 1 1	s	x	x		x			x						x			x				x
2 2 1		x		s			x			x							x				x
3 1 0		x	x		x		x				x				x						
3 1 1	x	x		x	s			x							x		x		x		
3 2 0			x		x	s				x		x									x
3 2 1	x	x	s	x		x	x	x			x	x	x	x	x			x	x		
3 2 2				x		x				s			x	x							
3 3 1		x	x		x					x	s				x		x				
3 3 2					x	x					x				x						x
4 1 0				x			x		s				x	x							
4 1 1				x	x				x			x						x	x		
4 2 1	x	x	x		x			x	x	x	x	x		s	x		x				
4 3 0							x			x						s	x				x
4 3 1	x	x	x	x			s	x	x				x	x		x			x		
4 3 2	x	x		x	x	x		x								x			x		s
4 3 3										x	x					x					
4 4 1									x					x							x
4 4 3														x		x					
5 1 0						x		x					x					x			
5 1 1			x	x		x					x							s	x		
5 2 0								x				x						x		x	
5 2 1	x	x			x	x	x	s		x					x					x	x
5 2 2										x				x						x	
5 3 0									s			x					x				
5 3 1	x	x	x	x	x	x	x	x	x	x		x		x				x	x		x
5 3 2	x		x	x		x			x			s		x	x				x	x	
5 3 3					x		x		x						x						
5 4 0													x				x				
5 4 1	x		x			x	x		x	x			x		x						x
5 4 3	x			x	x				x		x					x	s		x		
5 4 2		x	x	x											x			x	x	x	x
5 4 4																					x
5 5 1						x		x				x					x	x			
5 5 2																		x		x	
5 5 3								x	x				x					x			
5 5 4																					

For the wire described in Figure 5-4 the sub-crystals must have symmetric tilt boundaries that lie in the zones for <100>, <112> or <221> which reduces the possible number of CSLs considerably. From the list of possible CSLs for this bending axis, the boundary structures shown in Figure 5-6 were recovered. For the sub-crystal oriented parallel to <100> a Σ25a twin can result in {071} acting as a symmetric tilt boundary plane (this plane is indicated in

the upper part of Figure 5-6a. The angle between {110} and the appropriate {071} is 36.87°, resulting in a bend angle twice as large as this, 73.74°. The lower part of Figure 5-6a shows the resulting atomic structure where such a tilt boundary exists. Interestingly, when this bend angle is considered for the other sub-crystals, it becomes clear that the <112> oriented sub-crystals can achieve a similar deformation by the inclusion of a Σ15 boundary (where a {521} twin plane gives a bend angle of 78.40°) and the <122> oriented sub-crystals are deformed by a Σ25b twin (with {543} as the twin plane and a bend angle of 73.22°). These CSL boundary structures are shown in Figure 5-6b and 6c respectively.

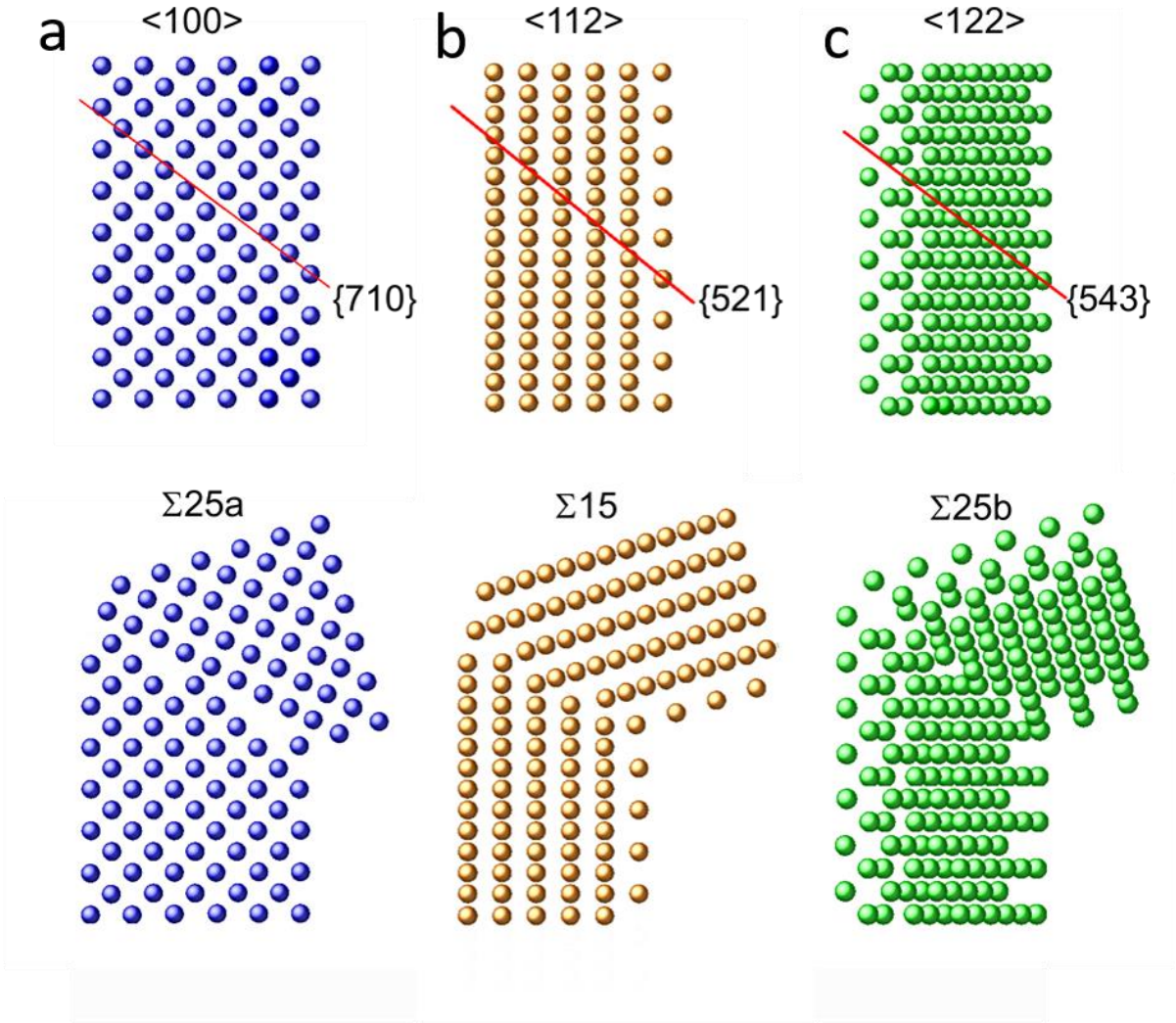

Figure 5-6 Lattice point distribution for silver crystals aligned to (a) <1 0 0>, (b) <1 1 2> and (c) <1 2 2>. The grain boundary planes are outlined using a CSL model when the NW

bending angle is 70°. For <1 0 0> segment, the plane is {7 1 0} Σ 25a. For <112> segment, the plane is {5 2 1} Σ 15. For <122> segment, the plane is {5 4 3} Σ 25b. Above figures are produced by CrystalMaker Software.

There is a small angular difference in the bend angles produced by these three types of twins. If we consider a perfect crystal interface, then small rotation angles between the two halves of the crystal can be as accommodated by an array of dislocations (the low angle tilt-boundary) that is again relatively low in energy compared to a random interface. Likewise, the well or cusp in surface energy terms associated with the low Σ twins can be relatively broad, as a small number of intrinsic secondary grain boundary dislocations can accommodate the angular difference while still resulting in an overall reduction in the energy of the interface compared to a random boundary. The depth of the well can be scaled approximately as $\Sigma^{-\frac{1}{2}}$ and its width described by the semi-empirical Brandon criterion of $15°\Sigma^{-\frac{1}{2}}$. [228]

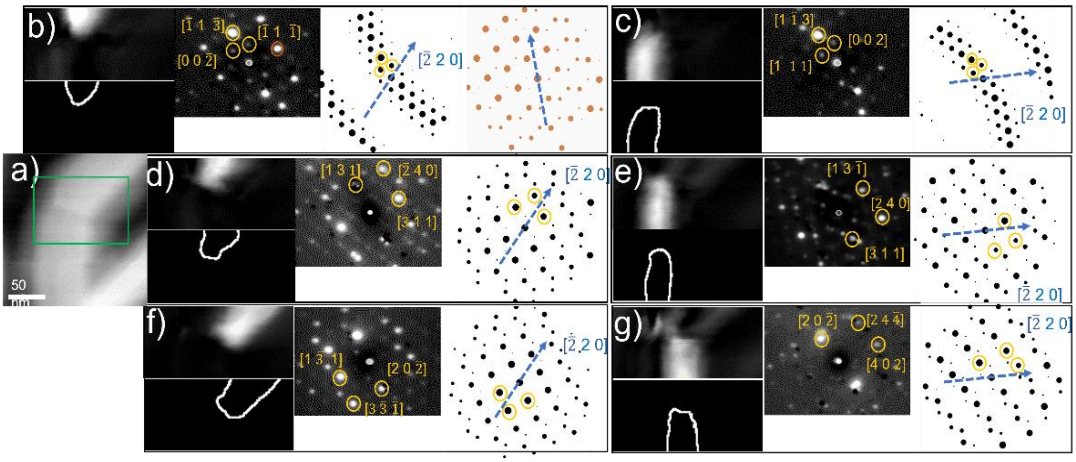

Figure 5-7 Decomposed SPED data from a bent pentatwinned NW and subsequent indexation analysis. (a) VBF images of bent Ag NWs. In the following each image, the VDF images and outline of the subcrystal are in the left, and the corresponding indexed diffraction patterns are in the middle. The matched templates and crystal growth direction (assumed to be [2$\bar{2}$ 0], blue arrows) are in the right. The pattern outlined by orange circle in (b) is indexed to belong to the patterns with zone axis of [2 4 9] (orange spots). (b), (d) and (f) show subcrystals above the bending boundaries and indexation returns that the subcrystals are oriented along <5 4 0> (6.3 ° to <1 1 0>), <2 1 5> (8.2 ° to <1 1 4>), <7 4 7> (13.2 ° to <1 1 1>). (c), (e) and (g) show subcrystals below the bending boundaries and indexation returns that the subcrystals

are oriented along <7 9 1> (8.7 º to <1 1 0>), <2 1 5> (8.2 º to <1 1 4>), <9 5 9> (13.8 º to <1 1 1>).

An identical analysis of another bent NW is shown in Figure 5-7, where Figure 5-7a is the VBF image of the wire indicating a bending angle of approximately 40 º. As described before, the cross-correlation compares the experimental pattern with all of the templates pixel by pixel before giving the solutions, so all the peaks in the patterns are considered in the indexation process. Besides this, the diffraction pattern indexation results should be consistent with the growth orientation of the NWs. These multiple criteria provide important guidance to choose the most possible indexation solutions. For example, when indexing the patterns shown in Figure 5-7b two solutions appears, where one shows that most of the patterns are indexed to belong to the template with the zone axis of <5 4 0> and the other shows that many patterns belong to the <2 4 9> template. Considering that the NWs growth direction should be consistent with other subcrystals, the second solution is exempted (the blue arrows are along with the [2 2 0] direction). A few additional bright spots may arise from the imperfect decomposition of the diffraction data.

The decomposition of SPED data across the bending interface indicates the bending axis was approximately 10º misoriented to one of the pentagon faces. This is thought to be a result of the uneven substrate possibly due to the existence of other wires (as seen in Figure 5-7a). As a result, the expected zones of the subcrystal are not <1 1 0>, <1 1 1> and <1 1 4> exactly but instead are rotated to be slightly away from these (typically to higher order zone axes e.g., <8 9 1> instead of <1 1 0>. In most cases the small misorientation means that most of the reflections in these patterns will also be present in the (nearby) <1 1 0>, <1 1 1> and <1 1 4> patterns, though the overall pattern will appear different as symmetry elements will be missing and some reflections may not be excited. Hence the diffraction signals (decomposition loadings) in Figure 5-7b, 5-7d and 5-7f, could be systematically indexed and the relative direction of the growth axis [$\bar{2}$ 2 0] is determined. The rotation of the [$\bar{2}$ 2 0] axis

representing the NW growth direction for subcrystals on two sides of the GBs is consistent with the bending angle of Ag NWs, approximately 40 ^{o}, which indicates that the above indexation should be reliable. In this analysis the two overlapping <2 1 5> oriented sub-crystals (close to <1 1 4>) are almost perfectly superimposed in the measurement meaning that they are returned as a single component by the decomposition, this seems likely given the relative sparsity of reflections in the <2 1 5> pattern compared to the other sub-crystal decomposition results for the corresponding sub-crystals on the other side of the boundary.

Even though the precession has been adopted to reduce the dynamical effect in this study, it may still exist and result in intensity discrepancies during the cross-correlation when comparing the experimental data with the templates produced from kinematical simulations. Therefore, minor misinterpretation of the diffraction patterns is found in experiments especially for the patterns given by the edge of the NWs (Figure 5-7 b, c, f and g), as the sample thickness changes sharply in these regions thus influences the intensity of the Bragg-diffracted beam in the reciprocal space. In addition, there is the possibility of interface strains at the numerous boundaries present in the vicinity of the bend. However, no rotation is observed for the subcrystal in the middle of NWs, where the patterns of corresponding subcrystals on two sides of the bend GBs matches well with the template for < 2 1 5>, which supports the assumption that no twist exists for other three subcrystals, as the deformation of all five subcrystals should be coordinated.

For this wire the bend is accommodated by a set of CSLs in the different sub-crystals as follows: in <110> the twin plane is {221} meaning the CSL is Σ5 (bending angle 36.7°) while for the sub-crystals that lie in <111> the twin plane is {321} meaning the CSL is Σ7 (bending angle 38.2°). For the <114> sub-crystals there is no low-Σ CSL that accommodates the ~ 40^{o} bend but the Σ49b CSL (twinning on the {941} plane) almost satisfies the angle and

axis conditions (within 2^{o} axially) but by twinning in this way, the entire wire can remain coherent. Hence, while this latter twin does not offer a significant energetic advantage in its own right, the fact that it allows very low-Σ CSLs to exist in the remaining sub-crystals helps to explain why this bend angle and interface occurs.

It is reasonable to expect there to be energetically favourable bending angles for the pentatwinned nanowires when the majority of the sub-crystals show orientations close to CSLs with low values of Σ. Figure 5-8 shows the bending angles for CSLs in different sub-crystals of the pentatwinned NW for 3 different bending axis directions. Where bending occurs around an axis normal to the {100} face of the sub-crystal T4 as illustrated in Figure 5-4. Figure 5-8a shows that there are no CSL orientations at tilt angles < 16° and that it is only above 40° that multiple sub-crystals show CSLs at common tilt angles (especially as the symmetry of the NW means that the blue and green points indicate CSLs that occur in two subcrystals simultaneously). This would be expected to represent the lowest energy interfaces for bending of the NW since the ordinate in the Figure shows the value of the energy metric ($\Sigma^{-\frac{1}{2}}$) for each CSL. Figure 5-8b shows the same analysis for a tilt-axis aligned parallel to the {100} facet of one of the sub-crystals again multiple CSLs at common angles do not occur below ~30^{o}. Figure 5-8c shows this analysis for a low symmetry bending axis (6^{o} from normal to the {100} sub-crystal facet). Here there are almost no CSLs with common angles and even where these occur they operate in only 2 of the 5 sub-crystals and so would be unlikely to provide a significant energetic advantage over other bending angles.

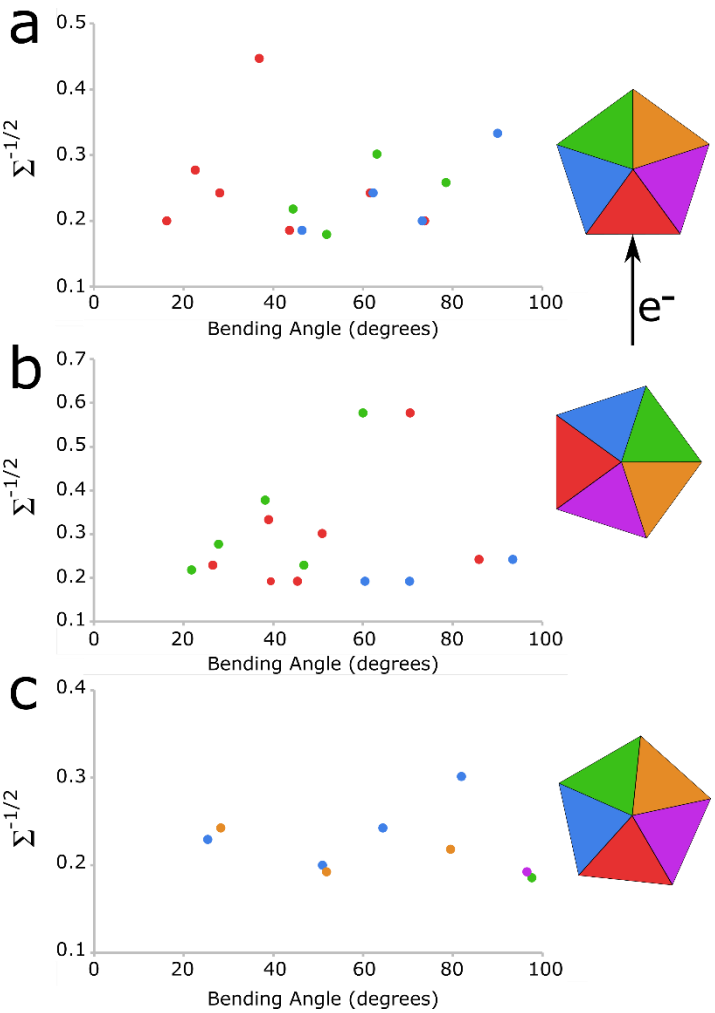

Figure 5-8 Different bending axes (the indicated electron beam direction is parallel to this bending axis). The colour of the point in the graph indicates which segment of the NW the CSL occurs in. (a) shows a NW with the bending axis normal to one of the {100} surface facets, note the symmetry of the NW means the CSLs will be the same in the green and orange segments, also the same in the blue and purple segments (only one set of points are shown for clarity). (b) shows a NW with the bending axis parallel to one of the {100} surface facets, the same segment symmetry occurs. (c) shows a NW with the bending axis aligned 6^{o} from normal to the {100} surface facet.

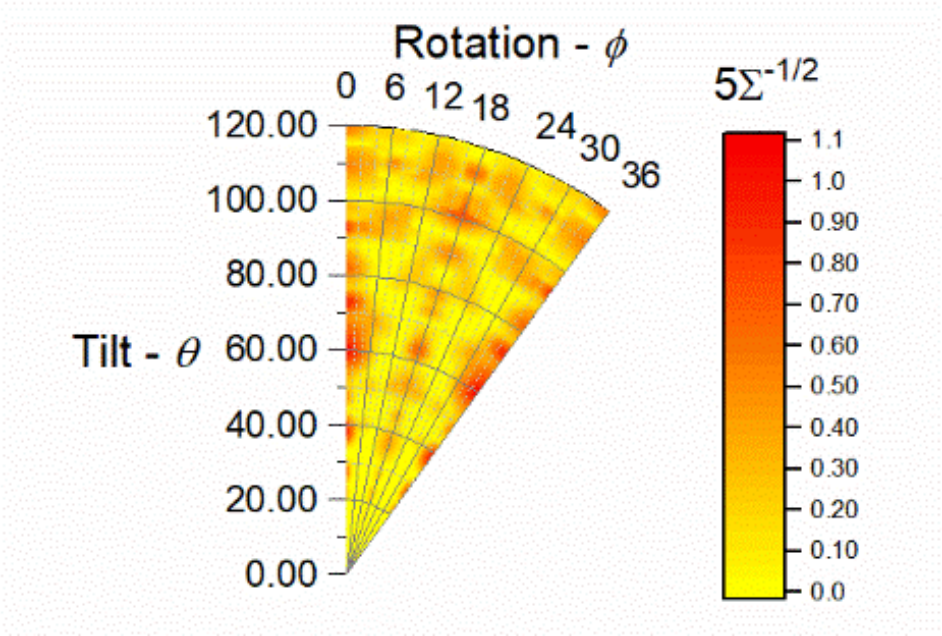

Figure 5-9 Illustration of Pentaprism orientation and low Σ CSLs associated with low energy tilt boundaries. Shading represents the sum of the CSL coincidence metric $\Sigma^{-1/2}$ of the 5 sub crystals (T1 – T5 in figure 4g) for a common bending (tilt) angle θ at a rotation ϕ from bending about the face of a prism {001}. Polar plot represents a total rotation of 36°, which is mirror symmetric about 18°, confirming that an 18° rotation (2π/20) captures all possible combinations of twist and tilt within the pentatwinned structure.

Given that the Brandon energy criterion allows the energy well around a CSL to deviate by a small amount in either tilt-angle or tilt-axis, a more general energy surface can be considered. By considering all possible CSLs with $\Sigma < 29$ (see table Table 5-1) it is possible to identify all rotations of the crystal from $0° < \Phi < 18°$ and to determine when there are CSLs with a common tilt angle, θ, in all of the sub-crystals T1 – T5. This is illustrated in Figure 5-9, which sums the metric $\Sigma^{-\frac{1}{2}}$ in each of the 5 sub-crystals as an approximate indicator of the total energy minimum associated with the CSL orientations. This confirms the low energies at selected tilts as indicated in Figure 5-8. It is clear that there is the greatest density of low CSL boundaries at similar tilt angles in multiple sub-crystals when the NW is oriented at 0° (which is a bending axis parallel to one of the sub-crystal {100} facets) with another favourable orientation, though with fewer common tilt angles, at 18° (a bending axis normal to one of the sub-crystal {100} facets). There are no CSLs of low energy at any NW

orientation for tilts < 25°. This plot indicates that the pentatwinned geometry allows a majority of low Σ CSLs to occur only along these two principal directions, parallel to, and normal to the pentagon faces. While there are CSLs that exist in the orientations of the crystal that lie between these limits, they are generally of higher Σ and so do not represent the most energetically favourable boundaries. The suggestion from this is that the majority of tilts will occur along one of these two directions, with bending axes up to 6 - 7^{o} away ultimately reordering into these more favourable end-states.

The other point of consideration is that for the single planar interface seen in the experimental data there need to be nearly parallel twin planes through each of the five sub-crystals. If we consider the two major bending directions in isolation (Figures 8a and 8b respectively) then a reasonable limit to the range of allowed bending in the system can be proposed. Below 25^{o} there are no multiply parallel CSL planes along either bending axis, at 40^{o} there are favourable bending geometries along both axes and this remains the case at intervals up to 90^{o}.

5.3.4 Quantitative Analysis of the Distribution of Bending Angles in Populations of Deformed NWs

To verify the above hypothesis on crystallographic constraints to deformation of penta-twined Ag NWs and to check the validity of the CSL model in explaining the behaviour of bent pentatwinned Ag NWs, the bending angles in individual NWs sampled from a large population were measured. A second sample of single crystal Ag NWs was also produced in the same way and the distribution of bending angles determined for comparison. In both cases > 300 NWs were measured. The results are shown in Figure 5-10. In Figure 5-10a, the relative frequency of the bending angles measured from the single crystal Ag NW samples is seen to show a modal value around 40° and follows an approximately log-normal distribution.

The distribution shape is consistent with the fact that a negative bending angle is not possible and that increasing bending angles require the generation of larger numbers of dislocations with a non-linear relation at large angles. Figure 5-10d shows the equivalent distribution observed for the bending angles measured from the pentatwinned NWs. This shows a number of distinctive differences when compared with the behaviour of the single crystal NWs. The bending angle distribution shows a cut-off with no angles < 16° recorded and a rapid reduction in the frequency of angles > 80°. The bending angle distribution in the range 20° < θ < 80° shows a bimodal distribution with peaks at θ ≈ 40° and a broader, less well-defined peak at θ ≈ 70°. Comparing the peaks in Figure 5-10b with the orientations with maximum $\Sigma^{-1/2}$ identified in Figure 5-9 shows that both the preferred bending angles observed with the Ag pentatwinned NWs coincide with peaks in the CSL model predictions.

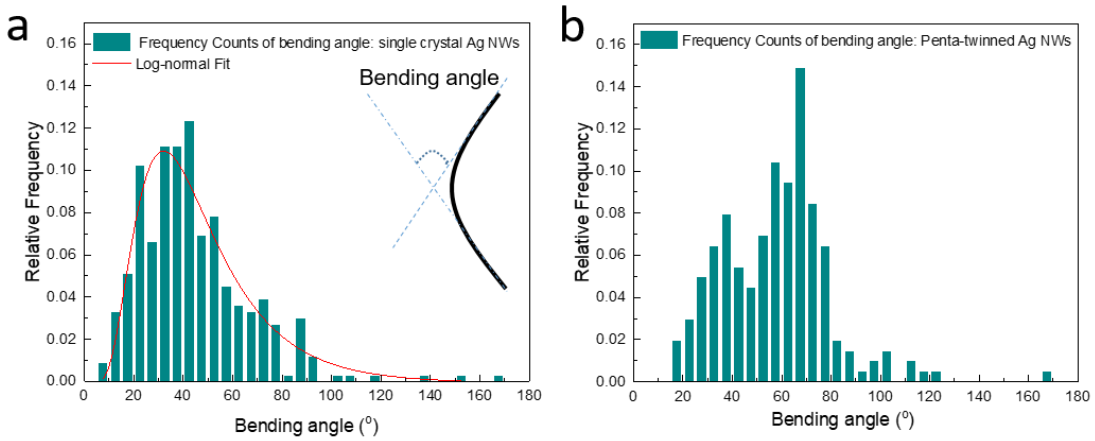

Figure 5-10 (a) Distribution of the bending angles measured from a population of 332 single crystal Ag NWs with the solid line showing the equivalent log-normal distribution. The inset shows the definition of the bending angle. (b) Distribution of the bending angles measured from a population of 370 pentatwinned Ag NWs.

5.4 Discussion

We have studied and compared the bending deformation of Ag nanowires that comprise a single crystal grown parallel to the <110> crystal direction with those formed via the polyol

process that also grow parallel to <110> but contain 5 parallel sub crystals interlinked by Σ3 twins on {111} planes. There are two major differences that are observed. First, single crystal Ag NWs show a continuous distribution of bending angles with a modal angular deviation (tilt, θ) of 40°, while the pentatwinned NWs show a bimodal distribution of bending angles with peaks at 40° and 70° and no NWs observed with θ< 16°, and fewer NWs with θ> 80°. Second, the single crystal NWs showed a range of deformation structures to accommodate the crystal rotation associated with the lattice rotation associated with the bend, including dislocation distributions and high angle grain boundaries, while the pentatwinned NWs showed clear sharp boundaries with few or no dislocations evident. Using scanning nanobeam diffraction and appropriate algorithmic decomposition procedures, it is possible to accurately determine the lattice rotation and boundary plane orientation in each of the five parallel sub-crystals of a pentatwinned Ag NW across the deformed region. We have used this technique to prepare a detailed characterisation of the relative orientation of each sub-crystal across the deformation zone in two pentatwinned NWs; in each case the rotation occurs across a sharply defined boundary region with a boundary plane close to a low Σ CSL boundary orientation. Finally, we have compared the frequency of the bending angle found in a large population of pentatwinned NWs and compared these with the tilt angles and NW orientations where there is a low Σ CSL boundary in the majority of the NW sub-crystals and found a strong correlation between the predicted lowest energy bending orientation and the modal values of the experimentally measured distribution of bending angles.

This brief summary of our findings indicates that our hypothesis that the presence of a number of low Σ CSL orientations in 3 or 4 of the sub-crystals presents a relatively low energy structure to accommodate the lattice rotation associated with Ag NW bend deformation. The presence of bent pentatwinned Ag NWs has been observed and commented on previously in the literature and describes as “v-shaped nanowires” of in the case of

multiple deformations “z-shaped nanowires.[193,229,230] Chen et al proposed that these v-shaped structures were formed by the adhesion of pairs of NWs. Jiang et al carried out a TEM investigation of the v-shaped wires and also found sharp interfaces and CSL orientations at the v-junction. They proposed that these structures either formed because of a crystal defects during growth or by the end-to-end fusion of adjacent NW. Although our results cannot eliminate the possibility of some of the bent nanowires resulting from growth defects or end-to-end joining, our examination of the bending of pentatwinned Ag NWs in situ using the TEM (Figure 5-3 and Figure 5-4) conclusively shows that high angle boundaries close to CSL orientations can form as a consequence of bending deformation.

5.5 Conclusions

The micromechanical behaviour of pentatwinned Ag nanowires under bending deformation has been studied using scanning nanobeam precession electron diffraction combined with machine learning approaches to determine the orientation and localisation of each of the sub-crystals in the wire. The deformation typically manifests itself as a rotation leading to a single planar boundary which has been identified as a low energy, high angle grain boundary across the whole wire that generates different coincident site lattices in the different sub-crystals of the wire. The geometrical constraint of finding CSLs in each of the sub-crystals severely limits the range of both bending axes and bending angles that can occur in the NWs even allowing for small elastic strains or deviations from the ideal CSL geometry.

The drive towards such behaviour seems to be the inability to activate conventional dislocation mediated slip in the small volumes that each sub-crystal represents and so the nanowires do not fail until a substantially higher stress (needed to reach the lowest angle multiple CSL condition) is reached. This high bending strength is suggested by highly curved NW seen prior to failure in the in-situ experiments. More importantly, a deformation

mechanism that maintains coherency along the wires suggests that the transport properties of the films can be retained even after an excessive compressive or bending load has been applied to the device.

6 Microstructure Evolutions of Pentatwinned Ag Nanowires in Networks under Fatigue Tests

6.1 Introduction

Technology developments in flexible electronics demand suitable flexible transparent electrodes, and the Ag NW is a competitive choice to replace traditional indium tin oxide (ITO) as the conductive component,[2,3] as the latter is brittle. Compared with other candidate materials like graphene, Ag NWs also provide an excellent balance between optical transparency and sheet resistance.[37] The standard polyol synthesizing process makes it possible to produce Ag NWs in bulk quantities at a relatively low cost.[32,231] The crystal structure of these Ag is typically pentatwinned and has been introduced in our previous research.[194] For the application of Ag NWs in reality, maintaining a low haze as well as keeping the electrical resistance low during high cyclic fatigue are important properties. The effective method to reduce haze is by adopting smaller diameter Ag NWs in order to minimise the scattering of light in the visible wavelength.[232,233] To increase the electrical reliability of Ag NW electrodes, junction welding and coating layers are widely applied in the reported research.[84,234–236] For example, Ag NWs networks with mechanically welded junctions show a negligible increase in resistance with a fatigue time of 500 cycles at 1% strain.[84] In order to further increase the reliability of these electrodes made by Ag NWs, understanding their failure mechanism under cyclic loading is necessary.

Currently, the majority of research is focused on the failure of welded junctions which form through mechanical sintering or thermal annealing.[152,237,238] The existence of grain boundaries at the welded junctions connecting two NWs with different crystal orientations would lead to stress concentration, so it is reasonable to suppose that the failures often occur near the junctions. In reality there are likely to be many unjoined junctions in the NW networks,[24] although the ratio of different junction types has not been confirmed. The presence of a significant population of unjoined junctions is likely, so researching failure modes associated with the main part of the ligaments of these NWs in networks is necessary.

The fatigue resistance of individual crystal NWs is believed to be better than bulk materials due to the reduction or absence of dislocation accumulation inside the wires during deformation.[74] For example extremely high fatigue resistance has been observed in ZnO NWs.[151] Comparing the fatigue resistance of Ag NWs with nanoscale Ag films also supports this theory, where the resistance of the former only increased 1.5 % while the resistance of Ag film increased 78%. [152] However, the fact that the metal NW networks resistance increases after fatigue cycling suggests that there some NWs undergo mechanical damage during fatigue.[83,153,154] Single crystal Ag NWs held under constant tensile strain show abrupt rupture due to stress-assisted diffusion,[239] but this loading condition is different from that expected under the operating conditions of NW networks, where cyclic loading would likely occur. Hwang et al.[24] conducted studies on the fatigue performance of Ag NW networks, which observed that NW network under cyclic compression undergoes buckling before failure in the middle of NWs due to strain localization, while the NW network under cyclic tension fails at the junctions. Other studies found that the NWs deformation mechanism is influenced by the density of the Ag NW networks, and that the bending strain can lead to a decrease in resistance caused by new junction formation for the less dense NW network in the early stage of bending.[154] Despite these initial explorations, there is still no

comprehensive understanding of the type and distribution of microstructure defects introduced to the Ag NWs within the networks under cyclic loading.

Transmission electron microscopy (TEM) is a powerful tool for observing the microstructure of NWs at very high resolution and can be used to characterise their internal crystal structure and defects. Given the difficulty in sample preparation, there are only limited published TEM characterization studies of the fatigue failure of Ag NW networks. [24,154] There is prior work using TEM to study the mechanisms of deformation of pentatwinned Ag NWs after tensile and bending tests.[100,194] Thus, there is an opportunity to explore the microscopic fatigue performance of individual Ag NWs in addition to the macroscopic properties of the network.

This chapter is based on a paper. Hu Zhao, Chongguang Liu, Alexander S. Eggeman and Brian Derby, 'Microstructure Evolutions of Pentatwinned Ag Nanowires in Networks under Fatigue Tests', in preparation. Hu Zhao conducted most of the experiments and prepared the first draft; the fatigue test equipment was prepared and operated by Chongguang liu, Alexander S. Eggeman and Brian Derby provided guidance and helped revise the draft.

6.2 Experiment method

Pentatwinned Ag NWs synthesised by the polyol process were acquired from commercial sources (NovaWire-Ag-A60, Novarials, Woburn MA, USA) with a mean diameter of approximately 60 nm. To support the NWs networks and to allow observation of the NWs under TEM before and after fatigue tests, a piece of porous polycarbonate (PC) film(pore size 8um, Millipore UK Limited, Watford, UK) was first covered by electron transparent collodion film (as described in the literature[194]), the thickness of which is approximately 200 nm to ensure that the film will not be damaged by the electron beam. Ag NWs were deposited on the PC/collodion substrates using an Infinity airbrush (Harder and Steenbeck, Norderstedt,

Germany), with a spray-head to substrate distance of 12cm. To promote electrical conductivity after spraying, a normal pressure of 29 MPa was applied for 15 s under ambient conditions using a laboratory hydraulic press. [240] This pressure treatment disrupts polymer surface films present from the polyol manufacturing process and forms conducting pressure welds between NWs. After application of the pressure the PC/collodion film containing the Ag NW network is approximately 10 μm in thickness. After fabrication, the sample was put into the TEM (Figure 6-1) to observe and characterise the Ag NW network before fatigue. Sample characterization before and after testing was conducted using a Tecnai TF30 (FEI, Eindhoven, Netherlands) and Talos F200A (Thermo Scientific, Eindhoven, Netherlands), operating at 300 kV and 200 kV separately. For scanning nanobeam electron diffraction experiments, Tecnai TF30 was controlled using a Nanomegas Digistar apparatus. The size of condenser aperture was 10μm corresponding to a convergence semi-angle of ~5 mrad, and the microscope spot size was 8, leading to a probe diameter of approximately 1 nm.

The fatigue experiments were carried out using an in-house designed and built testing rig (Figure 6-1).[22] The sprayed NW networks were first fixed onto a flexible polyethylene terephthalate (PET) film of thickness 100 μm using double sided tape and then mounted onto the belt of the testing rig, which was of thickness 340 μm. The flexible belt is driven forwards and backwards around a spindle of radius, R=4 mm, to generate repeated strain with a frequency of approximately 1 Hz. The maximum tensile strain acting on the NW networks is determined by assuming a simple elastic beam bending model, with:

$$\varepsilon = \frac{S + D + d}{2R + S + D + d} \times 100\% \qquad (6-1)$$

Where S is the belt thickness (340 um); D is the thickness of the PET film; d is the thickness of compressed PC/collodion substrate; and R is the radius of the spindle in the fatigue equipment. From this, the maximum strain applied on the NW networks is calculated to be about 5%. Networks were tested with up to 300,000 fatigue cycles of 0-5% strain. After cyclic bending, the sample was characterized under TEM. The pores in the PC film can be used as fiducial references to allow the same NWs to be identified and compared before and after testing.

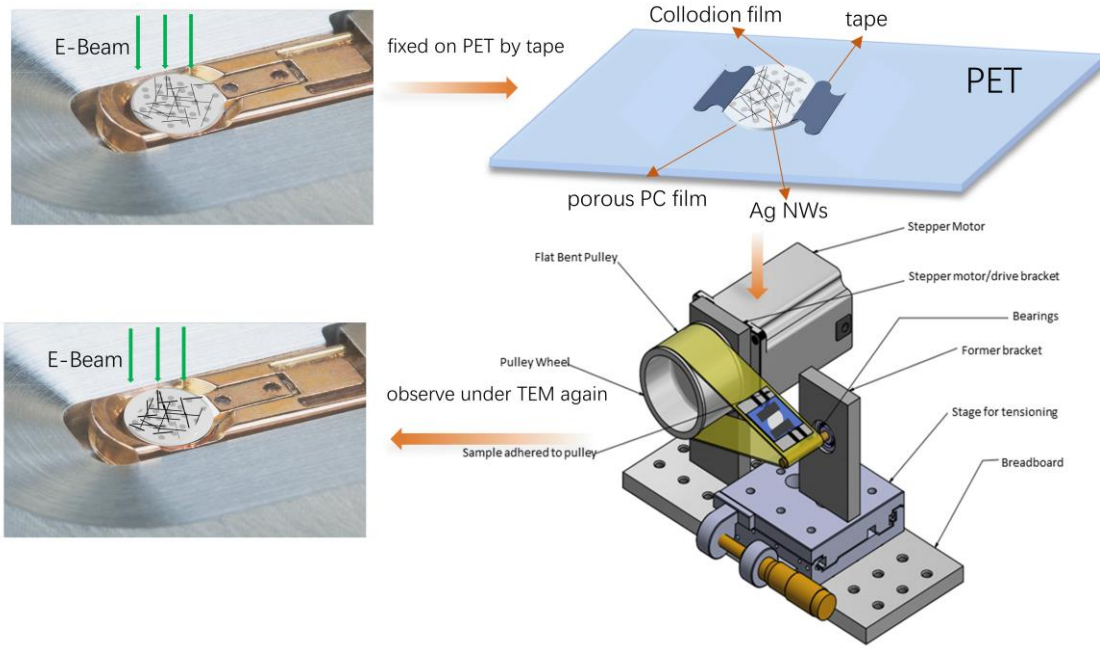

Figure 6-1Schematic of ex-situ fatigue experiments. The two-layer composite film with Ag NWs networks is observed under TEM before fatigue tests, then it is fixed on the PET substrate for cycle bending. The drawing of the test rig is shown here. After fatigue tests, the sample is characterized again in the same position.

6.3 Results and discussion

Fatigue behaviour of individual pentatwinned Ag NWs

The fatigue response of individual Ag NWs within the network is explored using bright field TEM images first. Figure 6-2 a-d shows the structure of the NWs before and after 50k fatigue

cycles. It is observed in Figure 6-2a and b that there is a NW section (indicted in yellow) that is subjected to compressive stress during cycling and becomes highly bent. The wire segment does not seem to be welded to the wire it crosses in this region so the network can accommodate the local plastic strain during deformation. Our previous research indicates that this bending structure can be highly coherent, [194] so the conductivity of the wire may be still very high. However, the fact that the resistance of Ag NW networks increases after cyclic loading indicates that there is widespread failure of the network and/or the individual NWs during fatigue.[153] It is believed that the bent NWs will be fractured under further cyclic loading. This assumption is supported by Figure 6-2c and (d), where an initially bent NW (circled) appears to be fractured. Being bent first then fractured under cyclic loading is thought to be one of the Ag NWs fracture modes leading to the electrical resistance of the networks increasing.

Additionally, some wires fracture under cyclic tension directly (Figure 6-2e and f). These NW networks were extracted from PET substrate directly without using porous PC films. The network is formed by applying a normal pressure so that the NWs which cross over each other is welded together to form conducting junctions. It appears that the fracture points are close to the junctions (Figure 6-2e). Necking of the pentatwinned Ag NWs is observed in the dashed circles, suggesting a ductile fracture mode. TEM studies of individual single crystal Ag NWs indicate that the NWs will rupture abruptly after extended cyclical tension as the failure can be driven by stress-assisted surface diffusion due to the reduction of elastic energy.[241] In this study, the fatigue tests can result in the cyclic extension of the Ag NW networks sputtered on the outside surface of PET substrate during bending, so surface diffusion may also exist for these wires, generating the necking and subsequent ductile fracture of the NWs. Those NWs that are not welded with others possibly fail at the junction due to strain localization (Figure 6-2f).

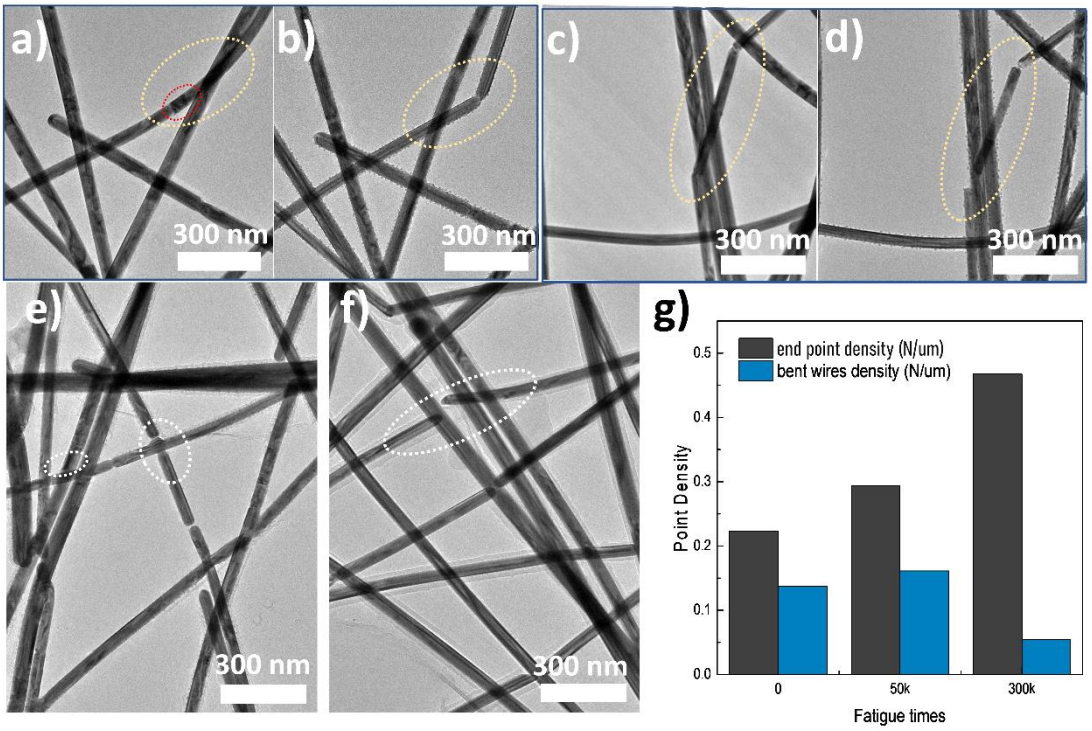

Figure 6-2 TEM images of Ag NWs before and after 50 k fatigue times under 5% strain. (a) and (b) shows that the wires are bent after fatigue. (c) and (d) indicates that one bent wire fractured after fatigue. NWs failure under tension is presented in (e) with welded junctions and (f) without welded junctions. (g) is the histogram of end point density and bent wires density as a function of different fatigue times.

In previous work it was shown that the sheet resistance of a Ag NW network can be modelled as a product of the network coverage (the proportion of surface area covered by nanowires) and the network resistance. The network resistance R_n was derived as[22,212]

$$R_n = K(r_w + r_j)\left(\frac{\omega}{\lambda}\right)^2 \qquad (6-2)$$

where K is a constant; r_w and r_j are the wire resistance and junction resistance respectively; λ is the average length of a NW and ω is its diameter. After cyclic fatigue it has been demonstrated previously that the sheet resistance of NW networks decreases with the increasing number of strain cycles but that the resistance remains proportional to the network coverage. [22] This has been interpreted in indicating that it is the change in R_n that describes the damage to the network during fatigue.[22]

On inspecting equation 6-2 we can see that there are three components to the model for network resistance that might change during fatigue cycling. The wire resistance, r_w, the junction resistance, r_j, and the mean length of the nanowires. During the fatigue, we assume that the resistance of the junction and the wires remain constant and that the dominant mechanism for the increase in resistance is the fracture of the NWs, which will lead to a decrease in λ. Therefore, the resistance change of the NWs network is mainly dependent on the square value of the NW length. Through TEM image analysis, the average densities of NW end points and bent NWs are calculated based on 10 TEM images with field of view of 2.5*2.5 μm for each sample(Figure 6-2g). The units of point density are number/um. When the fatigue time is 50 k, the point density increased from 0.22 to 0.29, indicating that the average length of the Ag NWs decreases from 9.0 μm to 6.8 um. Introducing this value to Eq. 6-2, the network resistance should increase 1.74 times after fatigue of 50k cycles. In the experiment, the resistance of Ag network (mean coverage 0.09) increased from 18 mΩ/□ to 28 mΩ/□ when the fatigue increased to 50 k cycles under 5% strain,[242] 1.56 times higher than the resistance of NW networks before fatigue tests, which is lower to our calculated value based on point density. This calculation method was also applied to the samples with 300 k fatigue cycles, and all the results are listed in Table 6-1. Higher resistance changing rate based on end point density calculation compared with actual resistance changing rate may indiacte that some other factors need to be considered when predicting the resistance of nanowire networks. For example, the fracture of some NWs may not change the NW network resistance too much as the model predicted, as there are some alternative paths/NWs carrying the mobile electrons, just like parallel circuits. These results provide valuable insight on the failure mechanisms of Ag NWs networks. However, predicting the inaccuracy of equation 6-2 in calculating the resistance of NW networks is not conclusive here, as only 10 TEM

images with field of view of 2.5*2.5 μm for each sample are analysed in this research due to the difficulty in the sample preparations.

Table 6-1 Measured resistances of Ag NW networks with fatigue times increasing and calculated resistance on NW length changes as a function of fatigue times.

Sample name	R_{nx}34 (mΩ/□)	Point density(/um)	Actual R_{nx}/R_{n1}	R_{n1}/R_{n0} based on end point density
0-R_{n1}	18	0.22	1.00	1.00
50k-R_{n2}	28	0.29	1.56	1.74
300k-R_{n3}	41	0.47	2.28	4.56

In addition to the fracture-point density, the bending structure density is also listed in Figure 6-2g. It shows that this value initially increases before dropping to 0.051 /um. The cycling loading could introduce more bend structures, as shown in Figure 6-2a and b, while further fatigue deformation could promote failure at these bend points. It is worth considering that the obvious reduction of NWs average length under 300 k fatigue times also make it more difficult to form bending structure (as described in chapter 5), so the formation of many new bending structures is unlikely under high fatigue times.

Microstructure of observed "bamboo" faults.

After exploring the failure mode of the individual NWs in the network, to further understand the deformation behaviour of Ag NWs in networks under fatigue loading, the internal structural changes within the pentatwinned Ag NWs were characterized under TEM. Previous research on compression testing has shown that the small diameter of NWs makes it easy for dislocations to escape from the surface.[65,74] Here we have investigated pentatwinned Ag NWs tested after fatigue and found few dislocations in the structure, as shown in Figure 6-3 a and b. However, these ex-situ TEM images show some high contrast bands are present along the

nanowire after cyclic loading, which has never been observed in the tensile tests of pentatwinned Ag NWs.[11,13] The small extent of the bands and their relatively large spacing leads to a bamboo-like effect along the NW. Using traditional TEM techniques (like bright field image and selected area diffraction) the bamboo defects within the pentatwinned Ag NWs are hard to analyse because of the overlapped subcrystals under the electron beam and the small spatial dimensions of the individual defects.

Here scanning nanobeam diffraction methods followed by machine learning decomposition were adopted to characterize the crystal structure of a bamboo fault. The details of this technique can be seen in our previous research.[16,194] Briefly, the NWs are scanned using a nanosized quasi-parallel electron beam in diffraction mode, and the formed electron DPs are recorded in every position simultaneously, forming a 4-D data set composed of a 2D field of view and 2D electron diffraction patterns pixel by pixel. In order to reduce dynamical effects as well as obtaining more diffracted beams, a precession angle of 0.5^{o} was applied to the beam.[15] As there is always more than one subcrystal along the incident electron beam trajectory, the obtained diffraction patterns contain overlapping information from the different crystal orientations. Therefore, a machine-learning method (non-negative matrix factorization [NMF]) was used to decompose the diffraction patterns of each subcrystal from the obtained 4D-data. Different from the recent observation that most bamboo faults move and disappeared during TEM imaging,[243] the bamboo faults formed after fatigue tests remain stable under the scanning electron beam in this study.

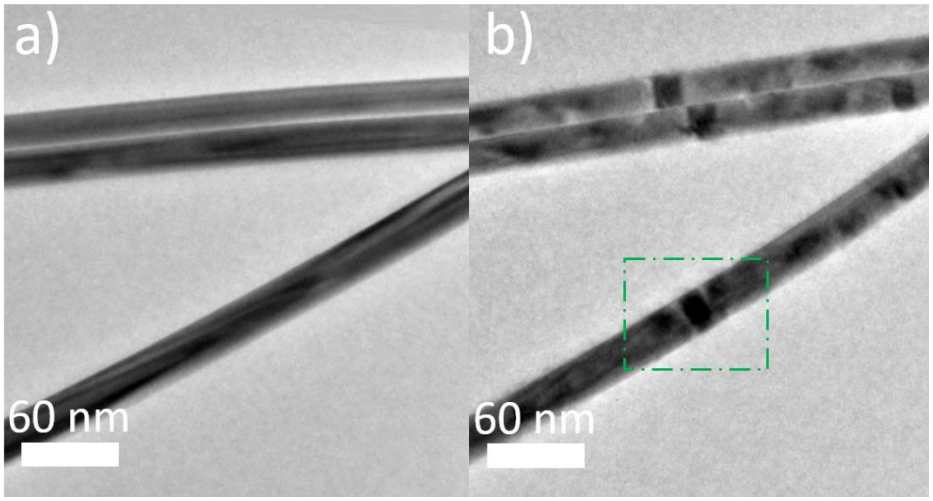

Figure 6-3 Imaging of bamboo faults after fatigue tests (a) Ag NWs in networks before fatigue tests and (b) after fatigue tests.

Crystal structure analysis results of the green-labelled area in Figure 6-3b are presented in Figure 6-4. The data is decomposed using the methods mentioned above, which returned three distinct regions in the 'upper' part of the pentatwinned Ag NW (Figure 6-4a). Indexation of the loadings (which contain the diffraction pattern information relating to those regions) shows that the patterns from the main part of the wire are a close match to the diffraction expected along <8 1 9> (close to <101> Figure 6-4c and d). In these cases, the reflection positions for the <819> zone axis are indicated by red overlay spots, and almost all the spots are well indexed using this template. The orientation of all the patterns is also consistent, which are indicated by the purple arrows along [2 0 2], further verifying the reliability of the indexation.

The loading for the third region corresponding to the bamboo fault was more complicated, and the template matching results indicate the there are two possible solutions for the decomposed signal with a high correlation score, as shown in the indexation map in Figure 6-4b. One solution is the diffraction patterns with a zone axis of <1 0 1>, while there are still many spots that have not been indexed, which are labelled yellow in the Figure 6-4b. Guided by the orientation indexation map, it is found that the above unindexed signals could be

matched well to a <1 1 5 > direction. The reflection positions for <1 1 5> are shown by the blue circles in the right corner of Figure 6-4b, with some reflections in the similar/same positions with the reflections from <8 1 9> axes (in red circles). Other solutions may also include part of the unindexed patterns, while the correlation index (Q) of them is not as high as the <1 1 5> solution. There is also another possibility that the unindexed diffraction patterns in Figure 6-4b are stimulated from multiple zone axes not only <1 1 5>. However, the decomposition results do not suggest any other crystals close to this region, so this possibility could also be excluded based on current analysis methods.

The accurate orientation results are indicated by the Euler's angle in the indexation software, which are (38.5, 137.0, 262.3) for the patterns shown in Figure 6-4b and (42.0, 136.5, 264.0) in Figure 6-4c, while both are given a Miller index of $[\bar{8}\,\bar{1}\,\bar{9}]$ due to the limited precision of the software. It is possible that a higher Miller index may better describe these patterns but these are not returned by the software being used.

Patterns from a zone axis of <8 1 9> will have many common features with patterns from a zone axis of <1 0 1>, as there is only a small misorientation (5.8 degrees) between the two. The patterns from equivalent systems (like [8 1 9], $[8\,\bar{1}\,9]$ and $[\bar{8}\,\bar{1}\,\bar{9}]$) can be reached through different inclinations of the crystal, resulting in very similar patterns but different orientations of asymmetric Laue circles. Therefore, there is a possibility that the software cannot distinguish the patterns simulated from equivalent systems well when noise exists in the data, leading to some misallocations. This may explain the different shapes of the patterns observed in Figures 6-4 c and d, as the minor errors from the imperfect decomposition may make the indexation results look different although they belong to the equivalent systems. On the other hand, there are also some other possibilities that the crystal may have rotated by slightly different amounts but where the software limitations prevent finer separation of the orientations.

Here the <8 1 9> reflections may come from imperfect decomposition. Given the partially coherent crystal relationship between the subcrystals we would expect many common reflections in the different subcrystal diffraction patterns. Patterns from the <1 1 5> zone axis exhibit many of the same reflections as the patterns from the <1 0 1> zone axis and imperfect partition of the intensity between these common features does occur when using NMF. However, the fact that reflections associated with the <1 1 5> zone axis do not appear in the adjacent crystals, such as crystals shown in Figure 6-4a and d, implies that in these regions, the decomposition was able to correctly partition the signals and hence suggests a distinct change (rotation) of the NW orientation in the defect.

The slight differences in the diffraction patterns shown in Figure 6-4c and d suggests that there seems to be a small strain in the crystal outside the defect, in addition to the large-scale change in crystal rotation that occurs within it. Another possibility is that the crystals on either side of the bamboo faults may also have minor deformations due to the existence of deformation defects (e.g. dislocations) in the middle or at the interfaces, which results in the rotation of the diffractions shown in Figure 6-4c and d. It is worth noting that this deformation should be not obvious as the zone axis and direction of the pattern (based on the NW growth direction analysis) for crystals on two side of the bamboo faults is still consistent.

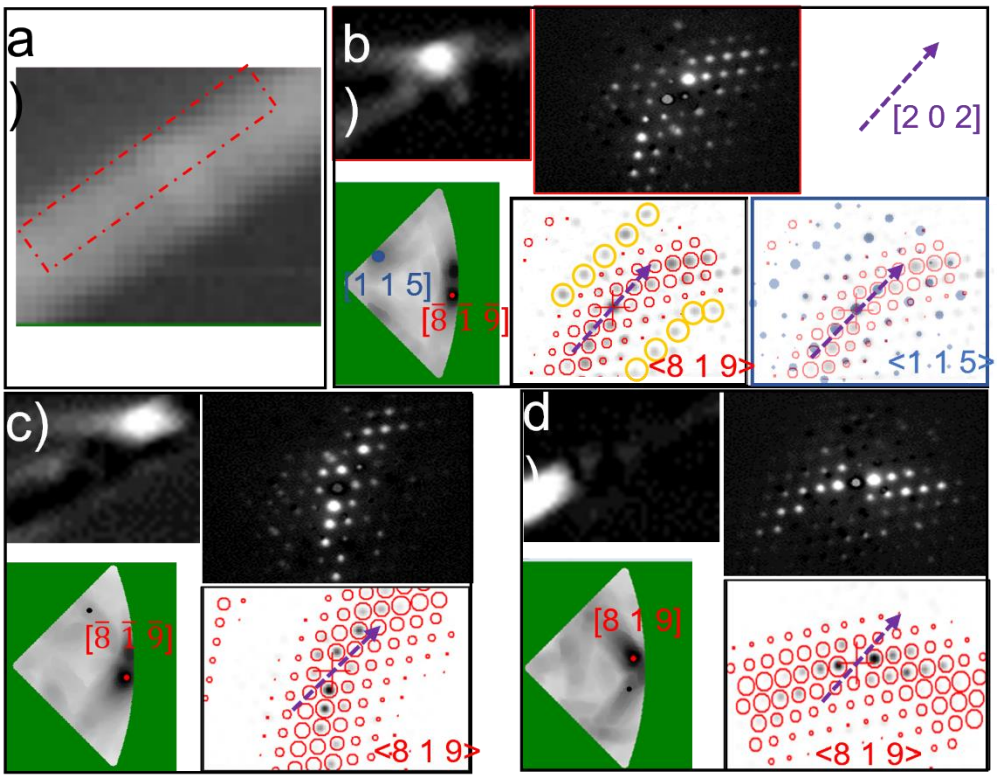

Figure 6-4 Bamboo structure characterization and crystal orientation indexation results. (a)shown VBF images of Ag NW and the decomposition of one subcrystal (in red rectangular) returns three segments divided by the bamboo faults. (b) The shape of the bamboo structure in the sub-crystal, and the corresponding diffraction pattern. The indexation results show that the signals from both zone axis < 1 1 5 > and <8 1 9> are found. (c) and (d) is the subcrysals on both side of the bamboo fault, and indexation results shows that the zone axes are <$\bar{8}$ $\bar{1}$ $\bar{9}$> and <8 1 9> correspondingly.

Formation of the bamboo faults

As there are five subcrystals along the growth direction in each Ag NW, the formation of a fault across the NW during fatigue tests should be achieved through a coordinated deformation of all five subcrystals to form a relatively low energy atomic arrangement. A similar co-ordinated deformation during the bending of Ag NWs has been inferred from our previous work and discussed in Chapter 5.[6] Based on the experimentally observed crystal rotation in some subcrystals (Figure 6-4), a possible mechanism describing the formation of the bamboo faults is presented.

The result that the zone axis of one subcrystal is indexed to be close to <1 1 0> suggests that the orientations all subcrystals in the wire are close to <1 1 0>, <1 1 1> and <1 1 4>, based on the pentatwinned structure of this Ag NWs. Therefore, one of the surface facets of the above NW should be parallel to the electron beam direction, as shown in Figure 6-5 a. For the subcrystal with orientation <1 1 0>, the crystal rotation prefers to go to <1 1 4> forming a Σ3 grain boundary with the adjacent unrotated crystal. This is illustrated in Figure 6-5b. Hence, it seems that, in the faulted region, the red coloured sub-crystal has undergone plastic deformation transforming it locally to the orientation of the green sub-crystal as shown in Figure 6-5c. This is consistent with the experimental observations that subcrystals with the orientation in <1 1 5> (close to the <1 1 4> direction) is observed in the <1 1 0> orientated subcrystals.

Since there is no visible change in the morphology of the wire, we can surmise that all of the sub-crystals have been subjected to near-identical stress and so should have also deformed by adopting the orientation of the adjacent sub-crystal in the faulted region. This structure is shown in Figure 6-5d. Such ‘cooperative’ twinning processes have been predicted and reported in our previous studies,[194] and result in a small dislocation density and hence a small stored plastic strain energy.

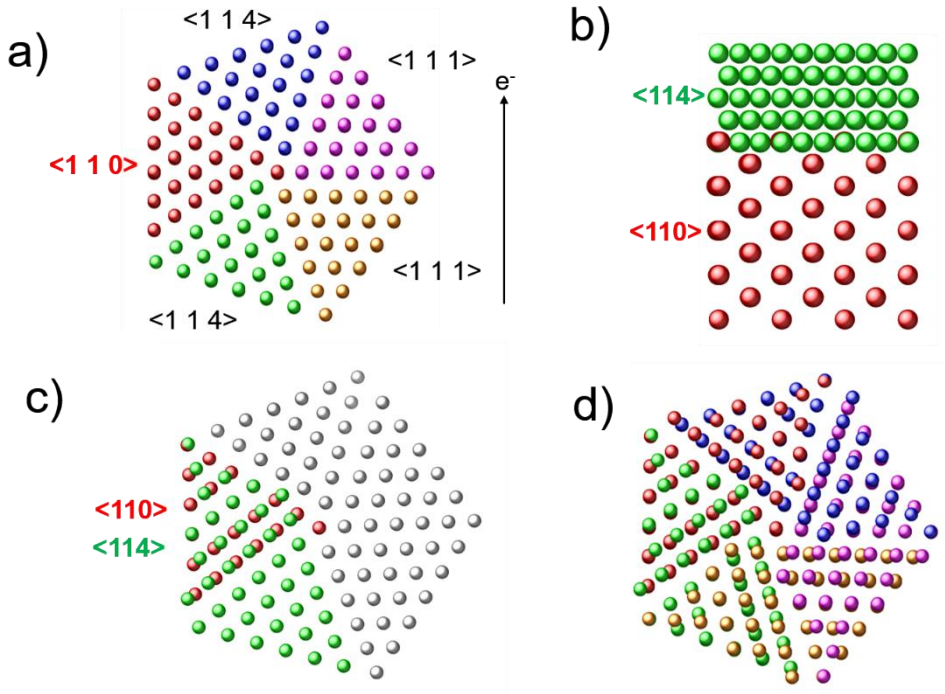

Figure 6-5 Structure analysis of the bamboo faults. (a) the schematic structure of the pentatwinned NW with the approximate orientations of the sub-crystals for the electron-beam trajectory indicated. (b) and (c) show the <1 1 0> oriented subcrystals viewed along the electron beam trajectory and the wire axis respectively, transforming the red crystal orientation to the green crystal orientation explains the measured disorientation. Continuing this approach produces a complete stacking fault across the NW as shown in (d). The above figures are produced by CrystalMaker Software.

The Σ3 twist boundary is one of the lowest energy twist boundaries in the (1 1 0) plane when the crystal is rotated along <1 1 0> axis according to coincidence site lattice theory,[226] while this cannot exempt the possibilities that other (1 1 0) twist boundary may also exist in <1 1 0> orientated subcrystal when the NWs are deformed. Wei et al.[244] calculated all the value of Σ when the materials are twisted along the <1 1 0> axis, and the plots of which are seen in Figure 6-6.

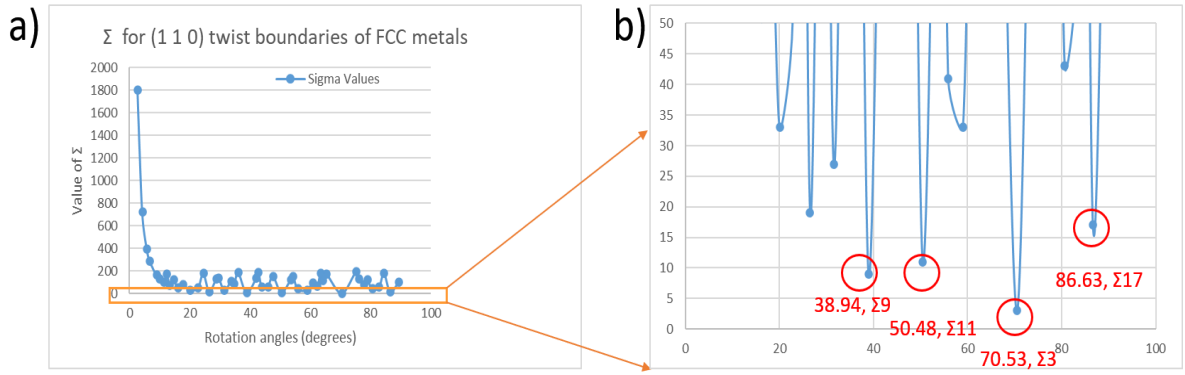

Figure 6-6 Plot of the Σ value for the FCC metals twisted along the <1 1 0> axis. (a) is the value of Σ as a function of rotation angles ranging from 0 to 90 degrees. (b) is the magnification of (a), which shows the several low Σ and corresponding rotation angles.

Several low Σ twist boundaries (< 20) and corresponding rotation angles are shown in Figure 6-6b. Assuming that these boundaries exist in <1 1 0> orientated subcrystals in pentatwinned Ag NWs, as shown in red in Figure 6-5a, the orientations of all five subcrystals after the appropriate twist deformations are calculated and shown in the 6-2 correspondingly.

6-2 Low Σ (1 1 0) twist boundaries and orientations of each subcrystal in pentatwinned NWs after these boundaries are formed in [1 -1 0] orientated subcrystal.

	Orientations of each sub-crystal in pentatwinned Ag NWs				
before twist	[1 -1 0]	[-1 1 4]	[-1 1 1]	[1 -1 1]	[1 -1 4]
Σ3, 70.53°	[1 -1 4]	[-4 4 5]	[1 -1 1]	[-1 1 5]	[-4 4 5]
Σ9, 38.94°	[4 -4 5]	[-5 5 4]	[-1 1 0]	[-1 1 5]	[-1 1 4]
Σ11, 50.48°	[3 -3 5]	[-2 2 1]	[-5 5 2]	[0 0 1]	[-2 2 5]
Σ17, 86.63°	[0 0 1]	[-5 5 2]	[-3 3 -5]	[-2 2 5]	[-5 5 3]
Σ19, 26.53°	[3 -3 2]	[-3 3 4]	[-5 5 1]	[2 -2 5]	[0 0 1]

Another bamboo fault is characterized using the same method as stated above, which shows a different twist boundary as predicted in table 6-2. The image of this bamboo fault is shown in Figure 6-7a. Decomposing the signals from the area in the green rectangle also returns to three different components divided by the boundary of the bamboo fault for the subcrystal on

the left (Figure 6-7a). For the region of wire outside the bamboo fault, the orientation of the decomposition factor can be indexed to be <9 1 9> and <8 1 9> correspondingly (closed to <1 0 1>), as shown in Figure 6-7b-1 and b-2. Therefore, the crystal orientation of each subcrystal relative to the incident electron beam is deduced and presented in Figure 6-7b-3 and shows a small ~6^{o} rotation of the wire from the ideal <1 1 0>/<1 1 4>/<1 1 1> orientation. The diffraction signal from the region of the fault is presented in Figure 6-7c, where multiple solutions appear.

As with the previous analysis there appears to be a diffraction signal within the faulted region from an axis close to <1 1 0>. However given the limitations of the data it is difficult or impossible to determine if this is the same <9 1 9> axis diffraction signal seen in the unfaulted wire or of this is comes from a slightly differently oriented subcrystal (such as the <2 2 1> orientation seen in table 6-2, though given the small deviation from the perfect wire alignment this would be actually closer to <4 4 1>).

As with the previous analysis this may not be fully unmixed because of the small number of measurements covering their strongly overlapping region. The reflections in the faulted region not associated with the <9 9 1> crystal orientation (in yellow circles) are indexed and most probably correspond to <3 3 7> through template matching. The smallest angle between the <3 3 7 > axis and the <9 1 9> axis is 27.1 ^{o}. This is the disorientation value returned by the ACOM crystal analysis software, where above disorientation is smallest possible rotation angle out of all symmetrically equivalent misorientations. However considering all possible misorientations between <3 3 7> and <9 9 1> this angle could also be 54.3 ^{o} (<3 $\bar{3}$ 7> and <9 $\bar{9}$ 1>), which closely matches the rotation needed for a Σ11 twist boundary described in table 6-2, this boundary also generates the <2 2 1> oriented subcrystal mentioned previously. The small differences in the indexed zone axis compared with table 6-2 should be from the different orientation of NWs under electron beam and shape uniformity of different

subcrystals in the NWs. The top view of deformed lattice resulting from the coordinated deformation of all five subcrystals is presented in Figure 6-7d, where the indicates in the grey rectangular are the axes of deformed subcrystals in the bamboo faults without considering the tilt of NWs under an electron beam.

Based on the model constructed in Figure 6-7d, the electron DPs recorded from one region of the bamboo fault (Figure 6-7c) may present as the sum of two DPs due to imperfect decompositions. Figure 6-7e presents a kinematical simulation of the diffraction from the above two overlapped crystal, <3 3 7> (closed to <3 3 5>) and <10 10 3> (closed to <2 2 1>). This is overlain on the decomposition factor from the subcrystal in the bamboo faults shown in Figure 6-7c. This seems to explain all of the reflection positions seen and helps to explain why there are inconsistencies when a <9 9 1> indexation is attempted. For example the four {1 1 1} reflections are much weaker than the rows of reflections running through the {2 2 0} reflections and the direct beam when they should be the strongest reflections in the patterns. Since these reflections are from different subcrystals the intensity discrepancy can be explained.

It is now possible to explain the observed diffraction signal both directly from the decomposition analysis as well as from the structural model of the pentatwinned NW.

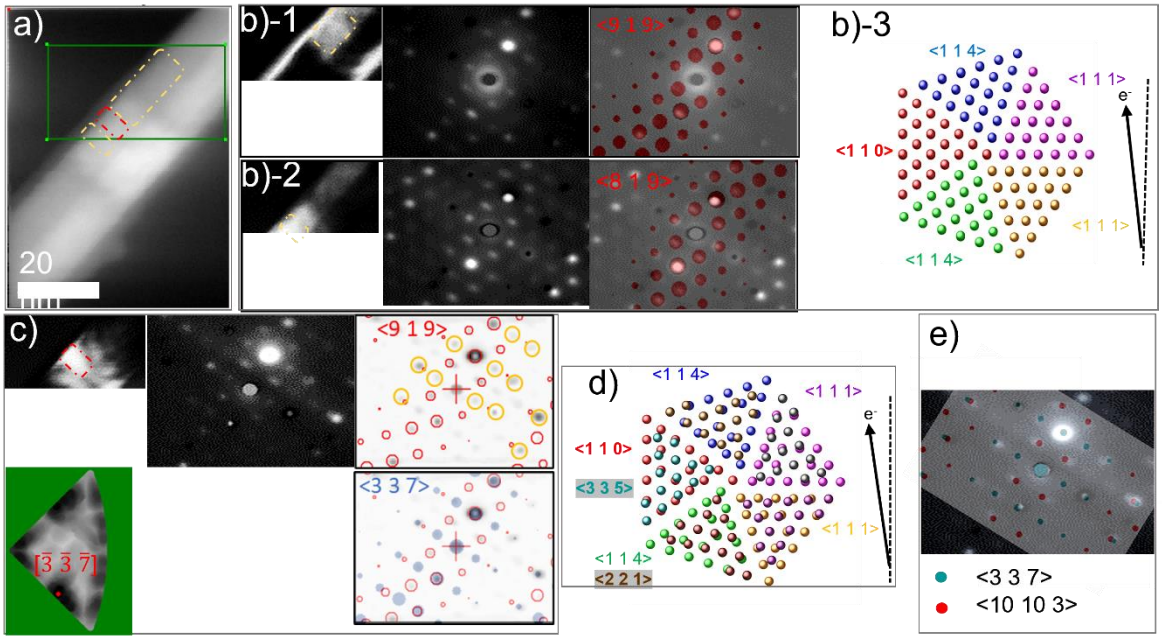

Figure 6-7 Bamboo faults and their crystal structure characterization. (a)The analysed area (green rectangular) of the NWs and segments that the decomposition returns in one subcrystal. (b)-1 and (b)-2 is the subcrystals on both sides of bamboo fault, and indexation results show that the zone axes of are <9 1 9> and <8 1 9>, (b)-3 the crystal orientation of each subcrystal relative to the incident electron beam. (c) The shape of the bamboo structure in the sub-crystal, and the corresponding diffraction pattern. The indexation results show that the zone axis is <$\bar{3}$ $\bar{3}$ $\bar{7}$> with extra signals from <9 1 9> axis; (d) The top view of the bamboo faults with Σ11 boundaries after a coordinated deformation occurs in all five subcrystals.(e) simulated diffraction patterns from the zone axes of <3 3 7> and <10 10 3>, which match well with the experimental data obtained from the bamboo fault region (c).

The above results suggest that the bamboo faults represent a rotation of the NW structure around its long axis, and the twist boundary is normal to the NW growth direction <1 1 0>. As such the partial dislocations that give rise to it must have a Burger's vector normal to the wire axis. It is recognised that twist boundaries are observed after the deformation of bulk materials, e.g. in polycrystalline aluminium after rolling deformation,[245] because of inhomogeneous deformation. However, the deformation of this one dimensional NW,[246] is subject to a much simpler set of stresses. Within a network of nanowires, the only constraints are where the wires are bonded at junctions. Bamboo faults are seen along the full length of the NWs, some distance from the junction. Here, from St. Venant's principle the local stress state can be approximated to a one dimensional state with only tensile and twisting stresses along the fibre axis.[247] There has been molecular dynamics simulations of the deformation of

Ag NWs in both tension and torsion. Models of tension loading predict deformation through edge dislocations propagating along the {1 1 1} planes inclined at 54° to the <1 1 0> axis, forming a characteristic pyramidal deformation structure.[13] Models where torsion loading is applied predict the formation of screw dislocations, either parallel to the <1 1 0> direction, where the torsion is accommodated by an "Eshelby twist" or in the case of inhomogeneous deformation by a series of screw dislocations on different slip planes.[248]

An explanation for the presence of torsion force comes from studies of stress distributions in similar, but larger diameter, fibre networks. As early as 1961, Ranger and Hopkins [249] noted that fibre bonds in paper could fail either by shear or by 'peeling' (torsion) and more recently Bergstrom et al. [250] show how the fibre-fibre bonds of the 3-D fibre network in free space are mostly twisted under a certain fibre density range. The suggestion here is that the increased network density leads to an increased proportion of torsional stresses in the network under loading, primarily because of the constraints introduced by junctions between fibres.

In order to accommodate rotation in the {1 1 0} plane normal to the growth direction it is necessary to have a series of screw dislocations with Burger's vectors within the plane of rotation. Three possible in-plane partial and perfect screw dislocations, with their Burgers' vectors are shown in Figure 6-8a. Note that two of the partial dislocations are also present in the {1 1 1} plane that act as the Σ3 boundaries between the crystals. These bamboo faults have never been previously reported with previous TEM studies of the tensile deformation of Ag NWs,[251,252] thus we believe that they only form in the presence of torsional loads such as can be generated during fibre network deformation. [249, 250]

Hence, even though the Ag NWs are attached to the PET substrate in our samples, the relative softness of the substrate means that a macroscopic tensile stress applied to the network can result in microscopic torsional forces being generated, particularly near the

welded junctions. This hypothesis is supported by comparing the bamboo density under different NW coverages all subjected to 50 k loading cycles with strain 5%) (Figure 6-8b). The density of the bamboo structures in the network (ρ) is calculated from the number of faults counted in a set of TEM images (n) using equation 6-3.

$$\rho = \frac{0.06n}{A * C} \qquad (6-3)$$

Where A is the area that each of TEM images (2.8 um*2.8 μm in this study) contains and C is the NW coverage in the TEM images, which is counted through a self-writing programme. The units are the number of the bamboo structure per μm length of NWs (the average diameter of the wires is 60 nm). Denser networks mean that the junction density is higher, as the NWs has more possibilities to overlap with each other. Each of the histogram represents the average bamboo density calculated from 12 images. The error bar the error bar shows the estimate of the variance obtained from the samples. It shows that the bamboo structure density increases monotonically as the NWs coverage ratio increase from 0.111- to 0.213. Above SPED characterization shows that the bamboo faults are coherent, connecting with other parts through low Σ twist boundaries, so it is not expected that it will contribute significant resistance to the Ag NW network, while these defects could be dislocation nucleation sites when the NWs fracture due to stress concentrations.

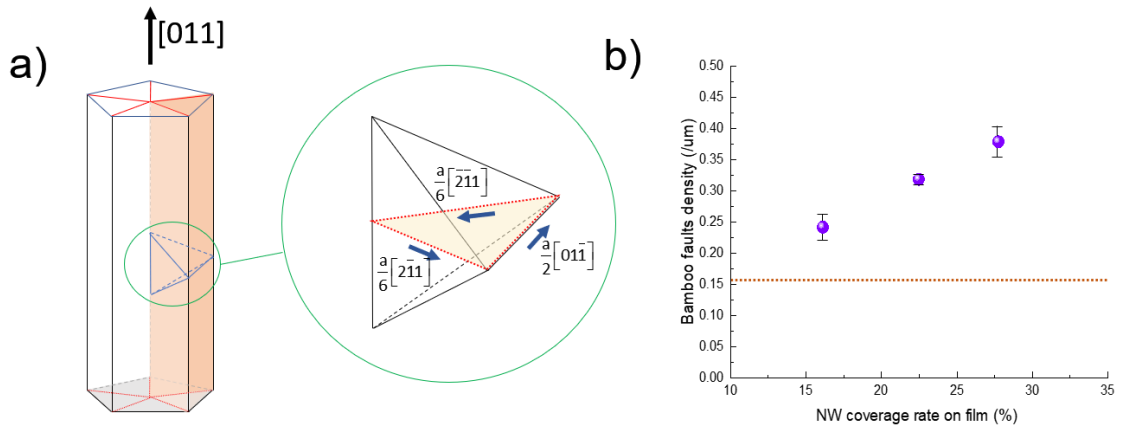

Figure 6-8 Formation mechanisms of bamboo faults (a) Schematic of the three possible in-plane screw dislocation Burgers vectors that can act together to generate a lattice rotation in the {0 1 1} plane for pentatwinned Ag NWs deformed under torsion. The Burgers vectors are drawn on a schematic Thompson tetrahedron showing the orientation of the slip systems within a subcrystal. (b) Bamboo faults density changes as a function of the Ag NWs coverage rate on polymer film (equal to NW junction density). The dashed orange line is the average bamboo structure density from the samples without fatigue tests, and other samples are tested with fatigue times being 50k

Changes in bamboo fault density

A further study of the change in bamboo fault density during fatigue testing was attempted. Using the same approach as the data in Figure 6-2 (and using Eq. 6-3) the change in bamboo fault density for a range of different fatigue cycle numbers was performed and the data is shown in Figure 6-9a. The data of each bar is based on 12 images with a view area of 2.8 um*2.8 um, and the error bar shows the estimate of the variance obtained from the samples. Before the fatigue tests, the bamboo structure density was in the range of 0.11-0.16 /um, while after fatigue testing, the bamboo density increased with increasing fatigue cycle number, before reducing to 0.19 /um, although there are considerable errors in these estimates given the relatively small sample sizes. One hypothetical explanation for the data is that when fatigue times are below 150 k, the cycling bending of PET substrate promotes the existence of bamboo faults, as suggested by Figure 6-3aand b. At higher numbers of cycles, the increased likelihood of failure of the network (both junction failure and wire fracture) could lead to local stress relaxation within the wires. This assumption is supported by further

detailed characterization in Figure 6-9b, c. In the white circle, it is obvious that the bamboo structure that exist before fatigue vanished when the wires fractured near the junction. The similar behaviour is also found in Figure 6-2a and b, where the bamboo structure disappeared when the wire is bent. This interesting observation indicates that the bamboo structure could be recoverable, which may be similar to the recovery of dislocations seen after uniaxial stress relaxation in Qin's work.[11]

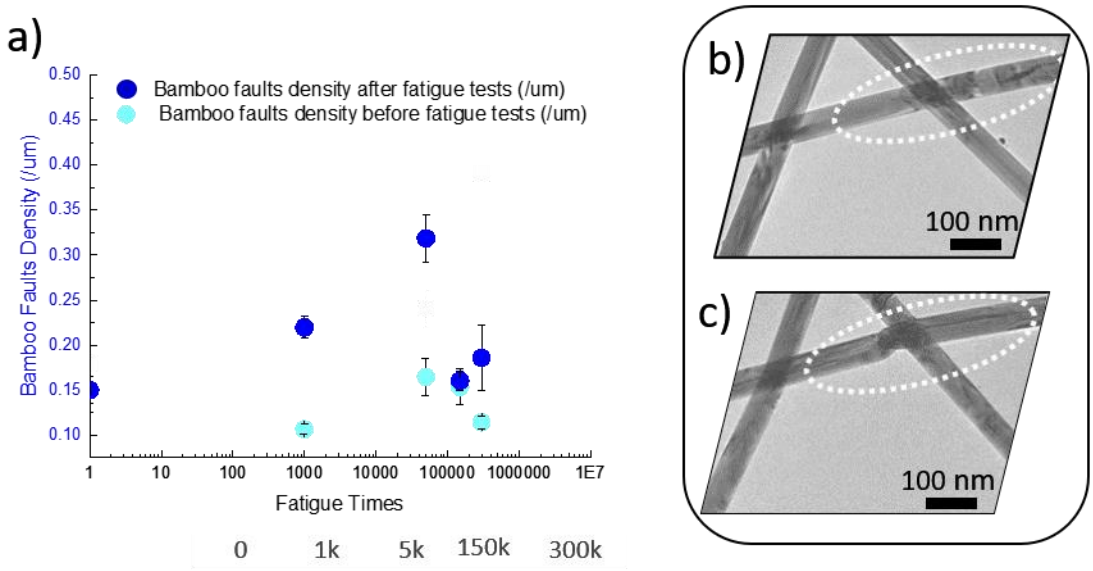

Figure 6-9 Bamboo faults density changes with fatigue times increasing. (a) is the bamboo structure density as a function of fatigue times. (b) shows that the bamboo faults are released after the NWs fracturing.

The apparent removal of bamboo faults from the network is supported by a free-energy argument. Since the composition and structure within the bamboo faults is the same with parent Ag NWs, and only a twinning interface is introduced when bamboo faults forming, the total energy change (E_{bulk}) in the system is the value changes of interface twin boundaries energy, E_{surf}. E_{bulk} and E_{surf} are expressed as:

$$E_{bulk} = \pi r^2 * t * \Delta G_{twin} \qquad (6-4)$$

$$E_{surf} = 2 * \pi r^2 * \gamma \qquad (6-5)$$

Where r and t are the radius (30 nm) and length of bamboo defaults respectively; ΔG_{twin} is the free-energy change in bamboo faults per unit volume and γ is the surface energy of twin boundary per unit area, which is 11 mJ m^{-2}.[253] As $E_{bulk}=E_{surf}$, the value of ΔG_{twin} is given by:

$$\Delta G_{twin} = \frac{2\gamma}{t} \qquad (6-6)$$

This suggests that ΔG_{twin} is about $2.2*10^6$ Jm^{-3}. Considering that the heat of fusion for the Ag is about $(923*10^6)$ Jm^{-3}, the increased energy in the bamboo faults (ΔG_{twin}) compared with the pristine crystal is relatively high. On the other hand, since there are only several low Σ grain boundaries existing for the rotated crystal in {1 1 0} plane, when the NWs are deformed under torsion, the intermediate deformed structure with high Σ value (high energy states) may exist under applied forces. In this case, the surface energy γ in equation 6-6 should be higher compared with TBs, leading to higher energy states of the bamboo faults. This large driving force for reversal combined with the relatively small separation of the twin boundaries (and hence the ease of reordering the atomic structure) may explain the reversible behaviour of bamboo faults observed in our experiments.

6.4 Conclusion

This study explored the failure behaviours and microstructure evolutions of Ag NW networks are studied under TEM. Based on the new sample preparation methods, the NWs deformation process and the microstructure changes of pentatwinned Ag NWs in network under high cyclic loading can be observed. The Ag NWs fail through being bent first or fracturing under tension directly. Quantitative analyse shows that the NW ends density increases with cyclic loading, and the calculated network resistance changing rates based on mathematic model proposed before are higher than the actual networks resistance changing rate observed in experiment. Further characterize into the inner structure of pentatwinned Ag NWs shows that

bamboo faults appear after fatigue tests, the crystal structure of which is characterized using SPED follows by signal decompositions. Lattice coherent rotation model is proposed here, and the torsional forces is thought to be related to the NW junction when tensile stress is applied in the network. It is believed that most of these faults will not increase the electrical resistance of the NW networks to a large scale due to the high coherence of twist boundaries, but they could be the dislocation nucleation sites leading to the fracture of NWs. Bamboo faults density vanished in some wires indicating that they may be reversible, which is believed to result from the high energy states of the faults.

The study here reveals failure modes of Ag NWs in networks and give a useful guidance to microstructure changes of NWs applied in flexible electrodes. The exploration on the fatigue performances of pentatwinned Ag NWs, like the bamboo defaults, may stimulate further interest to explore the unique fatigue performances of metal NWs in networks.

7 Conclusions and future work

7.1 Conclusions

This thesis set out to study the mechanical responses of Ag NWs and explore their underlying mechanisms. The influence of the pentatwin structure, characteristics of polyol synthesis, and sample size on the mechanical behaviours of Ag NWs were explored in detail. As the mechanical responses of Ag NWs and the underlying mechanisms are influenced by different deformation modes, the NWs are tested under tension, bending and fatigue loading, separately.

Tensile tests were conducted *in situ* inside a SEM using a nanoindenter equipped with a push to pull loading stage. The UTS values from 25 pentatwinned Ag NWs and 5 single crystal Ag NWs, with a diameter ranging from 70 to 320 nm show that the strengths of single crystal and

pentatwinned Ag NWs are similar and their behaviour follows the well-established empirical size effect of FCC metals with the power law exponent being about -0.66 ± 0.1. Due to the small diameter of these NWs, after the NWs deformed under tension, most dislocations escape from the surface leading to few dislocations observed in these NWs. Stacking faults are observed at a 54° angle to the NW growth direction (angle between <1 1 0> and {1 1 1}) and these indicate the passage of partial dislocations along the {1 1 1} planes. The TBs in the pentatwinned Ag NWs act as a barrier to dislocation motion, so the stacking faults arrest in the middle of these NWs, while in single crystal Ag NWs the stacking faults are observed to pass through the whole width of the sample. The barrier effect of the TBs reduces the dislocation interaction possibilities during the deformation process, so strain hardening is not obvious in most pentatwinned Ag NWs but is observed in the single crystal Ag NWs.

When the Ag NWs are deformed under bending, the presence of TBs results in a different deformation behaviour between the pentatwinned and single crystal Ag NWs. In particular, the deformed pentatwinned NWs showed a number of characteristic bending angles after deformation, with peaks at 40° and 70° and no NWs observed with $\theta < 16°$, and fewer NWs with $\theta > 80°$. In contrast, the distribution of bending angles in the single crystal NWs approximated to a log-normal distribution. Subsequent TEM analysis of the deformed NWs found significant differences in their behaviour. The bending of single crystal Ag NWs is accommodated by the formation of high angle grain boundaries, consistent with a conventional recovery and recrystallization mechanism after deformation. However, the bending of pentatwinned NWs must be accommodated by the coordinated deformation of all five subcrystals separated by the twin boundaries. Scanning nanobeam precession electron diffraction was used to determine the orientation and localisation of each of the subcrystals in the pentatwinned Ag NWs. The data shows that the five twin-related prisms follow an in-plane rotation across the boundary and that sharp high angle boundaries occurred in each

subcrystal. Subsequently, CSL theory was used to analyse the structure and stability of the boundaries in the bent pentatwinned Ag NWs. It is proposed that the observed preponderance of boundaries with a misorientation close to 40° and 70° indicate lower energy boundary configurations associated with low Σ boundaries in CSL theory. The geometrical constraint of the twinned subcrystals in the NWs limited the range of both bending axes and bending angles that can occur in NWs, so low CSL boundaries occur only along two principal directions, parallel to, and normal to the pentagon faces. This is consistent with the experiment observations.

After researching the mechanical behaviour of Ag NWs, this thesis explores the fatigue performances of Ag NWs networks, under bending fatigue loading conditions similar to those expected for applications in flexible electronics. A new sample preparation method assisted by the hybrid porous film was developed to allow *ex-situ* TEM observation of Ag NW networks before and after fatigue tests. TEM characterisation of pentatwinned Ag NWs after fatigue cycling, found the presence of widely spaced finite thickness defects across the width of the NW normal to the axis. These bamboo faults were characterized using SPED followed by signal decompositions. The bamboo faults were found to be a narrow crystal region having different orientations from the adjacent crystals, indicating that crystal rotation has occurred in the bamboo faults. As the growth direction of NWs is <1 1 0>, all the crystal rotation should be in {1 1 0} plane. Following on from our study of the characteristic bending deformation angles and associated low Σ value tilt boundaries, the Σ value of all possible {1 1 0} twist boundaries as a function of bending angle was determined and some of these correlated with the twists measured from a number of the bamboo faults investigated. To form twist boundaries in NWs, constraints within the NW network cause the applied (far-field) tensile stress to sometimes manifest as (local) torsional stress in an individual NW ligament. This is consistent with previous modelling work on the deformation of 3-D fibre

networks in free space, which predicted that the presence of fibre/fibre welded junctions constrains the network deformation and fibres become twisted in networks under far field uniaxial tensile loading.

Due to the coordinated deformation of all subcrystals in the pentatwinned Ag NWs and the coherence of the twist boundaries (low Σ), the bamboo faults are not expected to increase the electrical resistance of the NWs significantly. However, these faults are almost certainly the result of local dislocation activity and could be the defect nucleation sites that lead to the fracture of NWs. The bamboo fault density appeared to decrease in some wires during increased cycling, indicating that they may be reversible, which is believed to be from the high energy states of some faults.

This work has studied the mechanical response of Ag NWs systematically. Using SPED combined with a 4-D data decomposition method, the microstructure of deformed Ag NWs were also characterized using TEM at high resolution. Compared with single crystal Ag NWs, the existence of TBs in NWs influences the deformation mechanisms of pentatwinned Ag NWs, but it does not change the strength of NWs significantly in the tested diameter range, leading to a consistent size effect with other FCC metals. The exploration on the unique performances of pentatwinned Ag NWs, like the coherent bending grain boundaries and bamboo defaults, may stimulate further interest to explore the mechanical performances of nanometals containing TBs. Furthermore, this research also provides valuable insight to predict and improve the reliability of flexible electronics made by Ag NWs.

7.2 Outlook and Future Work

The influence of TBs and sample dimensions on the deformation mechanisms of Ag NWs have been explored in detail in this thesis. To further investigate the mechanical behaviours of these materials, a few possible studies may be recommended as a basis for future work.

In chapter 4, the tensile behaviour of both pentatwinned and single crystals Ag NWs was explored in the SEM. The rough surfaces of single crystal Ag NWs made by electrodeposition may affect the comparison between these two kinds of NWs. In the future, fabricating single crystal Ag NWs with controlled surface conditions could be explored. Physical vapour deposition seems a possible choice, however it may prove difficult to maintain a circular cross-section using these methods.

In this study, the deformed NWs were observed in TEM to explore the interaction between dislocations and TBs. To explore whether TBs are the dislocation nucleation sites or not, in-situ TEM observation of the dislocation nucleation and movement process under tension could be conducted in the future. This could use the TEM nanoindenter which was unavailable for this project. As there are multiple subcrystals overlapped along the incident electron beam for the pentatwinned Ag NWs, dislocation motions are not obvious in normal bright field images. Dark field images formed by the specific diffracted electron beam could be used to observe the deformation process of one subcrystal, thus exploring the dislocation nucleation mechanisms. Limited by the availability of the equipment, this work was not conducted in our current research. In addition to this, the size effect of the NWs should be explored over a much larger size range under similar experiment conditions. The strength of Ag NWs with ultra-small diameter (<50 nm) haven't been explored systematically in the literature. For nanocrystalline metals, the traditional strength mechanism does not follow the Hall-Petch equation when the grain size is below 10 nm, exhibiting instead an inverse Hall-Petch effect.[208,254] Similarly, it is also supposed that the strength of metal NWs will not follow the current size effect trend when the NW diameters are reduced to tens or several nanometres. However, the critical diameter range has not been known yet limited by the accuracy of the indenter and tensile tests sample preparation techniques. Future research

work could explore this problem assisted by advanced equipment and new sample preparation methods.

In chapter 5, the constraints of TBs on the bending behaviours of pentatwinned Ag NWs were observed under TEM and explained using the CSL theory. This work investigated the deformed structures of pentatwinned Ag NWs, while it is also worthwhile to further research on the deformation process of both single crystal and pentatwinned Ag NWs. Further work should study the deformation using controlled and quantified bending strain to better understand the evolution of the deformation microstructures and the significance of preferred deformation angles. Scanning nanobeam diffraction techniques are widely adopted for the characterization of the strain of materials in the nanoscale.[172,175] The difficulty for this research may be developing new experimental methods of bending tests in TEM with controlled bending angle and bending directions, as the bending tests methods adopted in this study are not suitable for in-situ strain measurements. The uncontrollable shrink of collodion film under the electron beam during the strain measurement process (using nanobeam diffraction methods) will result in changes of bending angles. Furthermore, in this chapter, to simplify the problems, only symmetric tilt boundaries were discussed. The predictions from this theory are consistent with experiment observations, giving reasonable explanations on the coordinated bending behaviours of pentatwinned Ag NWs. In the future, asymmetric tilt boundaries could also be considered to analyse the deformed structure of pentatwinned Ag NWs. Besides, the structure of several bent NWs was analysed to explore the bending properties of Ag NWs, but the influence of the sample size on the bending behaviours of Ag NWs have not been explored. As described in chapter 4, samples diameters have an influence on the tensile behaviour of nanowires, they may also play an important role in the bending deformation of Ag NWs. This is an interesting topic and could be explored in future work.

The third part of this work is researching the deformation behaviours of Ag NW networks in fatigue tests. The microstructural changes of individual Ag NW in the networks were characterized, where the bamboo faults were observed and explained by crystal rotation due to the constraints from NW junctions. The NW junction is a unique feature when the NWs are applied in the form of networks, while there is only limited work on welded NW junction characterizations.[234] Therefore, an attractive avenue for further research would be analysing the microstructure of joined junctions systematically and study their mechanical response. Moreover, the applied loading on NW networks in flexible electronics may also be different from that on NWs networks in this experiment, so the impacts of these differences could also be studied in the future.

This study is mainly focused on experimental work. To have an atomically resolved observation of the Ag NW deformation process, MD simulation could be adopted to explore the underline mechanisms in the future. For example, the twist deformation process of pentatwinned Ag NWs could be modelled by MD to unveil the formation mechanisms of the bamboo faults observed in experiments.

In addition to these, the explored failure mode of Ag NWs is the mechanical failure in this thesis, while other factors are also needed to be considered to predict and improved the reliability of fabricated flexible devices, such as electric migration and the effect of heating. Studies on the influence of these factors could be conducted in future work.

8 References

1. Wang, J. *et al.* Silver nanowire electrodes: Conductivity improvement without post-treatment and application in capacitive pressure sensors. *Nano-Micro Lett.* **7**, 51–58 (2014).

2. Wang, X. *et al.* A Highly Stretchable Transparent Self-Powered Triboelectric Tactile

Sensor with Metallized Nanofibers for Wearable Electronics. *Adv. Mater.* **1706738**, 1–8 (2018).

3. Kim, S. R., Kim, J. H. & Park, J. W. Wearable and Transparent Capacitive Strain Sensor with High Sensitivity Based on Patterned Ag Nanowire Networks. *ACS Appl. Mater. Interfaces* **9**, 26407–26416 (2017).

4. Kim, D. J. *et al.* Roll-to-roll slot-die coating of 400 mm wide, flexible, transparent Ag nanowire films for flexible touch screen panels. *Sci. Rep.* **6**, 1–12 (2016).

5. Margulis, G. Y. *et al.* Spray deposition of silver nanowire electrodes for semitransparent solid-state dye-sensitized solar cells. *Advanced Energy Materials* **3**, 1657–1663 (2013).

6. Celle, C. *et al.* Highly flexible transparent film heaters based on random networks of silver nanowires. *Nano Res.* **5**, 427–433 (2012).

7. Coskun, S., Selen Ates, E. & Emrah Unalan, H. Optimization of silver nanowire networks for polymer light emitting diode electrodes. *Nanotechnology* **24**, (2013).

8. Nam, V. & Lee, D. Copper Nanowires and Their Applications for Flexible, Transparent Conducting Films: A Review. *Nanomaterials* **6**, 47 (2016).

9. Kang, H. *et al.* Epitaxial-Growth-Induced Junction Welding of Silver Nanowire Network Electrodes. *ACS Nano* **12**, 4894–4902 (2018).

10. Chang, T. H., Cheng, G., Li, C. & Zhu, Y. On the size-dependent elasticity of penta-twinned silver nanowires. *Extrem. Mech. Lett.* **8**, 177–183 (2016).

11. Qin, Q. *et al.* Recoverable plasticity in penta-twinned metallic nanowires governed by dislocation nucleation and retraction. *Nat. Commun.* **6**, 5983 (2015).

12. Wang, L. *et al.* Mechanically Driven Grain Boundary Formation in Nickel Nanowires. *ACS Nano* **11**, 12500–12508 (2017).

13. Filleter, T. *et al.* Nucleation-controlled distributed plasticity in penta-twinned silver nanowires. *Small* **8**, 2986–2993 (2012).

14. Jang, D., Li, X., Gao, H. & Greer, J. R. Deformation mechanisms in nanotwinned metal

nanopillars. *Nat. Nanotechnol.* **7**, 594–601 (2012).

15. Midgley, P. A. & Eggeman, A. S. Precession electron diffraction - A topical review. *IUCrJ* **2**, 126–136 (2015).

16. Eggeman, A. S., Krakow, R. & Midgley, P. A. Scanning precession electron tomography for three-dimensional nanoscale orientation imaging and crystallographic analysis. *Nat. Commun.* **6**, 1–7 (2015).

17. Wilkinson, A. J., Meaden, G. & Dingley, D. J. High-resolution elastic strain measurement from electron backscatter diffraction patterns: New levels of sensitivity. *Ultramicroscopy* **106**, 307–313 (2006).

18. Eggeman, A. S. electron crystallography Scanning transmission electron diffraction methods. *Acta Cryst B* **B75**, 475–484 (2019).

19. Wallis, D., Hansen, L. N., Britton, T. B. & Wilkinson, A. J. High-Angular Resolution Electron Backscatter Diffraction as a New Tool for Mapping Lattice Distortion in Geological Minerals. *J. Geophys. Res. Solid Earth* **124**, 6337–6358 (2019).

20. Rouviere, J. L., Béché, A., Martin, Y., Denneulin, T. & Cooper, D. Improved strain precision with high spatial resolution using nanobeam precession electron diffraction. *Appl. Phys. Lett.* **103**, (2013).

21. Martineau, B. H., Johnstone, D. N., Helvoort, A. T. J. Van, Midgley, P. A. & Eggeman, A. S. Unsupervised machine learning applied to scanning precession electron diffraction data. *Adv. Struct. Chem. Imaging* **5:3**, (2019).

22. Liu, C., Ainsworth, C. A., Sampson, W. W. & Derby, B. Fatigue and the electrical resistance of silver nanowire networks. *Scr. Mater.* **181**, 97–100 (2020).

23. Schrenker, N. J. *et al.* Microscopic Deformation Modes and Impact of Network Anisotropy on the Mechanical and Electrical Performance of Five-fold Twinned Silver Nanowire Electrodes. *ACS Nano* (2020). doi:10.1021/acsnano.0c06480

24. Hwang, B., Kim, T. & Han, S. M. Compression and tension bending fatigue behavior of Ag nanowire network. *Extrem. Mech. Lett.* **8**, 266–272 (2016).

25. Lu, K., Lu, L. & Suresh, S. Strengthening materials by engineering coherent internal

boundaries at the nanoscale. *Science (80-.).* **324**, 349–352 (2009).

26. Grundmann, M. *The Physics of Semiconductors (2nd edition)*. *Springer* **20**, (2010).

27. Lu, K. Stabilizing nanostructures in metals using grain and twin boundary architectures. *Nat. Rev. Mater.* **1**, (2016).

28. Smallman, R. E. & Ngan, A. H. W. Surfaces, Grain Boundaries and Interfaces. in *Modern Physical Metallurgy* 415–442 (2014). doi:10.1016/b978-0-08-098204-5.00010-9

29. P. Lejcek R. Hull C. Jagadish R.M. Osgood, J. J. P. Z. W. H. W. Grain Boundary Segegation in Metals. *Springer Series in materials science* **136**, (2010).

30. Jang, D., Li, X., Gao, H. & Greer, J. R. Deformation mechanisms in nanotwinned metal nanopillars. *Nat. Nanotechnol.* **7**, 594–601 (2012).

31. Bernardi, M., Raja, S. N. & Lim, S. K. Nanotwinned gold nanowires obtained by chemical synthesis. *Nanotechnology* **21**, (2010).

32. Sun, Y. & Xia, Y. Large-scale synthesis of uniform silver nanowires through a soft, self-seeding, polyol process. *Adv. Mater.* **14**, 833–837 (2002).

33. Kim, S. H. *et al.* Deformation twinning of ultrahigh strength aluminum nanowire. *Acta Mater.* **160**, 14–21 (2018).

34. Zhu, Y. T. *et al.* Formation of single and multiple deformation twins in nanocrystalline fcc metals. *Acta Mater.* **57**, 3763–3770 (2009).

35. Sun, Y., Mayers, B., Herricks, T. & Xia, Y. Polyol synthesis of uniform silver nanowires: A plausible growth mechanism and the supporting evidence. *Nano Lett.* **3**, 955–960 (2003).

36. Liu, C.-H. & Yu, X. Silver nanowire-based transparent, flexible, and conductive thin film. *Nanoscale Res. Lett.* **6**, 75 (2011).

37. De, S. *et al.* Silver Nanowire Networks as Flexible, Transparent, Conducting Films: Extremely High DC to Optical Conductivity Ratios. *ACS Nano* **3**, 1767–1774 (2009).

38. Kwon, J. *et al.* Recent progress in silver nanowire based flexible/wearable

optoelectronics. *J. Mater. Chem. C* **6**, 7445–7461 (2018).

39. Sun, M., Cao, R., Xiao, F. & Deng, C. Surface and interface controlled yielding and plasticity in fivefold twinned Ag nanowires. *Comput. Mater. Sci.* **79**, 289–295 (2013).

40. Zhang, W. *et al.* Synergy between crystal strain and surface energy in morphological evolution of five-fold-twinned silver crystals. *J. Am. Chem. Soc.* **130**, 15581–15588 (2008).

41. Xie, L., Wang, C., Wang, Y., Wu, G. & Huang, X. Grain size effect on the mechanical behavior of metastable Fe-23Cr-8.5Ni alloy. *Metals (Basel).* **9**, (2019).

42. Hodge, A. M., Wang, Y. M. & Barbee, T. W. Mechanical deformation of high-purity sputter-deposited nano-twinned copper. *Scr. Mater.* **59**, 163–166 (2008).

43. Lu, L., Shen, Y., Chen, X., Qian, L. & Lu, K. Ultrahigh strength and high electrical conductivity in copper. *Science (80-.).* **304**, 422–6 (2004).

44. Wu, Z. X., Zhang, Y. W. & Srolovitz, D. J. Dislocation-twin interaction mechanisms for ultrahigh strength and ductility in nanotwinned metals. *Acta Mater.* **57**, 4508–4518 (2009).

45. Zhu, T., Li, J., Samanta, A., Kim, H. G. & Suresh, S. Interfacial plasticity governs strain rate sensitivity and ductility in nanostructured metals. *Proc. Natl. Acad. Sci.* **104**, 3031–3036 (2007).

46. You, Z. *et al.* Plastic anisotropy and associated deformation mechanisms in nanotwinned metals. *Acta Mater.* **61**, 217–227 (2013).

47. Wang, Y. B. & Sui, M. L. Atomic-scale in situ observation of lattice dislocations passing through twin boundaries. *Appl. Phys. Lett.* **94**, (2009).

48. Zhang, P., Zhang, Z. J., Li, L. L. & Zhang, Z. F. Twin boundary: Stronger or weaker interface to resist fatigue cracking? *Scr. Mater.* **66**, 854–859 (2012).

49. Zhu, Y. T. *et al.* Dislocation-twin interactions in nanocrystalline fcc metals. *Acta Mater.* **59**, 812–821 (2011).

50. Li, L. L., Zhang, Z. J., Zhang, P., Wang, Z. G. & Zhang, Z. F. Controllable fatigue cracking

mechanisms of copper bicrystals with a coherent twin boundary. *Nat. Commun.* **5**, (2014).

51. Shen, Y. F., Lu, L., Lu, Q. H., Jin, Z. H. & Lu, K. Tensile properties of copper with nano-scale twins. *Scr. Mater.* **52**, 989–994 (2005).

52. Naik, S. N. & Walley, S. M. The Hall–Petch and inverse Hall–Petch relations and the hardness of nanocrystalline metals. *J. Mater. Sci.* **55**, 2661–2681 (2020).

53. Lu, L., Chen, X., Huang, X. & Lu, K. Revealing the Maximum Strength in Nanotwinned Copper. *Science (80-.).* **323**, 607–610 (2009).

54. Padilla, H. A. & Boyce, B. L. A Review of fatigue behavior in nanocrystalline metals. *Exp. Mech.* **50**, 5–23 (2010).

55. Hanlon, T., Kwon, Y. N. & Suresh, S. Grain size effects on the fatigue response of nanocrystalline metals. *Scr. Mater.* **49**, 675–680 (2003).

56. Hosseinian, E. & Pierron, O. N. Quantitative in situ TEM tensile fatigue testing on nanocrystalline metallic ultrathin films. *Nanoscale* **5**, 12532–12541 (2013).

57. Li, L. L. *et al.* Strain localization and fatigue cracking behaviors of Cu bicrystal with an inclined twin boundary. *Acta Mater.* **73**, 167–176 (2014).

58. Jin, Z. H. *et al.* The interaction mechanism of screw dislocations with coherent twin boundaries in different face-centred cubic metals. *Scr. Mater.* **54**, 1163–1168 (2006).

59. Uchic, M. D. Sample Dimensions Influence Strength and Crystal Plasticity. *Science (80-.).* **305**, 986–989 (2004).

60. Greer, J. R., Oliver, W. C. & Nix, W. D. Size dependence of mechanical properties of gold at the micron scale in the absence of strain gradients. *Acta Mater.* **53**, 1821–1830 (2005).

61. Nix, W. D., Greer, J. R., Feng, G. & Lilleodden, E. T. Deformation at the nanometer and micrometer length scales: Effects of strain gradients and dislocation starvation. *Thin Solid Films* **515**, 3152–3157 (2007).

62. Greer, J. R. & Nix, W. D. Nanoscale gold pillars strengthened through dislocation

starvation. *Phys. Rev. B - Condens. Matter Mater. Phys.* **73**, 1–6 (2006).

63. Kiener, D., Motz, C., Schobert, T., Jenko, M. & Dehm, G. Determination of mechanical properties of copper at the micron scale. *Adv. Eng. Mater.* **8**, 1119–1125 (2006).

64. Kiener, D., Motz, C. & Dehm, G. Dislocation-induced crystal rotations in micro-compressed single crystal copper columns. *J. Mater. Sci.* **43**, 2503–2506 (2008).

65. Greer, J. R. & De Hosson, J. T. M. Plasticity in small-sized metallic systems: Intrinsic versus extrinsic size effect. *Prog. Mater. Sci.* **56**, 654–724 (2011).

66. Dou, R. & Derby, B. A universal scaling law for the strength of metal micropillars and nanowires. *Scr. Mater.* **61**, 524–527 (2009).

67. Volkert, C. A. & Lilleodden, E. T. Size effects in the deformation of sub-micron Au columns. *Philos. Mag.* **86**, 5567–5579 (2006).

68. Kim, J. Y. & Greer, J. R. Tensile and compressive behavior of gold and molybdenum single crystals at the nano-scale. *Acta Mater.* **57**, 5245–5253 (2009).

69. Frick, C. P., Clark, B. G., Orso, S., Schneider, A. S. & Arzt, E. Size effect on strength and strain hardening of small-scale [1 1 1] nickel compression pillars. *Mater. Sci. Eng. A* **489**, 319–329 (2008).

70. Lee, S. W., Han, S. M. & Nix, W. D. Uniaxial compression of fcc Au nanopillars on an MgO substrate: The effects of prestraining and annealing. *Acta Mater.* **57**, 4404–4415 (2009).

71. Jennings, A. T., Li, J. & Greer, J. R. Emergence of strain-rate sensitivity in Cu nanopillars: Transition from dislocation multiplication to dislocation nucleation. *Acta Mater.* **59**, 5627–5637 (2011).

72. Ng, K. S. & Ngan, A. H. W. Stochastic nature of plasticity of aluminum micro-pillars. *Acta Mater.* **56**, 1712–1720 (2008).

73. Csikor, F. F., Motz, C., Weygand, D., Zaiser, M. & Zapperi, S. Dislocation Avalanches, Strain Bursts, and the Problem of Plastic Forming at the Micrometer Scale. *Science (80-.).* **318**, 251–254 (2007).

74. Shan, Z. W., Mishra, R. K., Syed Asif, S. A., Warren, O. L. & Minor, A. M. Mechanical annealing and source-limited deformation in submicrometre-diameter Ni crystals. *Nat. Mater.* **7**, 115–119 (2008).

75. Liang, Z. Y., De Hosson, J. T. M. & Huang, M. X. Size effect on deformation twinning in face-centred cubic single crystals: Experiments and modelling. *Acta Mater.* **129**, 1–10 (2017).

76. Buzzi, S., Dietiker, M., Kunze, K., Spolenak, R. & Löffler, J. F. Deformation behavior of silver submicrometer-pillars prepared by nanoimprinting. *Philos. Mag.* **89**, 869–884 (2009).

77. Lee, S. W., Cheng, Y., Ryu, I. & Greer, J. R. Cold-temperature deformation of nano-sized tungsten and niobium as revealed by in-situ nano-mechanical experiments. *Sci. China Technol. Sci.* **57**, 652–662 (2014).

78. Brinckmann, S., Kim, J. Y. & Greer, J. R. Fundamental differences in mechanical behavior between two types of crystals at the nanoscale. *Phys. Rev. Lett.* **100**, 1–4 (2008).

79. Nix, W. D., Greer, J. R., Feng, G. & Lilleodden, E. T. Deformation at the nanometer and micrometer length scales: Effects of strain gradients and dislocation starvation. *Thin Solid Films* **515**, 3152–3157 (2007).

80. Oh, S. H., Legros, M., Kiener, D. & Dehm, G. In situ observation of dislocation nucleation and escape in a submicrometre aluminium single crystal. *Nat. Mater.* **8**, 95–100 (2009).

81. Kiener, D., Grosinger, W., Dehm, G. & Pippan, R. A further step towards an understanding of size-dependent crystal plasticity: In situ tension experiments of miniaturized single-crystal copper samples. *Acta Mater.* **56**, 580–592 (2008).

82. Jennings, A. T. & Greer, J. R. Tensile deformation of electroplated copper nanopillars. *Philos. Mag.* **91**, 1108–1120 (2010).

83. Park, M., Kim, W., Hwang, B. & Han, S. M. Effect of varying the density of Ag nanowire networks on their reliability during bending fatigue. *Scr. Mater.* **161**, 70–73 (2019).

84. Hwang, B., Shin, H. A. S., Kim, T., Joo, Y. C. & Han, S. M. Highly reliable Ag nanowire flexible transparent electrode with mechanically welded junctions. *Small* **10**, 3397–3404 (2014).

85. Chen, L. Y., He, M.-R., Shin, J., Richter, G. & Gianola, D. S. Measuring surface dislocation nucleation in defect-scarce nanostructures. *Nat. Mater.* **14**, 707–713 (2015).

86. Richter, G. *et al.* Ultrahigh strength single crystalline nanowhiskers grown by physical vapor deposition. *Nano Lett.* **9**, 3048–3052 (2009).

87. Seo, J. H. *et al.* Superplastic deformation of defect-free Au nanowires via coherent twin propagation. *Nano Lett.* **11**, 3499–3502 (2011).

88. Seo, J. H. *et al.* Origin of size dependency in coherent-twin-propagation-mediated tensile deformation of noble metal nanowires. *Nano Lett.* **13**, 5112–5116 (2013).

89. Zhu, Y., Xu, F., Qin, Q., Fung, W. Y. & Lu, W. Mechanical Properties of Vapor−Liquid−Solid Synthesized Silicon Nanowires. *Nano Lett.* **9**, 3934–3939 (2009).

90. Zhu, Y. *et al.* Size effects on elasticity, yielding, and fracture of silver nanowires: In situ experiments. *Phys. Rev. B - Condens. Matter Mater. Phys.* **85**, 1–7 (2012).

91. Zhang, Y. *et al.* Direct observation of super-plasticity of beta-SiC nanowires at low temperature. *Adv. Funct. Mater.* **17**, 3435–3440 (2007).

92. Yue, Y., Liu, P., Zhang, Z., Han, X. & Ma, E. Approaching the theoretical elastic strain limit in copper nanowires. *Nano Lett.* **11**, 3151–3155 (2011).

93. Deng, Q. *et al.* Uniform tensile elongation in framed submicron metallic glass specimen in the limit of suppressed shear banding. *Acta Mater.* **59**, 6511–6518 (2011).

94. Cited, R., City, O. & Data, R. U.-A. (12) United States Patent. **1**, 0–4 (2008).

95. Guo, H. *et al.* Mechanics and dynamics of the strain-induced M1-M2 structural phase transition in individual VO_2 nanowires. *Nano Lett.* **11**, 3207–13 (2011).

96. Chisholm, C. *et al.* Dislocation starvation and exhaustion hardening in Mo alloy nanofibers. *Acta Mater.* **60**, 2258–2264 (2012).

97. Chen, L. Y., Richter, G., Sullivan, J. P. & Gianola, D. S. Lattice anharmonicity in defect-free Pd nanowhiskers. *Phys. Rev. Lett.* **109**, (2012).

98. Chen, L. Y. *et al.* Temperature controlled tensile testing of individual nanowires. *Rev. Sci. Instrum.* **85**, (2014).

99. Kiener, D., Kaufmann, P. & Minor, A. M. Strength, hardening, and failure observed by in situ TEM tensile testing. *Adv. Eng. Mater.* **14**, 960–967 (2012).

100. Zhang, X., Li, X. & Gao, H. Size and strain rate effects in tensile strength of penta-twinned Ag nanowires. *Acta Mech. Sin.* (2017). doi:10.1007/s10409-017-0675-6

101. Kiener, D., Grosinger, W. & Dehm, G. On the importance of sample compliance in uniaxial microtesting. *Scr. Mater.* **60**, 148–151 (2009).

102. Zhu, T., Li, J., Samanta, A., Leach, A. & Gall, K. Temperature and strain-rate dependence of surface dislocation nucleation. *Phys. Rev. Lett.* **100**, 1–4 (2008).

103. Parthasarathy, T. A., Rao, S. I., Dimiduk, D. M., Uchic, M. D. & Trinkle, D. R. Contribution to size effect of yield strength from the stochastics of dislocation source lengths in finite samples. *Scr. Mater.* **56**, 313–316 (2007).

104. Kiener, D. & Minor, A. M. Source truncation and exhaustion: Insights from quantitative in situ TEM tensile testing. *Nano Lett.* **11**, 3816–3820 (2011).

105. Yin, S., Cheng, G., Richter, G., Gao, H. & Zhu, Y. Transition of Deformation Mechanisms in Single-Crystalline Metallic Nanowires. *ACS Nano* **13**, 9082–9090 (2019).

106. Cheng, G. *et al.* Anomalous Tensile Detwinning in Twinned Nanowires. *Phys. Rev. Lett.* **256101**, 1–6 (2017).

107. Jennings, A. T. *et al.* Modeling dislocation nucleation strengths in pristine metallic nanowires under experimental conditions. *Acta Mater.* **61**, 2244–2259 (2013).

108. Roos, B., Kapelle, B., Richter, G. & Volkert, C. A. Surface dislocation nucleation controlled deformation of Au nanowires. *Appl. Phys. Lett.* **105**, (2014).

109. Lu, Y., Song, J., Huang, J. Y. & Lou, J. Surface dislocation nucleation mediated

deformation and ultrahigh strength in sub-10-nm gold nanowires. *Nano Res.* **4**, 1261–1267 (2011).

110. Richter, G. *et al.* Ultrahigh Strength Single Crystalline Nanowhiskers Grown by Physical Vapor Deposition.

111. Wan, H. Y., Luo, X. M., Li, X., Liu, W. & Zhang, G. P. Nanotwin-enhanced fatigue resistance of ultrathin Ag films for flexible electronics applications. *Mater. Sci. Eng. A* **676**, 421–426 (2016).

112. Hirth, J. P., Lothe, J. & Mura, T. Theory of Dislocations (2nd ed.). *J. Appl. Mech.* **50**, 476–477 (1983).

113. Greer, J. R., Weinberger, C. R. & Cai, W. Comparing the strength of f.c.c. and b.c.c. sub-micrometer pillars: Compression experiments and dislocation dynamics simulations. *Mater. Sci. Eng. A* **493**, 21–25 (2008).

114. Mompiou, F. *et al.* Source-based strengthening of sub-micrometer Al fibers. *Acta Mater.* **60**, 977–983 (2012).

115. Rao, S. I. *et al.* Athermal mechanisms of size-dependent crystal flow gleaned from three-dimensional discrete dislocation simulations. *Acta Mater.* **56**, 3245–3259 (2008).

116. Motz, C., Weygand, D., Senger, J. & Gumbsch, P. Initial dislocation structures in 3-D discrete dislocation dynamics and their influence on microscale plasticity. *Acta Mater.* **57**, 1744–1754 (2009).

117. Rabkin, E. & Srolovitz, D. J. Onset of plasticity in gold nanopillar compression. *Nano Lett.* **7**, 101–107 (2007).

118. Diao, J., Gall, K., Dunn, M. L. & Zimmerman, J. A. Atomistic simulations of the yielding of gold nanowires. *Acta Mater.* **54**, 643–653 (2006).

119. Zheng, H. *et al.* Discrete plasticity in sub-10-nm-sized gold crystals. *Nat. Commun.* **1**, 144 (2010).

120. Gu, X. W., Wu, Z., Zhang, Y. W., Srolovitz, D. J. & Greer, J. R. Microstructure versus flaw: Mechanisms of failure and strength in nanostructures. *Nano Lett.* **13**, 5703–5709 (2013).

121. Leach, A. M., McDowell, M. & Gall, K. Deformation of top-down and bottom-up silver nanowires. *Adv. Funct. Mater.* **17**, 43–53 (2007).

122. Bernal, R. A. *et al.* Intrinsic bauschinger effect and recoverable plasticity in pentatwinned silver nanowires tested in tension. *Nano Lett.* **15**, 139–146 (2015).

123. Van Swygenhoven, H., Derlet, P. M. & Frøseth, A. G. Stacking fault energies and slip in nanocrystalline metals. *Nat. Mater.* **3**, 399–403 (2004).

124. Cao, A., Wei, Y. & Mao, S. X. Alternating starvation of dislocations during plastic yielding in metallic nanowires. *Scr. Mater.* **59**, 219–222 (2008).

125. Volkert, C. A. & Lilleodden, E. T. Size effects in the deformation of sub-micron Au columns. *Philos. Mag.* **86**, 5567–5579 (2006).

126. Uchic, M. D., Shade, P. A. & Dimiduk, D. M. Plasticity of Micrometer-Scale Single Crystals in Compression. *Annu. Rev. Mater. Res.* **39**, 361–386 (2009).

127. Kraft, O., Gruber, P. A., Mönig, R. & Weygand, D. Plasticity in Confined Dimensions. *Annu. Rev. Mater. Res.* **40**, 293–317 (2010).

128. Shin, J. *et al.* Controlling dislocation nucleation-mediated plasticity in nanostructures via surface modification. *Acta Mater.* **166**, 572–586 (2019).

129. Khalil, A., Singh Lalia, B., Hashaikeh, R. & Khraisheh, M. Electrospun metallic nanowires: Synthesis, characterization, and applications. *J. Appl. Phys.* **114**, (2013).

130. Tan, M. & Chen, X. Growth Mechanism of Single Crystal Nanowires of fcc Metals (Ag, Cu, Ni) and hcp Metal (Co) Electrodeposited. *J. Electrochem. Soc.* **159**, K15 (2012).

131. Riveros, G., Gómez, H., Cortes, A., Marotti, R. E. & Dalchiele, E. A. Silver nanowire arrays electrochemically grown into nanoporous anodic alumina templates. *Nanotechnology* 561–570 (2006). doi:10.1007/s00339-004-3112-1

132. Kurowska, E., Brzózka, A., Jarosz, M., Sulka, G. D. & Jaskuła, M. Silver nanowire array sensor for sensitive and rapid detection of H2O2. *Electrochim. Acta* **104**, 439–447 (2013).

133. Dou, R. & Derby, B. The strength of gold nanowire forests. *Scr. Mater.* **59**, 151–154

(2008).

134. Sun, Y., Gates, B., Mayers, B. & Xia, Y. Crystalline Silver Nanowires by Soft Solution Processing. *Nano Lett.* **2**, 165–168 (2002).

135. Sinha, A. K., Hwang, D. W. & Hwang, L. P. A novel approach to bulk synthesis of carbon nanotubes filled with metal by a catalytic chemical vapor deposition method. *Chem. Phys. Lett.* **332**, 455–460 (2000).

136. Wu, B. *et al.* Microstructure-hardened silver nanowires. *Nano Lett.* **6**, 468–472 (2006).

137. Wu, J. Y., Nagao, S., He, J. Y. & Zhang, Z. L. Role of five-fold twin boundary on the enhanced mechanical properties of fcc Fe nanowires. *Nano Lett.* **11**, 5264–5273 (2011).

138. Gao, Y. *et al.* Investigation on the mechanical behavior of fivefold twinned silver nanowires. *Comput. Mater. Sci.* **55**, 322–328 (2012).

139. Narayanan, S., Cheng, G., Zeng, Z., Zhu, Y. & Zhu, T. Strain Hardening and Size Effect in Five-fold Twinned Ag Nanowires. *Nano Lett.* **15**, 4037–4044 (2015).

140. Cao, A. & Ma, E. Sample shape and temperature strongly influence the yield strength of metallic nanopillars. *Acta Mater.* **56**, 4816–4828 (2008).

141. Zhao, Y. X., Zhang, Y., Li, Y. P. & Yan, Z. F. Strain-Induced Structural Evolution and High Robustness in Single Crystalline Fivefold Twinned Cu@C Coaxial Nanowires. *Adv. Mater. Res.* **1033**–**1034**, 1213–1219 (2014).

142. Cao, K. *et al.* Size-dependent fracture behavior of silver nanowires. *Nanotechnology* **29**, (2018).

143. Ramachandramoorthy, R., Gao, W., Bernal, R. & Espinosa, H. High Strain Rate Tensile Testing of Silver Nanowires: Rate-Dependent Brittle-to-Ductile Transition. *Nano Lett.* **16**, 255–263 (2016).

144. Chen, Y., Dorgan, B. L., McIlroy, D. N. & Aston, D. E. On the importance of boundary conditions on nanomechanical bending behavior and elastic modulus determination of silver nanowires. *J. Appl. Phys.* **100**, (2006).

145. Wang, L. *et al.* Dynamic and atomic-scale understanding of the twin thickness effect on dislocation nucleation and propagation activities by in situ bending of Ni nanowires. *Acta Mater.* **90**, 194–203 (2015).

146. Cao, A. J., Wei, Y. G. & Mao, S. X. Deformation mechanisms of face-centered-cubic metal nanowires with twin boundaries. *Appl. Phys. Lett.* **90**, 88–91 (2007).

147. Carter, C. B. & Holmes, S. M. The stacking-fault energy of nickel. *Philos. Mag.* **35**, 1161–1171 (1977).

148. Zhong, S. *et al.* Nanoscale twinned copper nanowire formation by direct electrodeposition. *Small* **5**, 2265–2270 (2009).

149. Afanasyev, K. a, Sansoz, F. & Afanasyev Konstantin A., S. F. Strengthening in Gold-Nanopillars with Nanoscale twins. *Nano Lett.* **7**, 2056–2062 (2007).

150. Jennings, A. T. & Greer, J. R. Tensile deformation of electroplated copper nanopillars. *Philos. Mag.* **91**, 1108–1120 (2011).

151. Li, P. *et al.* In situ transmission electron microscopy investigation on fatigue behavior of single ZnO wires under high-cycle strain. *Nano Lett.* **14**, 480–485 (2014).

152. Hwang, B., Shin, H. A. S., Kim, T., Joo, Y. C. & Han, S. M. Highly reliable Ag nanowire flexible transparent electrode with mechanically welded junctions. *Small* **10**, 3397–3404 (2014).

153. Kim, H. Y., Kim, J. Y., Yoo, K. T., Yang, W. J. & Byeon, J. W. Failure mechanism of Ag nanowire-coated conductive transparent electrode for wearable devices under folding and torsional fatigue condition. *Microelectron. Reliab.* **88–90**, 345–349 (2018).

154. Hwang, B., Seol, J. G., An, C. H. & Kim, S. H. Bending fatigue behavior of silver nanowire networks with different densities. *Thin Solid Films* **625**, 1–5 (2017).

155. Ensslen, C. *et al.* Mechanical annealing of Cu-Si nanowires during high-cycle fatigue. *MRS Commun.* **4**, 83–87 (2014).

156. Zhang, H., Jiang, C. & Lu, Y. Low-Cycle Fatigue Testing of Ni Nanowires Based on a Micro-Mechanical Device. *Exp. Mech.* **57**, 495–500 (2017).

157. Masuda, H. & Fukuda, K. Ordered Metal Nanohole Arrays Made by a Two-Step Replication of Honeycomb Structures of Anodic Alumina. *Science (80-.).* **268**, 1466–1468 (1995).

158. Toimil Molares, M. E. *et al.* Single-crystalline copper nanowires produced by electrochemical deposition in polymeric ion track membranes. *Adv. Mater.* **13**, 62–65 (2001).

159. Tian, M., Wang, J., Kurtz, J., Mallouk, T. E. & Chan, M. H. W. Electrochemical growth of single-crystal metal nanowires via a two-dimensional nucleation and growth mechanism. *Nano Lett.* **3**, 919–923 (2003).

160. Pan, H., Sun, H., Poh, C., Feng, Y. & Lin, J. Single-crystal growth of metallic nanowires with preferred orientation. *Nanotechnology* **16**, 1559–1564 (2005).

161. Maurer, F. *et al.* Preferred growth orientation of metallic fcc nanowires under direct and alternating electrodeposition conditions. *Nanotechnology* **18**, (2007).

162. Wroński, S., Tarasiuk, J., Bacroix, B., Baczmański, A. & Braham, C. Investigation of plastic deformation heterogeneities in duplex steel by EBSD. *Mater. Charact.* **73**, 52–60 (2012).

163. Konig, U. & Davepon, B. Microstructure of polycrystalline Ti and its microelectrochemical properties by means of electron-backscattering diffraction (EBSD). *Electrochim. Acta* **47**, 149–160 (2001).

164. Rowenhorst, D. J., Gupta, A., Feng, C. R. & Spanos, G. 3D Crystallographic and morphological analysis of coarse martensite: Combining EBSD and serial sectioning. *Scr. Mater.* **55**, 11–16 (2006).

165. Wilkinson, A. J. Advances in SEM-based diffraction studies of defects and strains in semiconductors. *J. Electron Microsc. (Tokyo).* **49**, 299–310 (2000).

166. Wilkinson, A. J. & Britton, T. Ben. Strains, planes, and EBSD in materials science. *Mater. Today* **15**, 366–376 (2012).

167. Troost, K. Z., Van Der Sluis, P. & Gravesteijn, D. J. Microscale elastic-strain determination by backscatter Kikuchi diffraction in the scanning electron microscope.

Appl. Phys. Lett. **62**, 1110–1112 (1993).

168. Miyamoto, G., Shibata, A., Maki, T. & Furuhara, T. Precise measurement of strain accommodation in austenite matrix surrounding martensite in ferrous alloys by electron backscatter diffraction analysis. *Acta Mater.* **57**, 1120–1131 (2009).

169. Wright, S. I., Nowell, M. M. & Field, D. P. A review of strain analysis using electron backscatter diffraction. *Microsc. Microanal.* **17**, 316–329 (2011).

170. Demir, E., Raabe, D., Zaafarani, N. & Zaefferer, S. Investigation of the indentation size effect through the measurement of the geometrically necessary dislocations beneath small indents of different depths using EBSD tomography. *Acta Mater.* **57**, 559–569 (2009).

171. Wallis, D., Hansen, L. N., Britton, T. Ben & Wilkinson, A. J. Ultramicroscopy Geometrically necessary dislocation densities in olivine obtained using high-angular resolution electron backscatter diffraction. *Ultramicroscopy* **168**, 34–45 (2017).

172. Béché, A., Rouvière, J. L., Barnes, J. P. & Cooper, D. Strain measurement at the nanoscale: Comparison between convergent beam electron diffraction, nano-beam electron diffraction, high resolution imaging and dark field electron holography. *Ultramicroscopy* **131**, 10–23 (2013).

173. Tanaka, M. & Tsuda, K. Convergent-beam electron diffraction. *J. Electron Microsc. (Tokyo).* **60**, 245–267 (2011).

174. Vincent, R. & Midgley, P. A. Double conical beam-rocking system for measurement of integrated electron diffraction intensities. *Ultramicroscopy* **53**, 271–282 (1994).

175. Cooper, D., Denneulin, T., Bernier, N., Béché, A. & Rouvière, J. L. Strain mapping of semiconductor specimens with nm-scale resolution in a transmission electron microscope. *Micron* **80**, 145–165 (2016).

176. Brunetti, G. *et al.* Confirmation of the domino-cascade model by lifepo4/fepo 4 precession electron diffraction. *Chem. Mater.* **23**, 4515–4524 (2011).

177. Guillemin, S. *et al.* Spontaneous shape transition of thin films into ZnO nanowires with high structural and optical quality. *Nanoscale* **7**, 16994–17003 (2015).

178. Ktari, H. H., Couzinie, J. P., Bourgon, J., Champion, Y. & Njah, N. Orientation imaging-ASTAR investigation of the grain and precipitate morphology in Al-Cu-Mg alloy processed by Equal Channel Angular Pressing. *J. Alloys Compd.* **647**, 152–158 (2015).

179. Lillo, T. M., Van Rooyen, I. J. & Wu, Y. Q. Precession electron diffraction for SiC grain boundary characterization in unirradiated TRISO fuel. *Nucl. Eng. Des.* **305**, 277–283 (2016).

180. Rauch, E. F. *et al.* Automated nanocrystal orientation and phase mapping in the transmission electron microscope on the basis of precession electron diffraction. *Zeitschrift fur Krist.* **225**, 103–109 (2010).

181. Gammer, C., Ozdol, V. B., Liebscher, C. H. & Minor, A. M. Diffraction contrast imaging using virtual apertures. *Ultramicroscopy* **155**, 1–10 (2015).

182. R.B.W. *Introduction to dislocations*. *Journal of the Less Common Metals* **10**, (1966).

183. Rauch, E. F. & Véron, M. Virtual dark-field images reconstructed from electron diffraction patterns. *EPJ Appl. Phys.* **66**, 1–6 (2014).

184. Klenov, D. O. & Stemmer, S. Contributions to the contrast in experimental high-angle annular dark-field images. *Ultramicroscopy* **106**, 889–901 (2006).

185. Valery, A., Rauch, E. F., ClÉment, L. & Lorut, F. Retrieving overlapping crystals information from TEM nano-beam electron diffraction patterns. *J. Microsc.* **268**, 208–218 (2017).

186. Lee, D. D. & Seung, H. S. Learning the parts of objects by non-negative matrix factorization. *Nature* **401**, 788–791 (1999).

187. Müller, K. *et al.* Scanning transmission electron microscopy strain measurement from millisecond frames of a direct electron charge coupled device. *Appl. Phys. Lett.* **101**, (2012).

188. HyperSpy: multi-dimensional data analysis toolbox — HyperSpy. Available at: https://hyperspy.org/. (Accessed: 13th June 2021)

189. Bergh, T. *et al.* Nanocrystal segmentation in scanning precession electron diffraction data. *J. Microsc.* **00**, 1–10 (2019).

190. Uesugi, F. *et al.* Ultramicroscopy Non-negative matrix factorization for mining big data obtained using four-dimensional scanning transmission electron microscopy. *Ultramicroscopy* **221**, 113168 (2021).

191. Lorut, F. Retrieving overlapping crystals information from TEM nano-beam. doi:10.1111/jmi.12599

192. Sannicolo, T. *et al.* Metallic Nanowire-Based Transparent Electrodes for Next Generation Flexible Devices: a Review. *Small* **12**, 6052–6075 (2016).

193. Chen, D. & Gao, L. Large-scale growth and end-to-end assembly of silver nanorods by PVP-directed polyol process. *J. Cryst. Growth* **264**, 216–222 (2004).

194. Zhao, H., Eggeman, A. S., Race, C. P. & Derby, B. Geometrical constraints on the bending deformation of Penta-twinned silver nanowires. *Acta Mater.* **185**, 110–118 (2020).

195. Fu, X. & Yuan, J. Non-destructive detection of cross-sectional strain and defect structure in an individual Ag five-fold twinned nanowire by 3D electron diffraction mapping. *Sci. Rep.* **7**, 1–12 (2017).

196. Hirth, J. P., Hirth, G. & Wang, J. Disclinations and disconnections in minerals and metals. *Proc. Natl. Acad. Sci. U. S. A.* **117**, 196–204 (2020).

197. Dimiduk, D. M., Uchic, M. D. & Parthasarathy, T. A. Size-affected single-slip behavior of pure nickel microcrystals. *Acta Mater.* **53**, 4065–4077 (2005).

198. Lu, N., Suo, Z. & Vlassak, J. J. The effect of film thickness on the failure strain of polymer-supported metal films. *Acta Mater.* **58**, 1679–1687 (2010).

199. Arzt, E. Size effects in materials due to microstructural and dimensional constraints: A comparative review. *Acta Mater.* **456**, 5611–5626 (1998).

200. Imrich, P. J., Kirchlechner, C., Kiener, D. & Dehm, G. Internal and external stresses: In situ TEM compression of Cu bicrystals containing a twin boundary. *Scr. Mater.* **100**, 94–97 (2015).

201. Imrich, P. J., Kirchlechner, C. & Dehm, G. Influence of inclined twin boundaries on the deformation behavior of Cu micropillars. *Mater. Sci. Eng. A* **642**, 65–70 (2015).

202. Wei, D. A. *et al.* Effects of twin boundary orientation on plasticity of bicrystalline copper micropillars: A discrete dislocation dynamics simulation study. *Acta Mater.* **176**, 289–296 (2019).

203. Reyes-Gasga, J. *et al.* On the structure of nanorods and nanowires with pentagonal cross-sections. *J. Cryst. Growth* **286**, 162–172 (2006).

204. Abbas, K. Characterization of the mechanical properties of freestanding platinum thin films. *Ph.D thesis Univ. New Mex.* (2013).

205. Abbas, K. *et al.* Nanoscale size effects on the mechanical properties of platinum thin films and cross- sectional grain morphology. *J. Micromechanics Microengineering* **26**, 1–7 (2016).

206. Buzzi, S., Dietiker, M., Kunze, K., Spolenak, R. & Löffler, J. F. Deformation behavior of silver submicrometer-pillars prepared by nanoimprinting. *Philos. Mag.* **89**, 869–884 (2009).

207. Carter, D. B. W. C. B. *Transmission Electron Microscopy*. (Springer, 2009).

208. Cordero, Z. C., Knight, B. E. & Schuh, C. A. Six decades of the Hall–Petch effect – a survey of grain-size strengthening studies on pure metals. *Int. Mater. Rev.* **61**, 495–512 (2016).

209. Dao, M., Lu, L., Shen, Y. F. & Suresh, S. Strength, strain-rate sensitivity and ductility of copper with nanoscale twins. *Acta Mater.* **54**, 5421–5432 (2006).

210. Langley, D. *et al.* Flexible transparent conductive materials based on silver nanowire networks: A review. *Nanotechnology* **24**, (2013).

211. Wiley, B., Sun, Y., Mayers, B. & Xia, Y. Shape-controlled synthesis of metal nanostructures: The case of silver. *Chem. - A Eur. J.* **11**, 454–463 (2005).

212. Ainsworth, C. A., Derby, B. & Sampson, W. W. Interdependence of Resistance and Optical Transmission in Conductive Nanowire Networks. *Adv. Theory Simulations* **1**, 1700011 (2018).

213. Zhu, Y. *et al.* Size effects on elasticity, yielding, and fracture of silver nanowires: In situ experiments. *Phys. Rev. B - Condens. Matter Mater. Phys.* **85**, 1–7 (2012).

214. Wu, B., Heidelberg, A. & Boland, J. J. Mechanical properties of ultrahigh-strength gold nanowires. *Nat. Mater.* **4**, 525–529 (2005).

215. Wu, B. *et al.* Microstructure-hardened silver nanowires. *Nano Lett.* **6**, 468–472 (2006).

216. Vlassov, S. *et al.* Elasticity and yield strength of pentagonal silver nanowires: In situ bending tests. *Mater. Chem. Phys.* **143**, 1026–1031 (2014).

217. Zhang, Z. *et al.* Low-temperature in situ large strain plasticity of ceramic SiC nanowires and its atomic-scale mechanism. *Nano Lett.* **7**, 452–457 (2007).

218. Zheng, K. *et al.* Electron-beam-assisted superplastic shaping of nanoscale amorphous silica. *Nat. Commun.* **1**, 1–8 (2010).

219. Dou, R. & Derby, B. Deformation mechanisms in gold nanowires and nanoporous gold. *Philos. Mag.* **91**, 1070–1083 (2011).

220. Chen, H. *et al.* Transmission-electron-microscopy study on fivefold twinned silver nanorods. *J. Phys. Chem. B* **108**, 12038–12043 (2004).

221. Wang, L., Zheng, K., Zhang, Z. & Han, X. Direct atomic-scale imaging about the mechanisms of ultralarge bent straining in si nanowires. *Nano Lett.* **11**, 2382–2385 (2011).

222. Wang, L. *et al.* In situ atomic-scale observation of continuous and reversible lattice deformation beyond the elastic limit. *Nat. Commun.* **4**, 1–7 (2013).

223. Martineau, B. H., Johnstone, D. N., van Helvoort, A. T. J., Midgley, P. A. & Eggeman, A. S. Unsupervised machine learning applied to scanning precession electron diffraction data. *Adv. Struct. Chem. Imaging* **5**, (2019).

224. Rauch, E. F. *et al.* Automated nanocrystal orientation and phase mapping in the transmission electron microscope on the basis of precession electron diffraction. *Zeitschrift fur Krist.* **225**, 103–109 (2010).

225. Rauch, E. F. Automatic Crystal Orientation and Phase Mapping in TEM by Precession Diffraction. *Microsc. Microanal.* S5–S8 (2008).

226. Balluffi, R. W. & Brokman, A. Coincidence Lattice Model for the Structure and Energy

of Grain Boundaries. *Acta Metall.* **29**, 1703–1719 (1981).

227. Grimmer, H., Bollmann, W. & Warrington, D. H. Coincidence-ste lattices and complete patter-shift lattices in cubic crystals. *Acta Crystallogr A* **30**, 197–207 (1974).

228. Brandon, D. G. The Structure of High Angle Grain Boundaries. *Acta Metall.* **14**, 1479–1484 (1966).

229. X. C. Jiang*†S. X. Xiong†Z. A. Tian†‡C. Y. Chen†W. M. Chen†A. B. Yu†. Twinned Structure and Growth of V-Shaped Silver Nanowires Generated by a Polyol−Thermal Approach. *J. Phys. Chem. C* **115**, 1800–1810 (2010).

230. Peng, P., Liu, L., Gerlich, A. P., Hu, A. & Zhou, Y. N. Self-oriented nanojoining of silver nanowires via surface selective activation. *Part. Part. Syst. Charact.* **30**, 420–426 (2013).

231. Lee, J. H., Lee, P., Lee, D., Lee, S. S. & Ko, S. H. Large-scale synthesis and characterization of very long silver nanowires via successive multistep growth. *Cryst. Growth Des.* **12**, 5598–5605 (2012).

232. Araki, T. *et al.* Low haze transparent electrodes and highly conducting air dried films with ultra-long silver nanowires synthesized by one-step polyol method. *Nano Res.* **7**, 236–245 (2014).

233. Menamparambath, M. M. *et al.* Reduced haze of transparent conductive films by smaller diameter silver nanowires. *Nanotechnology* **27**, (2016).

234. Garnett, E. C. *et al.* Self-limited plasmonic welding of silver nanowire junctions. *Nat. Mater.* **11**, 241–249 (2012).

235. Hwang, B., An, C. H. & Becker, S. Highly robust Ag nanowire flexible transparent electrode with UV-curable polyurethane-based overcoating layer. *Mater. Des.* **129**, 180–185 (2017).

236. Hwang, B. *et al.* Highly Flexible and Transparent Ag Nanowire Electrode Encapsulated with Ultra-Thin Al2O3: Thermal, Ambient, and Mechanical Stabilities. *Sci. Rep.* **7**, 1–7 (2017).

237. Sergei Vlassov, Magnus Mets, Boris Polyakov, Jianjun Bian, L. M. D. and V. Z. Abrupt

elastic to plastic transition in pentagonal nanowires under bending. 0–17 (2019). doi:10.3762/bxiv.2019.90.v1

238. Daniel D. Lee; H. Sebastian Seung. Algorithms for non-negative matrix factorization. (2001). doi:10.1109/IJCNN.2008.4634046

239. Ramachandramoorthy, R. *et al.* Reliability of Single Crystal Silver Nanowire-Based Systems: Stress Assisted Instabilities. *ACS Nano* **11**, 4768–4776 (2017).

240. Tokuno, T. *et al.* Fabrication of silver nanowire transparent electrodes at room temperature. *Nano Res.* **4**, 1215–1222 (2011).

241. Ramachandramoorthy, R. *et al.* Reliability of Single Crystal Silver Nanowire-Based Systems: Stress Assisted Instabilities. *ACS Nano* **11**, 4768–4776 (2017).

242. Novoselov, K. S. Electric Field Effect in Atomically Thin Carbon Films. *Science (80-.).* **666**, 666–670 (2010).

243. Kim, M. J. *et al.* Silver Nanowires Network Film with Enhanced Crystallinity toward Mechano-Electrically Sustainable Flexible-Electrode. *Adv. Mater. Technol.* **2000838**, 1–8 (2020).

244. Wei, X. M., Zhang, J. M. & Xu, K. W. Energy calculation of (0 1 1) twist grain boundary in noble metals. *Appl. Surf. Sci.* **252**, 7331–7336 (2006).

245. Winther, G., Hong, C. S. & Huang, X. Low-Energy Dislocation Structure (LEDS) character of dislocation boundaries aligned with slip planes in rolled aluminium. *Philos. Mag.* **6435**, 1–20 (2015).

246. Yang, G. & Park, S. J. Deformation of single crystals, polycrystalline materials, and thin films: A review. *Materials (Basel).* **12**, (2019).

247. R.V.Mises. On saint venant's principle. *Bull.AMS* **51**, 555–562 (1945).

248. Weinberger, C. R. & Cai, W. Orientation-dependent plasticity in metal nanowires under torsion: Twist boundary formation and eshelby twist. *Nano Lett.* **10**, 139–142 (2010).

249. Ranger, A. E. & Hopkins, L. F. A new theory of the tensile behaviour of paper. *Fundam.*

Res. Symp. **1**, 277–318 (1962).

250. Bergström, P., Hossain, S. & Uesaka, T. Scaling behaviour of strength of 3D-, semi-flexible-, cross-linked fibre network. *Int. J. Solids Struct.* **166**, 68–74 (2019).

251. Ramachandramoorthy, R., Gao, W., Bernal, R. & Espinosa, H. High Strain Rate Tensile Testing of Silver Nanowires: Rate-Dependent Brittle-to-Ductile Transition. *Nano Lett.* **16**, 255–263 (2016).

252. Filleter, T. *et al.* Nucleation-controlled distributed plasticity in penta-twinned silver nanowires. *Small* **8**, 2986–2993 (2012).

253. Murr, L. E. *Handbook of Materials Structures*. (2015).

254. Carlton, C. E. & Ferreira, P. J. What is behind the inverse Hall-Petch effect in nanocrystalline materials? *Acta Mater.* **55**, 3749–3756 (2007).